UNIVERSITAT POLITÈCNICA DE VALÈNCIA

DEPARTAMENT DE COMUNICACIONS

# Optical Frequency Domain Interferometry for the characterization and development of complex and tunable photonic integrated circuits

## Ph.D. THESIS

by
Luis Alberto Bru Orgiles

Ph.D. Supervisors:
Dr. Pascual Muñoz Muñoz
Dr. Daniel Pastor Abellán

Valencia, January 2022

UNIVERSITAT POLITÈCNICA DE VALÈNCIA

DEPARTAMENT DE COMUNICACIONS

# Optical Frequency Domain Interferometry for the characterization and development of complex and tunable photonic integrated circuits

Luis Alberto Bru Orgiles
Photonics Research Labs
ITEAM Research Institute
Universitat Politècnica de València
Camí de Vera s/n, 46022 Valencia, SPAIN
luis.bru@upv.es

Ph.D. Supervisors:
Dr. Pascual Muñoz Muñoz
Dr. Daniel Pastor Abellán

Valencia, January 2022

*A mi familia*

*"Physics is like sex: sure, it may give some practical results,
but that's not why we do it."*

*"La física es como el sexo: sí, podría dar resultados prácticos,
pero esa no es la razón por la que lo hacemos."*

Richard P. Feynman

# Agradecimientos

La redacción de los agradecimientos de la tesis suele hacerse al final del proceso de escritura, cuando las energías están hundidas en el suelo de ruido. Pero aun así me enrollaré un poco. Hay muchísimas personas que considero que están relacionadas con la realización y culminación de esta etapa de mi vida, que me han apoyado de una manera u otra.

Buscar las razones por las cuáles acabé en una carrera investigadora científica podría remontarse a si existe predisposición genética a ello. En cualquier caso, lo que es seguro es que las circunstancias y gente del entorno son super determinantes. Mi profesora de matemáticas en el cole, Verónica, que me escogió sin dudar como representante para unas olimpiadas de matemáticas. En Bachiller recuerdo a Ismael, profesor de matemáticas, inspirador en su conocimiento, dotes docentes, y pasión. En una hora muerta entre clases aprovechó para explicar la relación entre lentes ópticas y curvas cónicas. También recuerdo a José Melero que, aunque era profesor de Biología, apoyó mi interés por la física y me facilitó sus apuntes de relatividad especial de primero de carrera. En la misma época Pepito, archiconocido profesor en Elche, fue una motivación crucial.

Una vez en la carrera, Física en la Universitat de València, son muchos los nombres de profesores. Me viene por ejemplo la figura de Jose Manuel Bordes, en primer curso. En esta etapa la inspiración no fue puramente académica. Mis amigos para siempre Rosa, Carlos, Pablo, Paloma, Luis, que siempre han estado ahí. También durante años, mi desde y para siempre querida Mari que, a pesar de la vida, todavía hoy me apoya siempre que puede.

En mi primera experiencia investigadora, colaboré con el grupo de óptica no lineal y óptica cuántica de la misma facultad. Eugenio Roldán, Germán del Valcárcel y Fernando Silva. También con Armando Pérez, físico teórico. Los admiro muchísimo y fueron, y de alguna manera siguen siendo, una grandísima inspiración. También mis compañeros y buenos amigos en esta etapa: Joaquín, Rubén, Rafa, Marga, Manu. Muy grandes ellos. Más tarde, empecé mi doctorado en Photonics Research Labs, en la Universitat Politècnica de Valencia. Mucha gente ha pasado por aquí. Desde los inicios con Rocío, Chicharro, Manolo, Hervás, Susana, Andrés, Juan... y Berni, al que aún hoy tengo cerca como amigo, menos mal que estaba en los inicios. A los que aún hoy en día veo por allí... son muchos, entre ellos: Erica, la bedel de la sala. Demetrio, gran persona y temple. Hablando de italianos Giuseppe, reciente incorporación. Dani, con su inspirador amor por lo que hace, y que lo convierte en el dios yeclano de la fotónica. Jesús, compañero, amigo del metal y vecino del barrio (de Jesús, claro). Y por supuesto Gloria, mi persona más especial. Amigos desde la carrera, nos hemos cuidado siempre durante esta época. Menos mal.

Fuera del ámbito académico, grandes personas han estado ahí también. Gracias a Esther, que me cuidó incondicionalmente y con amor durante muchos años en la época del máster y principios del doctorado. Ambos empezamos nuestra carrera en la fotónica de la mano. Gracias también a Elena, buena amiga en la actualidad, que también tuvo que lidiar de cerca con mis problemas un par de años. Por poquito tiempo, pero también con cariño y preocupación, ahí estuvo Cristina. Patri, como no quererla. De esas personas buenas que siempre están ahí, desde hace años. Rubén, mi mayor fuente de apoyo y comedia en el ámbito amistoso. Dulce, amiga y compañera de piso muchos años, siempre preocupada por mí. Pablo, querido amigo del metal y de la vida. Andrea, y más recientemente Quim (y más reciente todavía, el pequeño Manel). Miguel Ángel (conocido como MA), que me ha salvado de alguna época oscurilla. También la cuadrilla de la academia de guitarra, buenas risas y confidencias: Alberto, Jose y Josevi, además del ya mencionado Berni. También algún amigo que me queda en Elche. Raúl, querido amigo desde la ESO y referente ingeniero apasionado por su mundo. Quizás no haya tanta relación hoy en día, pero se han preocupado mucho por mí en el pasado y les quiero: Toni, Cristina, Emilio, incluso Pedro.

Por supuesto, gracias a mis jefes, los catedráticos Pascual Muñoz y Daniel Pastor. Con su atenta y valiosa supervisión he aprendido casi todo lo que se sobre este trabajo y fotónica integrada, especialmente la parte más ingenieril. Son dos bestias legendarias en este mundillo. Con el paso de los años, además, los considero mis amigos.

Por último, y sí más importante, mi familia. Qué se puede decir de quien te lleva soportando a todos los niveles los 30 y pico años que llevas existiendo (o como poco, los que ellos llevan). A mi tía Manoli, que ojalá se termine de recuperar del momento tan difícil que pasa. A mi abuela Asunción, la mejor, que aún está ahí y es el mayor ejemplo de ganas de vivir que conozco. A mi abuelo Salvador, así como a mis abuelos paternos, Teresa y Diego, estoy seguro que les hubiera gustado saber lo que acabo de terminar. Mis hermanos, Alejandro y Sonia. Qué puedo decir de ellos, aunque no sean las personas con las que más hablo, son mis mejores amigos y los admiro. He elegido sus nombres y los he tenido en brazos. Y especialmente a mis padres. Con permiso del resto, los mejores de todo. Ni siquiera alcanzo a comprender ese nivel de incondicionalidad, en todos los aspectos. Un millón de gracias, os quiero muchísimo a todos. Por todos vosotros, este paso en mi carrera finalmente ha podido darse.

# Abstract

This PhD thesis covers the characterization of complex photonic integrated circuits (PIC) by using Optical Frequency Domain Interferometry (OFDI). OFDI has a fairly simple implementation and interrogates the device under test (DUT) providing its time domain response, in which the different optical paths followed by light manifest in contributions with position, amplitude and phase information. Together with a working OFDI setup built in our laboratory and integrated test structures involving devices such as ring resonators, interferometers, etc., we propose and implement techniques to get crucial optical parameters such as waveguide group refractive index, chromatic dispersion, polarization rotation, and propagation loss. Also, to characterize optical couplers. Direct optical phase assessment is made in different experiments permitting, amongst others, the characterization of on-chip heat effects. In the culmination of the thesis, the co-integration of the OFDI interferometers with the DUT is addressed, conceiving it as an integrated characterization structure. The use of integrated waveguides provide high stability and adaptation to the DUT, as well as an inherent dispersion de-embedding mechanism. It is provided analysis and experimental proof of concept with an arrayed waveguide grating as DUT in a silicon nitride platform. A considerable leap forward is then taken by proposing a novel three-way interferometer architecture, reducing the measurement complexity. Wide experimental validation is carried out using different laboratory equipment, horizontal and vertical chip coupling, and different DUTs in silicon nitride and silicon-on-insulator.

# Resumen

Esta tesis aborda la caracterización de circuitos fotónicos integrados (PIC) usando interferometría óptica en el domino de las frecuencias (OFDI). OFDI tiene una implementación razonablemente simple e interroga al dispositivo bajo test (DUT) proporcionando su respuesta en el dominio del tiempo, en la que los distintos caminos ópticos seguidos por la luz se manifiestan en contribuciones que contienen información de posición, amplitud y fase. Junto con un *setup* OFDI construido en nuestros laboratorios y estructuras de test integradas que involucran anillos resonantes, interferómetros, etc., proponemos e implementamos técnicas para obtener parámetros ópticos cruciales tales como el índice de grupo, dispersión cromática, rotación de polarización y pérdidas de propagación de guías de onda. También para caracterizar acopladores ópticos. Se realizan evaluaciones directas de fase óptica en diferentes experimentos para, entre otras aplicaciones, caracterizar efectos de calor en chips. En la culminación de la tesis, se aborda la integración conjunta de los interferómetros de OFDI junto con el DUT, concibiéndolo como una estructura de caracterización integrada. El uso de guías de onda integradas proporciona una alta estabilidad y adaptación al DUT, además de un mecanismo inherente de compensación de la dispersión. Se realiza un análisis y prueba de concepto experimental caracterizando un *arrayed waveguide grating* en tecnología de nitruro de silicio. Seguidamente, se da un paso adelante proponiendo una arquitectura interferométrica de tres brazos novedosa que permite reducir la complejidad de la medida. Se lleva a cabo una validación experimental amplia usando distintos equipos de laboratorio, acoplamiento horizontal y vertical al chip, y diferentes DUTs en tecnologías de nitruro de silicio y *silicon-on-insulator*.

# Resum

Aquesta tesi aborda la caracterització de circuits fotònics integrats (PIC) usant interferometria òptica al domini de les freqüències (OFDI). OFDI té una implementació raonablement simple i interroga el dispositiu sota test (DUT) proporcionant la seva resposta en el domini del temps, en què els diferents camins òptics seguits per la llum es manifesten en contribucions que contenen informació de posició, amplitud i fase. Juntament amb un *setup* OFDI construït als nostres laboratoris i estructures de test integrades que involucren anells ressonants, interferòmetres, etc., proposem i implementem tècniques per obtenir paràmetres òptics crucials com ara l'índex de grup, dispersió cromàtica, rotació de polarització i pèrdues de propagació de guies d'ona. També per caracteritzar acobladors òptics. Es fan avaluacions directes de fase òptica en diferents experiments per, entre altres aplicacions, caracteritzar efectes de calor en xips. A la culminació de la tesi, s'aborda la integració conjunta dels interferòmetres d'OFDI juntament amb el DUT, concebent-ho com una estructura de caracterització integrada. L´ús de guies d´ona integrades proporciona una alta estabilitat i adaptació al DUT, a més d´un mecanisme inherent de compensació de la dispersió. Es realitza una anàlisi i prova de concepte experimental caracteritzant un *arrayed waveguide grating* en tecnologia de nitrur de silici. Seguidament, es fa un pas avant proposant una arquitectura interferomètrica de tres braços nova que permet reduir la complexitat de la mesura. Es du a terme una validació experimental àmplia usant diferents equips de laboratori, acoblament horitzontal i vertical al xip, i diferents DUTs en tecnologies de nitrur de silici i *silicon-on-insulator*.

# Contents

# List of Figures

# List of Tables

# Chapter 1

# Introduction

Light science is about light radiation, whose properties are determined by its amplitude, frequency, phase and polarization state. At its minimal expression, light is made by photons which are governed by the laws of quantum physics, a complicated, bizarre and exciting world. In its macroscopic picture, the classical theory of light says that that it is electromagnetic radiation, whose existence and behaviour is predicted from the Maxwell equations. From them, wave equations are derived and, together with the set of boundary conditions, all the wave-related phenomenology that light experiences is described. Although it is fascinating, in this thesis we do not address any topic related with the nature of light, its behaviour, interactions and properties, which corresponds to classical and quantum optics. Instead, our endeavour is in the the applications that light interactions with itself, or any other physical entity, offer.

In the classical world, light is definitely an electromagnetic wave, and it is described by complex vectors. As a wave, a great part of the interaction that can experience with itself is based on the superposition principle: when two light waves interact, their superposition can be constructive (whether the vectors are aligned and in phase), destructive (the complementary case) or any other intermediate continuum of situations. The most basic way of interference takes place when two 'simple' waves (e.g. planar waves) that have been propagating independently, coincide in the space (in a stationary picture). Light diffraction is a more intricated way of interference [2]. In the core of interference is that, in the superposition of complex fields, the light phase difference between them translates, unambiguously, to an amplitude outcome. And photodetectors basically measure a generated photocurrent which is proportional to the optical intensity of light, i.e. the squared modulus of its amplitude. Therefore, light interference is the key mechanism to know the optical phase relationship between two optical fields.

The devices that are designed and intended to superimpose light and generate interference patterns are the interferometers. It can be physically carried out by division of a wavefront, as it is the case of the well-known Young's doubleslit experiment, or by amplitude splitting, where the incident wave is divided into separated beams and after some path independent propagation, they are recombined. Correspondingly, optical interferometry, which has been employed for more than a century, is the method that employ interferometers to carry out optical phase sensing. We cover interferometric techniques in section 1.2.

Interferometry is an important part of photonics science, a branch of applied science that looks for creating, manipulating and detecting light signals (not only visible, but other regions of the electromagnetic spectrum, specially longer wavelengths) to carry out varied technological applications. The interaction of photons with materials is behind of what it can be done with light. Therefore, in order to settle the technological platforms where light phenomenology is involved, photonics research gathers together extremely prominent doctrines of physics and engineering such as material science, solid-state physics, semiconductors or electrical engineering. Regarding their applications as such, many other branches of science and engineering are involved, including biological sciences, telecommunications or astronomy, apart from different optics sub-branches, just to mention some.

## 1.1 Integrated photonics

Integrated photonics, first introduced in [3], is an emerging branch of research that deals with the integration of photonic waveguides and devices into small chips, with a similar evolution to integrated electronic circuits. In the past years, integrated photonics has become a mature branch of technology, implementing increasingly complex photonic integrated circuits (PIC). Its popularity and development owes partly to the emergence of multi-project wafer (MPW) fabrication runs [4], where the wafer space for designs and fabrication costs is shared between the users.

Amongst the multiple PIC technology platforms proposed by the community, the following ones clearly stand out. On the one hand, there is silicon photonics, which includes silicon-on-insulator (SOI) and with later popularity, but with their own strengths and weak points, silicon nitride [5, 6] (SiN). Part of their success is due to the fact they are technologies compatible with complementary metal-oxide semiconductor (CMOS), inherited from mature integrated electronic circuits fabrication. SOI is the most popular technology and the most employed in commercial applications [7, 8]. Besides, as a high-index-contrast technology it allows for large-scale PIC integration. SiN technology [9, 10] is less high-contrast and draws attention as it is transparent in a wider wavelength range, including operation at visible wavelengths apart from mid-infrared. For a thorough survey on SiN technologies, see a recent PhD thesis of our group [11]. On the other hand, indium phosphide (InP) material gives rise to PICs with very interesting characteristics [12]. Its main advantage with respect to silicon photonics is that it allows the monolithic integration of active semiconductor materials along with the passive waveguides and devices. Therefore, integrated lasers, photodetectors, optical modulators, optical switches, amplifiers, etc., are technologically direct in InP platforms. In silicon photonics, the active functionalities are possible by integrating III-V semiconductor materials, but require additional and costly fabrication steps [13]. One of the the main drawbacks of InP is the moderate optical confinement of the waveguides, not permitting to generate high-density waveguides and devices integration. Besides, it is not a CMOS compatible technology.

In the context of this thesis and our PIC research group, integrated devices are mostly fabricated in SiN platform, also in SOI, and typically with basic fabrication processes. In what follows, we briefly summarize the most important integrated devices, most of them appearing in this thesis. After that, we describe the different parts of a laboratory PIC characterization setup.

### 1.1.1 Integrated devices

There is a great deal of different integrated devices that has been proposed along the integrated photonics research history, implementing different functionalities for a myriad of applications. Some of them are very simple, others more complex, all of them composing PICs. So often the complex devices and PICs implementing high-level functionalities are a combination of the simpler ones. Oriented to those we employ in this thesis, a summary is in Fig. 1.1 and a description in what follows:

**Optical waveguide:** they can be considered the most trivial integrated devices, and they are basically employed to guide light in the PICs. Depending on the index contrast, thus the waveguide light confinement, smaller radius bends can be reliably designed, to change the light direction. In their canonical dimensions, typically rectangular and implementing a single-mode regime (strip waveguides), variations of it are introduced in specific parts. Amongst others, this is used to implement multi-mode regions for some applications, to alter polarization state, to implement filters, and also for tapers and inverted-tapers to aid in the mode size matching with optical fibers in the horizontal input and output coupling to the chip [14].

**Optical couplers:** this devices are, after waveguides, the most essential ones, implementing light amplitude splitting and combination. Depending on the underlying physics principle, there are several devices implementing optical couplers: in the directional couplers, two waveguides are put nearby enough so their optical fields are in contact and coupling between them occurs, leading to an oscillating power sharing between the waveguides. This section is, by design, stretched up to a given length where the power of the fields implement the desired splitting ratio. In multimode interference couplers (MMI), light is launched to a wider waveguide region, where a number of modes can exist and are excited. These modes propagate at different velocity and the resulting interference landscape changes along the device length. Patterns corresponding to each eigenmode appear and repeat after a given distance, by waveguide Talbot effect, and can be predicted. When the desired pattern takes place, two (or more, though more rarely used) waveguides are set to gather the amplitude separated light. MMIs are less wavelength-dependent devices when compared to directional couplers. Less used, Y-junctions are physically the simplest coupler as they directly divide one waveguide into two. Considering a greater number of inputs and outputs, the star (or slab) couplers make use of a quasi-free propagation region that distributes light from individual inputs over a greater number of outputs.

**Interferometers:** an interferometer consists of splitting light in amplitude to make it travel through different paths, and then combine them. The most used is the Mach-Zehnder interferometer (MZI), for which two basic optical couplers (e.g. MMIs) and waveguides are needed. These devices are central for a huge amount of applications in PICs such as filters or switches.

**Ring resonators:** ring resonators (RR) are optical cavities that, like interferometers, are a combination of couplers and waveguides. Incident light path is divided in a coupler (typically a directional coupler to implement weak coupling), and a small part of the light make roundtrips around the RR cavity, so that a certain group frequencies resonate. Combinations of simple RR are made to implement sofisticated filters such as CROWs [15] or SCISSORS [16].

**Bragg gratings:** they are periodic structures that, based on Bragg's law, scatter the incident light very directionally and wavelength-dependent. This artificial one-dimensional crystal lattices can be implemented by lateral waveguide width variations, or through different waveguide heights with different etching processes. Depending on their design, part of the light can be reflected perfectly backwards and/or radiated vertically out of the chip. Therefore, these structures are widely used to implement vertical chip coupling (grating couplers).

**Arrayed waveguide gratings:** Wavelength multiplexing and de-multiplexing functionalities (MUX, DEMUX) are typically implemented on-chip by arrayed waveguide gratings (AWG) [17–20]. In this device, which can be considered the integrated version of a prism, light illuminates an slab or star coupler which feeds a given number of outputs. An array of waveguides propagate light with an incremental length intended to introduce an incremental and linear phase delay between all of them when reach the second slab coupler. This formed extended source, with linear incremental phase and nearly Gaussian apodization, diffracts along the (quasi) free-propagation region which focuses light onto each output waveguide depending on the light wavelength. Other device implementing these functionalities is the echelle-grating [21–23].

In combination with the described passive devices, there are active devices. Leaving aside those active devices requiring other semiconductor materials, probably the most popular and simple active device is the metal heater [24, 25], represented in Fig. 1.1 at the bottom right. They comprise a metal conductor at a given height over the waveguides (e.g. deposited over the silicon oxide cladding).

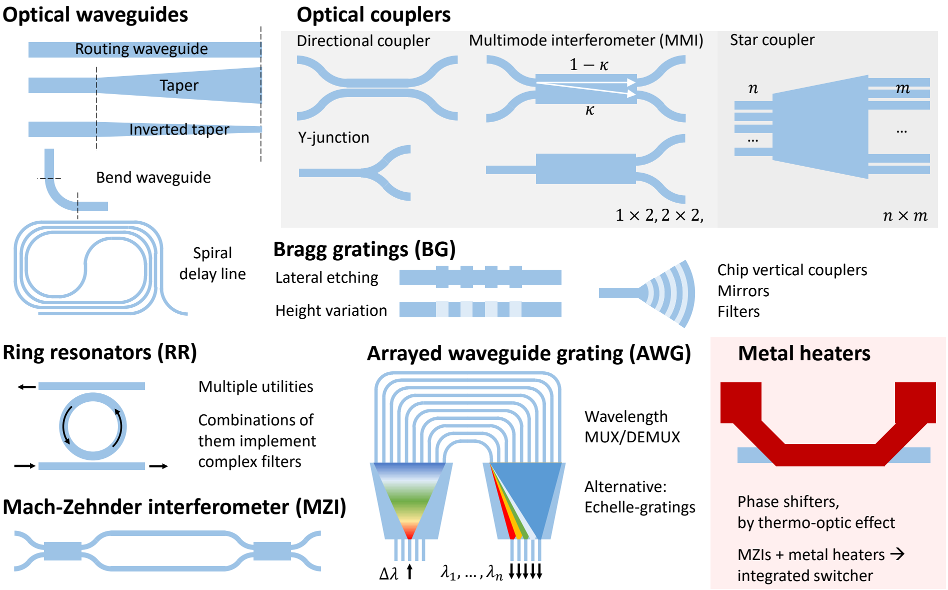

**Figure 1.1:** Basic integrated devices: different combinations of optical waveguides and couplers give rise to more complex devices such us RRs, interferometers, or AWGs. All of them are combined to carry out specific functionalities.

This metal is intended to generate heat by Joule effect that takes places when an electrical intensity travels over it. This generated heat propagates and changes the temperature of the waveguides. By thermo-optic effect, it changes their effective index, so that by controlling an electrical current these devices implement configurable phase-shifters. A direct application is to implement integrated optical switches, in combination with MZIs. They are not exempt, though, of complications. Their power consumption is typically high and heat crosstalk to other parts of the chip takes place, affecting the performance of nearby devices. Therefore, a proper heat sink and temperature controller is needed. In order to isolate this effect, some strategies to act as heat walls may be implemented, e.g. by etching material and creating an air layer.

Routing optical waveguides (both straight and bend sections) plus optical couplers (any $n \times m$ coupler may be built through $2 \times 2$ couplers) give rise to every other more complex device. Not surprisingly, programmable PICs relies upon the combination of these two classes of primitive devices to form meshes, along with active devices of course [26].

### 1.1.2 Characterization setup

In order to test the behaviour of the fabricated devices included in a PIC, they are typically set in a test space of the chip, separately, either by including some test

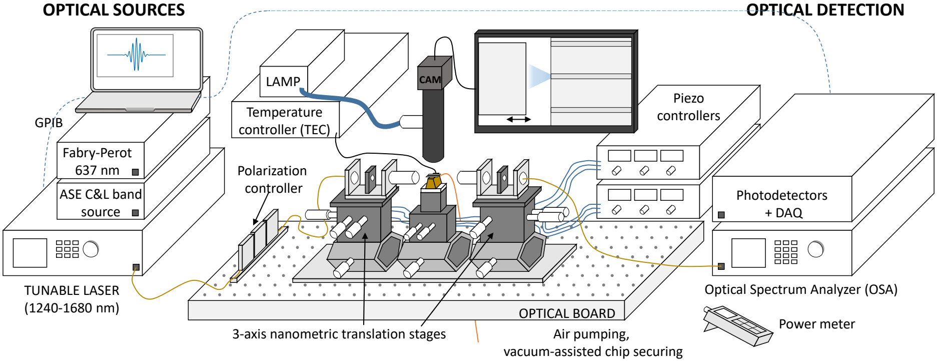

**Figure 1.2:** Typical integrated photonic chip characterization setup, including light sources, detection parts, movement stages and camera to aid in the fiber-chip alignment.

structure or alone. In any case, with the intention of interrogate them or a more complex PIC, a functional characterization setup is absolutely indispensable.

In Fig. 1.2, a typical PIC characterization setup sketch is shown. The setup is mounted onto an optical board that is over a vibration isolation special table. In the center of the figure, the chip chuck (shown in gold color) is joined to a 3-axis stage. The sample chip is settled over and secured to it by vacuum-assisted strategy, making use of an air pump. If the specific application requires it, a temperature controller (TEC) is connected to a Peltier element installed under the chip that balances temperature, sometimes helped by heat radiator structures underneath. Other 3-axis translation stages with nanometer precision are at both sides of the chip. These ones hold the stages where optical fiber is aligned to the sample chip. Whether they are V-groove fiber holders in direct fiber to chip coupling strategy (with simple or lensed fibers), or stages with objectives, where light is collimated to pass along a free-space region (where other elements can be interposed, like polarizers, see section 2.5 in this thesis) and coupled to objective, that reduces the light beam waist at its focus to match the chip waveguide modes size. These stages are equipped with piezoelectric controllers for precise alignment.

Light input, which in the figure is conducted on the left side, is formed by a fiber pigtail that connects the light source to the left alignment stage. The typical available light sources in a PIC characterization lab are coherent tunable laser sources and broadband sources based on amplified spontaneous emission (ASE). These are the ones to interrogate the chip, their use depend on the specific application and they have associated different equipment at the optical detection part. If input light polarization is desired to be controlled when using polarized light sources as tunable laser (TL), 3-paddle stage providing independent rotatable wave plates are employed in the connecting fiber pigtail. Besides, other classical light source in the laboratory is a single-channel visible laser (e.g. red light emitting at $\lambda = 637$ nm), employed in the manual alignment process. In this process, where the piezo-controlled 3-axis translation stages are moved, the chip and fiber or objective are visualized by using a camera providing a top view of the system in a monitor screen. For proper illumination during this top view observation, a halogen lamp is employed

In the right part of the figure, a fiber pigtail connects the output stage to the photodetection equipment. An optical spectrum analyzer is employed if a broadband source is feeding the sample chip under test, in order to draw its amplitude spectrum. Conventional photodiodes (or power meters) are employed when a single-wavelength test or a wavelength sweep is being performed. In the case of the photodiodes, output voltage is converted to digital data by means of a data acquisition card (DAQ). An indispensable tool in a PIC characterization setup is a fiber-optic power meter, that aids in the alignment process, whether this is automatic or manual. Of course, a laptop is employed to communicate with the different lab equipment and orchestrate the measurements.

Finally, not shown in the figure are the components to control the possible active (electric) parts of the chip, which typically consists of current/voltage precision sources and the added stages to land the electrical probe needles on the chip, whether they are single or multi-contact.

## 1.2 Interferometric techniques

The first interferometer ever proposed was Michelson's instrument in 1881, that some years later gave rise to the famous physics experiment where, in search of the luminiferous aether detection, that was the believed carrier of light waves by the time, they found evidence against its existence [27]. Ultimately, this led some years after to the special theory of relativity, that discards its existence. The instrument they employed was afterwards known as the Michelson-Morley interferometer. Basically, light path is split into two by means of a beam splitter, it reflects on both paths and goes back to be superimposed again. Amongst the myriad of experiments where this concept has been employed since then, it is remarkable one of the most important contemporary physics experiments, the LIGO experiment, where gravitational waves predicted by the general theory of relativity were experimentally observed in 2015 [28]. After Michelson-Morley interferometer was invented, different type of interferometers arose. It was also at the end of 19th century when first L. Zehnder, then L. Mach improving it, proposed a new type of interferometer similar to the Michelson-Morley but without reflection, widely used in general and very important in this thesis work, the Mach-Zehnder interferometer.

In the photonics world, the different interferometric techniques can be classified, broadly speaking, by whether they are carried out in the time domain or in the frequency domain [29,30]. Optical time domain reflectometry (OTDR) [31,32] is a well-known technique that requires short light pulse generation and achieves high length ranges, suitable in the world of optical fiber testing and devices, and having a phase-sensitive version [33]. Low-coherence interferometry (LCI) [34,35] makes use of broadband light sources and involves moving mechanical parts in the body of the interferometer, achieving great spatial resolutions desirable in optical sensing. On the other hand, optical frequency domain reflectometry technique (OFDR) [36–39] is based on a passive interferometric setup and relies on a TL source sweep that determines a relatively high spatial resolution.

In photonics, the major part of the interferometric techniques research in the literature is applied to test optical fiber devices. Later on, they have been envisaged to characterize integrated devices too. However, its use is not too much widespread in the PIC community, likely and partly due to the high cost and complexity of existing commercial equipment implementing it. There is, though, an increasing interest by the PIC community, e.g. foundries to have precise and reliable characterization tools in their chip fabrication steps. In accordance to it, we believe that this type of advanced characterization, allowing to track the device under test (DUT) phase response and therefore, through processing, to switch between its frequency and time domain responses, make the difference with the increasing complexity of PICs, providing temporal resolved information that allows to deal with the minutiae of light propagation in the integrated waveguides and devices. Under this vision, it is our first motivation in this thesis to contribute to the community by laying the foundations of a versatile, easy to implement, reachable interferometric setup for photonics research laboratories like ours, with standard know-how and equipment, as an alternative to the highly complex commercial equipment available, as it is the case of Luna Technologies Inc. commercial products based in OFDI [40] (a description of their optical vector analyzer can be found in section 2.5). And beyond, we aim for creating a characterization framework with applications based on the technique. In these respects, taking into account the interferometric techniques characteristics brief discussion above, we find OFDI as the candidate that better fits the stated requirements, thanks to their high spatial resolution and passive interferometric setup. Some works considering OFDI applied to PIC characterization have been published in the literature: in reflectometry mode, its more used application is to characterize waveguide group index and propagation loss [41–44] (we cover this topic, along with our works, in section 3.3.1). An equivalent technique (minimum phase) has been proposed as well to remove intra-chip reflection artifacts [45]. By the beggining of this thesis, OFDI was applied for on-wafer mapping using waveguides with reflectors [46], and also to characterize intra-chip reflections coming from waveguide crossings [47]. More recently, it has been used for active flip-chip alignment [48], to characterize transmittance and reflectance of elemental devices [49], and incorporating frequency combs to calibrate the measurements of integrated devices [50].

Finally, just mention that OFDI stands for interferometry and we make use of this acronym along this thesis for the sake of generality, since most of the times we employ the setup in transmission mode. OFDR stands for reflectometry, inherited from its former application in the field of optical fibers.

## 1.3 Objectives

This PhD thesis main objective is the exploration of OFDI technique as promising laboratory tool to aid in the demanding characterization of integrated devices. This task can be sorted as:

1. Development of an OFDI setup, based upon the existing literature and expertise and resources of the research group.
2. Validation of the OFDI technique to interrogate integrated devices; search for refinements of the system.
3. Development of OFDI-based applications in the field of integrated photonics, by proposing and investigating novel techniques involving test structures, allowing to retrieve valuable information about integrated waveguides and devices.

## 1.4 Thesis outline

According to the goals of this thesis, the manuscript is organized by chapters as follows:

**Chapter 2:** theoretical analysis of OFDI, including functioning and physical implementation. Considerations about important involved parameters as it is the presence of chromatic dispersion and polarization phenomena taking place in the employed waveguides.

**Chapter 3:** OFDI-based applications. First validations of OFDI in this thesis are reviewed. After that, developed applications in this thesis based in OFDI employing RR and other test structures as a mean to characterize waveguide dispersion, waveguide losses and optical coupler parameters, amongst others.

**Chapter 4:** integration of the OFDI interferometric part along with the DUT, giving room to a powerful test structure to characterize integrated devices and waveguides. A refinement of this structure is proposed as well along with extensive experimental validation including several DUTs in different photonic technology platforms, as well as different experimental conditions of interest.

**Chapter 5:** general conclusions of the thesis, perspectives, and open research lines.

Some of the published articles and conference papers in this thesis (a list can be found in Appendix A), are reproduced to a great extent in their corresponding parts of the manuscript. In chapter 3, papers [51, 52] in section 3.2, and [53] in 3.3.2. In chapter 4, papers [54, 55].

## Chapter 2

# OFDI theory and implementation

In this chapter, we describe in detail the optical frequency domain interferometry (OFDI) technique. After introducing some historical context and comparison to other interferometric techniques in the previous chapter, here we go first to explain OFDI functioning and implementation in section 2.1. After that, we provide an analytical overview of the interferometers in section 2.2, giving rise to the interferograms. Next, all the associated interferogram processing involved to switch to the time domain, the description of the information that is contained in that picture, and other features such as the spectral response reconstruction, are covered in section 2.3. In section 2.4, we focus onto the effects of chromatic dispersion in OFDI technique. Finally, we review how light polarization can affect OFDI measurements and which are the related solutions to alleviate its effects and get information about it.

## 2.1 OFDI implementation

We can classify an OFDI setup in the optical source, the interferometric, and the photodetection parts. As it is represented in Fig. 2.1, the optical source, that in a conventional OFDI system consists of a tunable laser source (TL), feeds two interferometers simultaneously. These interferometers can be of different kind including Michelson-Morley [37, 56], Fabry-Perot [47] and, mostly used, Mach-Zehnder interferometer (MZI) [39]. In fact, this is the kind of interferometer we use along the thesis and we refer to it as MZI and interferometer indistinctly, except where indicated.

These two interferometers are passive, with fixed path length differences (PLD) of $\Delta l$ and $\Delta l'$, such that $\Delta l' \geq 2\Delta l$, determined by Nyquist sampling criterion as we shall cover in next sections. In the upper interferometer, that we call DUT-MZI, the device under test (DUT) is inserted in one of the arms. How it is inserted depends on the kind of experiment we aim to perform: in serial disposition (represented in the DUT-MZI upper option of Fig. 2.1) we have the OFDI

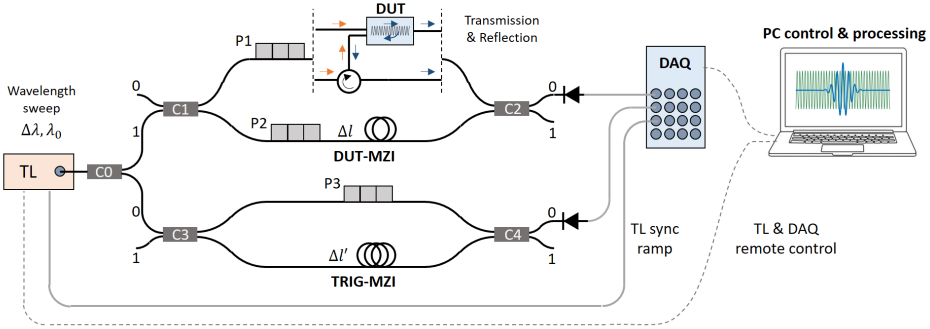

**Figure 2.1:** OFDI setup sketch: the TL is connected to two interferometers, where the DUT is connected to one of them. The TL sweep is performed and photodetected through remote computer control, and digitized interferogram data stored for analysis.

in transmission mode, which is the most common in our context. Alternatively, the same setup can be straightforwardly converted to reflection mode by using a fiber-based optical circulator. This kind of device interrogation, as mentioned above in this thesis, corresponds to the former use of this technique (OFDR) intended to assess optical fiber devices doing reflectometry. In fact, it is probably in this reflectometry experiment where a Michelson-Morley interferometer is mostly used as suitable. In general, for an external OFDI setup, the interferometric part is made of optical fiber. Therefore, the optical coupling / splitting is implemented by the classical commercial devices based on fused silica evanescent coupling. At the starting splitter (C0) and the one of the DUT-MZI (C1), it is usually convenient to employ a biased splitting (e.g. 90:10) to maximize light power for the DUT interrogation. This approach maximizes the resolution of the obtained traces regarding the dynamic range of the system. In the MZI arms, polarization controllers are employed, typically implemented by the 3-paddle stage providing independent rotatable wave plates. In the upper arm of the DUT-MZI, P1 is intended to control light polarization coupled to the DUT, whereas P2 in the reference arm is for polarization alignment to ensure light beating in C2. A third polarization controller, P3, is used in the TRIG-MZI (standing for triggering) for the same purpose. For more details in polarization management in OFDI, see section 2.5 below.

OFDI is a homodyne detection technique. This basically means that it self-references the measurements to a local oscillator with the same optical source, thus being robust against possible scanning nonlinearities. This OFDI feature is appealing, not only because it makes room for more defective measurement takes, but also it opens the door to explore less demanding optical sources. This means that benchmark, bulky and expensive TL sources are not necessarily required, but also other cheaper options as solid state lasers like vertical-cavity surface-emitting lasers (VCSEL) [57], amongst others, might be considered. Beyond, a broadband source may be explored to do OFDI, in combination with an optical spetrum analyzer (OSA) in the photodetection part, doing the necessary scanning part. This combination to do OFDI, not previously demonstrated to the best of our acquintance, is reported in a very specific advantageous context in [55] and addressed in this thesis in chapter 4.

On each interferometer, the light coming from the two arms is put together by means of couplers C2 and C4, respectively for DUT-MZI and TRIG-MZI. The superposition of both signals gives rise to light interference, and depending on the relative phase relationship between them, this gets in the continuum from destructive to constructive interference. The monotonic TL sweep in wavelength draws the wavelength-resolved interference pattern (more formal details in next section). During the wavelength scanning, the interference pattern has to be captured by means of the photodiodes (PD). The PDs need to be fast enough to cope with the resolution of the interference fringes, that are generated at velocity given by the TL speed $v_{\mathrm{TL}}$ and the interference pattern free spectral range (FSR), i.e. the wavelength increment between two consecutive oscillations. From Eq. 2.9, derived in the next section, the TRIG-MZI oscillation phase, that is the fastest and thus the most demanding to be resolved, is given by $\beta\Delta l'$. The mean propagation constant $\beta_0 = 2\pi n_0/\lambda_0$ leads to an average $\mathrm{FSR}_0 = \lambda_0^2/\left(n_0\Delta l'\right)$. Therefore, the lapsed time to overcome one oscillation is given by $\mathrm{FSR}_0/v_{\mathrm{TL}}$ that, in the most demanding of our scenarios ($n_0 = 1.468$, $\Delta l' \simeq 80$ cm, $\lambda_0 = 1550$ nm, $v_{\mathrm{TL}} = 100$ nm/s) is about 20 µs. This can be always relaxed by reducing $v_{\mathrm{TL}}$, that in our case is benchmark Yenista TUNICS T100R/M (old model, 2012, shown in Fig. 2.2 at the right) capable of configurable scanning speed from 1 to 100 nm/s. In our setup, we make use of Thorlabs FGA01FC InGaAs high-speed photodiodes [58]. They are unmounted PDs whose rise/fall time $t_r$ depends on the employed load resistance $R_{\mathrm{L}}$. As shown in Fig. 2.2 at the right, the PDs are mounted in a standard high impedance front-end without electronic amplification, providing an electrical voltage proportional to the optical intensity. The nominal specification for $R_{\mathrm{L}} = 50\,\Omega$ is $t_r = 0.3$ ns, 4 orders of magnitude faster, so there is room enough to properly resolve the interference fringes. In fact, in order to maximize PD output voltage, in most of the cases we employ greater $R_{\mathrm{L}}$ than the nominal without getting into trouble.

Once this electrical photocurrent is properly generated, a data acquisition card (DAQ) is employed to digitize this signal. In our case, we employ a National Instruments USB-6259 (old model, from 2007, shown in Fig. 2.2 at the left), able to simultaneously acquired 16 analog channels at 1 MS/s in aggregated rate, i.e. a shared 1 µs clock sampling. In normal conditions, apart from both interferograms we capture a third trace corresponding to an electric ramp generated by the TL during the wavelength scan, that we use in our setup for band referencing, i.e. establish initial and final wavelengths of the sweep ($\lambda_1$,$\lambda_2$). We use this approach for relative $\lambda$ referencing. It is pretty straightforward and useful for our purposes, although there are more precise and absolute $\lambda$ referencing strategies as, for example, to employ an Hydrogen Cyanide gas-cell as in [39]. This ramp trace does not need as much resolution as the interference patterns captured by the PD, so the DAQ sampling capability is more than enough for our purposes. Finally, the

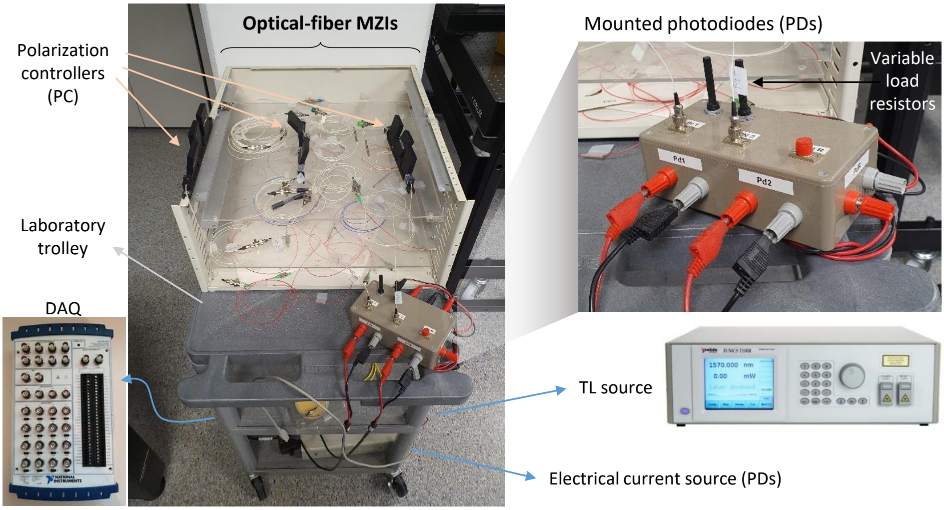

**Figure 2.2:** Laboratory OFDI setup built during this thesis. All the setup elements are installed on a laboratory trolley, The optical interferometric part is at the top part of it, whereas the lab equipment is on the shelves below, including the TL, the DAQ, and the electrical current source.

resulting generated data is transferred to the computer and stored to hard drive. The resulting trace after all this photodetection process is what we call the raw or unprocessed interferograms. We deal with the interferograms processing part in section 2.3.

## 2.2 Theoretical description

Coupled-mode theory [59, 60] is at the formal basis of the description of the photonics systems in this thesis. Without going into detail, it allows to analytically describe wave-guided phenomena in a simple way and basically consists on considering the existing propagating modes separately, putting the implicit time dependance of the form $\exp(j\omega t)$ aside, so that we get a spatial propagation picture of them, obeying the following simple differential equation and solution:

$$\frac{\mathrm{d}\mathbf{E}}{\mathrm{d}x} = -j\beta\mathbf{E} \rightarrow \mathbf{E}(\beta, x) = \mathrm{E}\exp(-j\beta x), \tag{2.1}$$

where $x$ represents the propagation direction, $\beta$ the propagation constant of the mode in the medium, and $\mathrm{E} = |\mathbf{E}|$ the mode amplitude. This is the widespread approach to describe analytically the problems in photonics.

All the purely propagation features are given by $\beta$ that, in general, is a function of the frequency or wavelength. Conventionally, it is modeled by the well-known series expansion of $\beta \equiv \frac{n(\omega)\omega}{c} = \frac{2\pi n(\lambda)}{\lambda}$ (where $n$ is the effective index of the medium) around the central angular frequency $\omega_0$, and up to a second-degree polynomial to account for chromatic dispersion of the medium, as:

$$\beta(\omega) \simeq \beta_0 + \beta_1 \Delta\omega + \frac{1}{2!}\beta_2 \Delta\omega^2, \tag{2.2}$$

where $\Delta\omega = \omega - \omega_0$. Of course, where required, more terms of the series expansion may be adopted. The coefficients $\beta_n \equiv \frac{d^n\beta(\omega)}{d\omega^n}\Big|_{\omega=\omega_0}$ are readily related to important figures of light propagation as:

$$\beta_0 = \frac{n_0\omega_0}{c} = \frac{2\pi n_0}{\lambda_0}; \quad \beta_1 = \frac{1}{v_{\mathrm{g},0}} = \frac{n_{\mathrm{g},0}}{c}; \quad \beta_2 = -\frac{\lambda_0^2}{2\pi c}D = -\frac{2\pi c}{\omega_0^2}D. \tag{2.3}$$

$\beta_1$ is the group delay per unit length in the center of the band $\lambda_0$, whereas its inverse is the group velocity of light $v_{\mathrm{g},0}$, defined by the group refractive index $n_{g,0}$. The group delay (GD), an important figure, is defined as the variation of the spectral phase response $\phi$ as:

$$\tau_{\mathrm{g}} = \frac{d\phi(\omega)}{d\omega} \tag{2.4}$$

As for the second-order coefficient $\beta_2$, it is known the group velocity dispersion (GVD), which relates to the dispersion parameter $D$ in the indicated ways. In turn, $D$ parameter is expressed in function of GVD as $D = -\frac{2\pi c}{\lambda^2}\beta_2$. In other regards, without loss of generality, we may consider a lossy medium through a variable field amplitude. For instance, in order to account for the propagation loss, E is typically expressed as $\mathrm{E} = \mathrm{E}_0 \exp\left(-\alpha x/2\right)$, where $\alpha$ is the attenuation or propagation loss coefficient. It is, though, more common to express propagation loss in logarithmic scale, that would be given by the well-known simple relation:

$$\alpha_{\mathrm{dB}}\,[\mathrm{dB/cm}] = \alpha\left[\mathrm{cm}^{-1}\right] 10\log e. \tag{2.5}$$

In the direction of describing the OFDI system, let us consider now an interferometer (a MZI by default, as the TRIG-MZI in Fig. 2.1), where input light is split, travels along two paths of different lengths $l_0$ and $l_1$, and afterwards are put together and photodetected. By convention, we choose $l_1 > l_0$ and the PLD is $\Delta l = l_1 - l_0$. As the system involves 2 different paths for the light to propagate, it can be described in a two-dimensional matrix formalism. The input optical field would be given by a column vector, that in the case of input through 0 (upwards) and normalized, is $\mathbf{E}_{\mathrm{in}} = \binom{1}{0}$. The optical couplers carrying out split and combination of optical fields are described by a $2 \times 2$ matrix of the form:

$$\hat{M} = \sqrt{\gamma}\begin{pmatrix} \sqrt{1-\kappa} & i\sqrt{\kappa} \\ i\sqrt{\kappa} & \sqrt{1-\kappa} \end{pmatrix}, \tag{2.6}$$

where $\gamma$ represents the insertion loss of the optical coupler and $\kappa$ determines its power ratio. In turn, the uncoupled propagation can be represented by the following matrix:

$$\hat{P}_{0,1} = \begin{pmatrix} \mu_0 & 0 \\ 0 & \mu_1 \end{pmatrix} = \begin{pmatrix} e^{-\frac{\alpha l_0}{2}} e^{-i\beta l_0} & 0 \\ 0 & e^{-\frac{\alpha l_1}{2}} e^{-i\beta l_1} \end{pmatrix} \tag{2.7}$$

where $\beta$ is the propagation constant of the medium. In order derive the optical field at the output of the MZI, we only need to do the operation $\mathbf{E}_{\text{out}} = \hat{M}\hat{P}_{0,1}\hat{M}\mathbf{E}_{\text{in}}$ resulting into:

$$\mathbf{E}_{\text{out}} = \begin{pmatrix} E_{out,0} \\ E_{out,1} \end{pmatrix} = \gamma \begin{pmatrix} \mu_0 - (\mu_0 + \mu_1)\,\kappa \\ i\,(\mu_0 + \mu_1)\,\sqrt{\kappa}\sqrt{1-\kappa} \end{pmatrix}. \tag{2.8}$$

Once these fields are photodetected, the obtained trace (photocurrent) is proportional to the optical field intensity $I = |\mathbf{E}|^2$. The intensity can be divided into oscillatory and 'ground' contributions, $I = I_{\text{DC}} + I_{\text{AC}}$:

$$\begin{gathered} I_0^{\text{DC}} = \gamma^2 \left( (1-\kappa)^2 \, \mathrm{e}^{-\alpha l_0} + \kappa^2 \mathrm{e}^{-\alpha l_1} \right); \; I_1^{\text{DC}} = \gamma^2 \kappa\,(1-\kappa) \left( \mathrm{e}^{-\alpha l_0} + \mathrm{e}^{-\alpha l_1} \right); \\ I_0^{\text{AC}} = 2\gamma^2 \kappa\,(1-\kappa)\,\mathrm{e}^{-\alpha \frac{l_0+l_1}{2}} \cos(\beta \Delta l + \pi)\,, \\ I_1^{\text{AC}} = 2\gamma^2 \kappa\,(1-\kappa)\,\mathrm{e}^{-\alpha \frac{l_0+l_1}{2}} \cos(\beta \Delta l)\,. \end{gathered} \tag{2.9}$$

The DC terms depend on the accumulated optical loss per path, this is $\gamma^2$ for both, a complementary combination of $\kappa$, and the corresponding propagation loss given by $\alpha l$. In the symmetric limit where couplers are the same, unbiased, and propagation loss can be considered zero or at least, negligible the difference, the terms are the same and equal to $0.5\gamma^2$. Most interesting, the oscillatory or AC term, that is the same for both outputs except for a $\pi$ phase jump, determines the interference pattern. The amplitude of the cosine is given, as for the DC terms, by $\gamma$, $\kappa$ and waveguide loss. In the argument of the sinusoidal it is $\beta\Delta l$, that basically leaves two ways to generate an interference pattern: the direct way is by varying $\Delta l$, as it is the case in LCI technique mentioned in chapter 1 [34,35]. Alternatively, the way a frequency-domain interferometry as OFDI does is by varying $\beta \equiv \frac{n(\omega)\omega}{c} = \frac{2\pi n(\lambda)}{\lambda}$ through wavelength sweep, taking advantage of the almost linear variation of the refractive index (RI) of the propagation medium in the working band. This ultimately generates an interferogram sampled in wavelength, with the possible TL nonlinearities superimposed, that is reconditioned in the linearization process that we detail in the following section 2.3. If, beyond, we cannot consider a linear fashion of the implied RIs due to the presence of considerable chromatic dispersion, we shall have consequences in our measurements that we cover in section 2.4.

Let us consider now an interferometer where a DUT is inserted in one of the arms (DUT-MZI in Fig. 2.1), by convention in the shortest. The DUT has a given length $l_{\text{D}}$ and it is characterized by its transfer function:

$$H(\lambda) = |H(\lambda)| \exp(-i\beta_{\text{D}} l_{\text{D}}) \exp(i\phi_{\text{D}}(\lambda)) \tag{2.10}$$

where $\beta_{\text{D}}$ is the propagation, $\phi_{\text{D}}$ is the phase response of the DUT, etc. Its insertion can be accounted in the upper term of the propagation matrix above

$\hat{P}_{0,1}$. When doing so, after some algebra, the corresponding contributions of the interferograms are given by:

$$I_0^{\mathrm{DC}} = \gamma^2 \left( |H|^2 (1-\kappa)^2 \mathrm{e}^{-\alpha l_0} + \kappa^2 \mathrm{e}^{-\alpha l_1} \right) ; \; I_1^{\mathrm{DC}} = \gamma^2 \kappa (1-\kappa) \left( |H|^2 \mathrm{e}^{-\alpha l_0} + \mathrm{e}^{-\alpha l_1} \right) ;$$
$$I_0^{\mathrm{AC}} = 2\gamma^2 |H| \kappa (1-\kappa) \mathrm{e}^{-\alpha \frac{l_0+l_1}{2}} \cos\left( \beta \Delta l - \beta_{\mathrm{D}} l_{\mathrm{D}} + \phi_{\mathrm{D}}(\lambda) + \pi \right),$$
$$I_1^{\mathrm{AC}} = 2\gamma^2 |H| \kappa (1-\kappa) \mathrm{e}^{-\alpha \frac{l_0+l_1}{2}} \cos\left( \beta \Delta l - \beta_{\mathrm{D}} l_{\mathrm{D}} + \phi_{\mathrm{D}}(\lambda) \right), \tag{2.11}$$

where, of course, we may recover Eq. 2.9 in the limit where $H(\lambda) = 1$. In this case the interference fringes are modulated in amplitude by the DUT spectral response $|H(\omega)|$ and, most important, the phase response given by $\phi_{\mathrm{D}}$ gets tracked by the cosine in its argument. This is signature of an interferometric technique, its added value when compared to other more conventional experimental test as analyzing the device spectrum by using an optical broadband source and an OSA. Once everything concerning the interferograms is described, that is what is obtained in the measurements, in the next section we cover the next step, central in OFDI technique: the processing of the interferograms.

## 2.3 Interferogram processing

After all the measurement procedure, the proper processing of the measured interferograms is behind the correct interpretation of the temporal features that are observed in the time domain response of the DUT. This processing comprises the following parts: the linearization, where the interferograms are prepared to apply Fourier transform, the Fourier processing leading to the time domain response of the DUT, and the retrieving of amplitude and phase information in the time domain picture. Additionally, the spectral response of the whole DUT, or portions of it, can be recovered from it. We cover all the details in the following subsections.

### 2.3.1 Linearization and Fourier processing

The process in which OFDI technique leaves the DUT interferogram trace properly ready to be processed is called linearization. As mentioned before, OFDI is a swept-wavelength technique in which a TL source is used to scan a given band of width $\Delta\lambda$ centered at $\lambda_0$. This scanning, which lasts a certain amount of time depending on the TL scan speed $v_{\mathrm{TL}}$, is readily coordinated with the photodetection and capture of the resulting signal. However, in general, all the TL sources rely on a wavelength sweep and besides, manifest a certain degree of deviation from linearity during the scan. This, combined with a lot more precise electronic clock based DAQ, entails a problem in view of the requirements of a frequency-sampled trace that we would need in order to apply Fourier processing onto it. This gives the reason for being to the reference or triggering MZI: the resulting interferogram contains the same phase information as the DUT-MZI, but the DUT phase response itself. Therefore, by making the TRIG interferogram to provide the sampling points to the DUT, the corresponding phase frequency nonlinearities coming from both a wavelength sweep and the systematic plus random TL phase errors, cancels out, leaving a DUT trace linearly sampled in frequency.

There are two different options to capture the interferograms: on the one hand, in the direct sampling it can be choose the reference MZI to trigger the sampling of the DUT-MZI interferometer. Most of the commercial DAQs can do that fastly enough, being common to get 1 sample (S) per TRIG interferogram oscillation. More concisely, the growing zeros of the sinusoidal (i.e. the subset of the interferogram zeros with positive derivative). Conversely, as long as the DAQ sampling rate allows it, an indirect sampling approach can be employed: both interferograms can be captured simultaneously, sufficiently sampled to reproduce the corresponding sinusoidal traces, and store them to data. This approach is the more appropriated from a research point of view and the one that we use, in general, along this thesis work. It allows to observe a more complete image of the raw interferograms to observe its characteristics, at the cost of larger files and of course, requiring faster PD and DAQ sampling rate capabilities. Inherited from what commercial equipment typically does in the direct sampling and the bibliography, we have typically stick to the 1 S/TRIG oscillation approach.

In Fig. 2.3, an OFDI processing chart is shown, using as an example the traces corresponding to OFDI measurements and processing of a real device, a silica-based telecom grade arrayed waveguide grating (AWG) having 18 × 18 inputs/outputs and a FSR = 14 nm (this OFDI validation is one of the very first in this thesis, see section 3.1 in the following chapter). After an OFDI measurement of the central input/output of the AWG (number 9 in both cases), with wavelength sweep span $\Delta\lambda = 50$ nm around $\lambda_0 = 1545$ nm, at $v_{\mathrm{TL}} = 40$ nm/s and DAQ rate of $10^5$ S/s (this is the nominal DAQ rate we use in the experiments on the thesis, enough to resolve interferogram fringes at typical $v_{\mathrm{TL}}$), the DUT and TRIG captured interferograms are shown at the top left part of the figure, in blue and green curves, respectively. The DUT trace shows, as expected, a sinusoidal curve modulated by the wavelength resolved transfer function of the DUT, which is also present in the DC, as given by Eq. 2.11. In the window below, a zoom to a narrower region is shown. The linearization points given by the TRIG interferogram (in the 1 S/TRIG oscillation approach) provide the 6–7 re-sampling points to the DUT interferogram, represented in asterisk symbols. The mismatch between the original sampling points and this set is overcome by doing interpolation.

In order to account for the 1 S/oscillation criterion, we recall TRIG interferogram oscillatory part $I^{\mathrm{AC}}$ argument, given by Eq. 2.9, and take the growing zeros of this:

$$I_{\mathrm{TRIG}}^{\mathrm{AC}} \propto \cos\left(\beta_m \Delta l'\right) = 0^{+} \rightarrow \beta_m = \frac{1}{\Delta l'}\left(\frac{3\pi}{2} + 2\pi m\right), \text{ where } m \in \mathbb{Z} \tag{2.12}$$

is the interference order of the TRIG interferogram. This is a linear sampling in $\beta$ that entails a linear sampling in frequency too. By expressing $\beta$ and $\beta_{\mathrm{D}}$ according to Eq. 2.2 up to a first-order, the corresponding set of frequency re-sampling points $\nu_m$ is given by:

$$\nu_m = \nu_0 + \frac{1}{n_{\mathrm{g},0}} \left( \frac{c}{\Delta l'} \left( \frac{3}{4} + m \right) - \nu_0 n_0 \right); \tag{2.13}$$

where $\nu_0$, $n_0$ and $n_{\mathrm{g},0}$ are frequency, and effective and group RIs of the interferometer waveguides in the center of the band, respectively. On the other hand, the DUT interferogram AC part, that is given by Eq. 2.11, is of the form $I_{\mathrm{D}}^{\mathrm{AC}} \propto |H| \cos\left(\beta \Delta l - \beta_{\mathrm{D}} l_{\mathrm{D}} + \phi_{\mathrm{D}}(\lambda)\right)$. When introducing this set of points into the DUT propagation constant $\beta_{\mathrm{D}}$, we obtain:

$$\beta_{\mathrm{D},m} = \left( \frac{n_{\mathrm{g,D},0}}{n_{\mathrm{g},0}} \right) \beta_m + \frac{2\pi\nu_0}{c} \left( n_{\mathrm{D},0} - \frac{n_{\mathrm{g,D},0}}{n_{\mathrm{g},0}} n_0 \right), \tag{2.14}$$

i.e. the DUT propagation constant is linearly sampled as well, with a re-scaling factor and a shift given by the different RIs. If we substitute $\beta_m$ and $\beta_{\mathrm{D},m}$ expressions in the argument of the DUT interferogram, we finally have:

$$\begin{aligned} I_{\mathrm{D}}^{\mathrm{AC}} \propto |H(\nu_m)| \cos \Bigg( & \left[ \frac{3\pi}{2} \frac{\Delta l}{\Delta l'} - \frac{2\pi\nu_0}{c} \left( n_{\mathrm{D},0} - \frac{n_{\mathrm{g,D},0}}{n_{\mathrm{g},0}} n_0 \right) l_{\mathrm{D}} \right] \\ & + 2\pi \frac{\Delta l}{\Delta l'} m + \phi_{\mathrm{D}}(\nu_m) \Bigg) \end{aligned} \tag{2.15}$$

where the first is a constant phase term that depends on the propagation properties mismatch between DUT and MZI waveguides (we have included $l_{\mathrm{D}}$ in $\Delta l$ by doing $\Delta l - \frac{n_{\mathrm{g,D},0}}{n_{\mathrm{g},0}} l_{\mathrm{D}} \simeq \Delta l$). There is, as expected, the phase response of the DUT $\phi_{\mathrm{D}}(\nu_m)$, and the linear term in integer $m$ that traces interferogram oscillations. The last is an important point: a relationship between $\Delta l$ and $\Delta l'$ must be fulfilled for a correct sampling in the linearization. The well-known Nyquist criterion determines it, and imposes that a (sinusoidal) signal must be sampled above the Nyquist frequency, which equals to 2 S per oscillation. In order for the linearized DUT to accomplish it, it must occur that:

$$\Delta l' \geq 2\Delta l. \tag{2.16}$$

After the linearization is performed correctly, including the adoption of the Nyquist criterion, the discrete time inverse Fourier transform algorithm can be properly applied. In our case, we apply the built-in Fast Fourier Transform (FFT) algorithms in Matlab. In this way, the time domain picture is obtained, where $\Delta l$, $\Delta l'$, and the specific relation between them, determines the characteristics of the time domain window.

### 2.3.2 Time Domain

The time domain picture of the linearized DUT interferogram $I_{\mathrm{D}}^{\mathrm{AC}}$ in Eq. 2.15 is a complex vector $\tilde{H} = H(t) \exp\left(i\tilde{\phi_{\mathrm{D}}}(t)\right)$ that fulfills the common and well-established discrete Fourier transform properties. The whole temporal window is

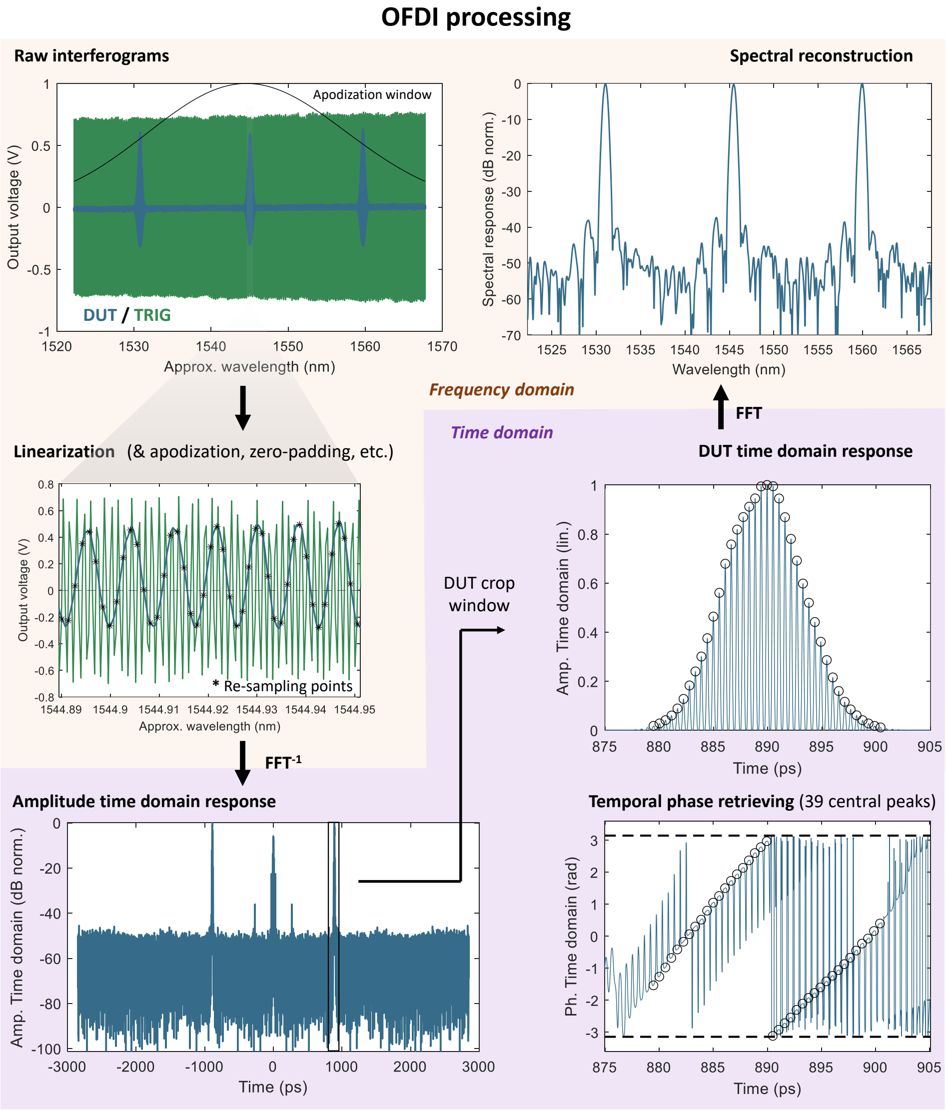

**Figure 2.3:** OFDI processing chart of a silica-based AWG: the interferograms are processed to obtain the AWG amplitude and phase in the time domain. The spectral response can be reconstructed.

symmetric with respect to the center of this trace, as shown in Fig. 2.3 at the bottom left, so information is repeated and only half of the window is used. For our explanation, we keep the right part, and we call it the temporal semi-window. $I_{\mathrm{D}}^{\mathrm{AC}}$ is a frequency-resolved trace of extent $\Delta\nu$ (or $\Delta\lambda$), and a pace $\delta\nu$ ($\delta\lambda$). The pace, that is determined by the TRIG-MZI $\Delta l'$ and the linearization criterion as given by Eq. 2.13, $\delta\nu = \frac{c}{n_{\mathrm{g},0}\Delta l'}$, leads to the size of the time domain window by recalling the time scaling property of the Fourier transform, as:

$$\text{Time domain window: } \left[-\frac{T}{2}, \frac{T}{2}\right], \text{ with } T = \frac{1}{\delta\nu}. \tag{2.17}$$

i.e. the extent of the semi-window is $T/2 = n_{\mathrm{g},0}\Delta l'/2c$. The corresponding axis in positions normalized to the DUT properties is obtained through $X = T\frac{c}{n_{\mathrm{g,D},0}} = \left(\frac{n_{\mathrm{g},0}}{n_{\mathrm{g,D},0}}\right)\Delta l'$. This is, the semi-window extent is given by $\Delta l'/2$ scaled to the DUT waveguides through the given group RIs ratio. Inside the temporal semi-window, assuming the DUT has a non-zero temporal width, depending on the signature of the DUT-MZI PLD, i.e. whether $\Delta l > 0$ or $\Delta l < 0$, the time arrow is going to the left or to the right, respectively. This is because for longer paths in the DUT, the PLD of the MZI gets lesser or greater, thus closer to the semi-window origin ($z = 0$) or to the edge $z = \frac{X}{2}$. The present contributions in the center of the temporal window correspond to the DC term of the interferogram.

Regarding the temporal peaks of the DUT amplitude time domain response $H(t)$, a central figure (specially when dealing with tiny integrated devices) is the spatial resolution of the system. The ideal spatial resolution $\delta z_{\mathrm{id}}$ can be directly deduced from the Fourier transform properties: in the same way that the time domain window size is given by the the frequency pace $\delta\nu$, the frequency span of the interferogram $\Delta\nu$ determines the temporal pace $\delta t$, whose spatial version is what is known as the ideal spatial resolution:

$$\begin{aligned} \text{Transmission mode: } \delta z_{\mathrm{id}} &= \frac{c}{n_{\mathrm{g}}\Delta\nu} = \frac{\lambda^2}{n_{\mathrm{g}}\Delta\lambda}, \\ \text{Reflection mode: } \delta z_{\mathrm{id}} &= \frac{\lambda^2}{2n_{\mathrm{g}}\Delta\lambda}, \end{aligned} \tag{2.18}$$

where in reflection mode, $\delta z_{\mathrm{id}}$ is doubled since the DUT is traversed twice by the light. A more formal deriving of $\delta z_{\mathrm{id}}$ can be found in [37], performed by doing the Fourier transform of a finite, clipped, cosine function (i.e. the cosine convolved with a squared function), that leads to a sinc function whose main lobe width is estimated to be $\delta z_{\mathrm{id}}$. This more formal discussion provides details of the temporal peaks shape. The secondary lobes are artefacts with no physical meaning that can interact with nearby contributions. The most intuitive way to reduce this effect, known as Gibbs phenomenon [61], is to apply an apodization window (e.g. a Gaussian one) to the DUT interferogram prior the FFT, as shown in Fig. 2.3. As this apodization gets stronger, the convolved function becomes a Gaussian and therefore, a transition from sinc to Gaussian is observed in the time-domain peaks. However, there is a trade-off between this secondary lobe reduction of the sinc and the reduced effective band span $\Delta\lambda$ when applying the apodization window, which in turn reduces the spatial resolution in the time domain, broadening the peaks.

Another important Fourier processing step is the zero-padding: the complex time domain response $\tilde{H}$ has the same number of elements as the linearized interferogram $I_{\mathrm{D}}^{\mathrm{AC}}$. In some situations, this point density might not be enough to resolve the structure of the temporal peaks. This straightforward and well-known Fourier processing strategy can be applied to mitigate it, and consists of surrounding $I_{\mathrm{D}}^{\mathrm{AC}}$ trace with zeros, prior the FFT. In this way, while no information is changed in the interferogram, the number of elements increases, resulting into a higher point density for the obtained $\tilde{H}$.

From a more physical point of view, the temporal window contains the time domain response of the DUT, which provides highly valuable information. In this picture, the sweep-wavelength OFDI experiment is equivalent to send a virtual optical pulse which travels the DUT and all the circuitry around, experiencing optical power split, following different paths, reflecting and transmitting onto different media interfaces by Fresnel reflection, etc. These results into the presence of a set of contributions, manifested in form of peaks in amplitude, carrying the following information:

**Position** The most evident information of a temporal event is its position (either in time or spatially). This information allows to identify its origin. Some events are expected either coming from the DUT, the chip formed cavities, etc. but any other unexpected events taking place will appear in the temporal semi-window as well. Considering a pair of expected peaks, separated $\Delta t$ and for which the length difference $\Delta x$ is known by design, the average group index of the chip waveguides in the working band can be deduced as:

$$n_{\mathrm{g},0} = c\frac{\Delta t}{\Delta x} \tag{2.19}$$

where $c$ is the speed of light in vacuum.

**Shape** Given an apodized DUT interferogram, the ideal shape of the peaks is Gaussian. However, several causes can provoke the distortion of its shape. One of the main reasons has to be with the typically high chromatic dispersion of the integrated waveguides, leading to the temporal broadening of the contributions (for more details, see next section). This cause is fairly easy to identify when having a number of consecutive contributions, as it is a length cumulative phenomenon. An alternative source of distortion may be to have different waveguide cross section transitions like, for example, the tapers used for mode matching in horizontal coupling to the chip. This sections are wider and, probably, of multi-mode regime, so some coupling between different $n_{\mathrm{eff}}$ propagation modes may occur leading to a slightly delayed combination of peaks. In case of an unexpected peak, given a distorted shape may indicate it is taking place at a delay beyond the temporal semi-window, thus aliased.

**Amplitude** Provided that the peaks are isolated enough from each other, each peak amplitude can be evaluated and compared to other peak amplitudes. This allows to retrieve varied information about loss in the chip and the DUT, and even conceive intended test structures relying on this principle to assess important parameters (see next chapter). Besides and remarkably, regardless of the peak shape, the peak amplitude can be integrated over its width.

**Phase** Where the events are localized, the corresponding optical phase response $\tilde{\phi}_{\mathrm{D}}$ can be retrieved [62]. Similarly as described for amplitude, the phase between the different contributions can be compared to get valuable information about the DUT. For example, as shown in Fig. 2.3 at the bottom left, the time domain phase corresponding to the 39 central AWG array waveguides (depicted in black circles) can be computed to evaluate the degree of phase error of the real device. Furthermore, relative phase assessments can be compared from one take to another (more on relative phase measurements in the next chapter).

It is possible to retrieve absolute magnitudes from the time domain response. This implies to build an OFDI setup with all its parts carefully characterized and controlled, requiring a thoughtful maintenance. These parts include the optical power loss along the MZIs, the associated loss in the chip coupling, a precise absolute wavelength referencing, the PDs electro-optical response, amongst others. In this way, by relying on Plancherel theorem, amplitude temporal information can be scaled to optical magnitude units. However, even with commercial equipment [40], consecutive takes of the same measurement provide different phase response in absolute terms, since this is a fragile information, very sensitive to the immediate external conditions. In our OFDI, we decided not to make such efforts in this direction, and take advantage of what we believe is one of the strongest points of the technique: in the same measurement take, we have at our disposal the different contributions taking place in the chip (DUT). This makes the different contributions time domain amplitude and phase to be comparable between them in a very robust, inherent way. Absolute values of amplitude may be of interest. However, in case of being interested, it is a smart strategy to relate the amplitude of a temporal contribution externally to a given value. Once that is done, the rest of the temporal contributions can be referenced to it.

As a final point of this section, we briefly explain an interesting processing strategy. So far, the described OFDI processing is done for a given span $\Delta\lambda$, which means the time domain response observed features and retrieved informations are correspondingly averaged. If the wavelength dependance of any information is desired, a piecewise OFDI processing approach may be adopted. Basically, it consists in dividing the whole available band $\Delta\lambda$ into a number of pieces, smaller sub-bands, either by individual sweeps or by slicing the whole interferogram. As long as the spatial resolution is enough for the specific purpose of the processing, independent OFDI processing can be applied to each of them and time domain group of traces are obtained. Whatever it is the retrieved information, it is now obtained for different wavelength centers $\lambda_{0,i}$, distributed along the $\Delta\lambda$ band. If some more spatial resolution is needed, these sub-bands do not need to be perfect slices, but some coupling between them is perfectly acceptable, at the cost of some wider wavelength averaging. To see an example of this kind of processing, see section 3.3.2 in the next chapter.

### 2.3.3 Spectral reconstruction

From Eq. 2.11, the DUT interferogram itself contains the whole spectral response $|H(\lambda)|$ in its envelope. It is added to a DC contribution proportional to $|H(\lambda)|$, and strictly speaking, contains the whole casuistry taking place along the DUT arm (external fiber response, in and out coupling to chip, etc.) with respect to the reference arm of the MZI. As previously described, after linearization and Fourier processing the time domain response of the DUT provides a set of temporal contributions represented by peaks in amplitude with an associated phase trace. It also contains contributions coming from other features taking place in the DUT arm of the MZI. In order to reconstruct the DUT response in an isolated way, a crop function (i.e. a temporal filtering window) can be defined for the DUT response. Again, with the aim to avoid Gibbs phenomenon effect of sharp borders [61], an apodization window can be applied to it. Once this is done, similarly as done when obtaining the time domain response, we can apply FFT to recover the spectral response of the DUT, both in amplitude and phase. In this reconstruction, unwanted temporal contributions are discarded so a purer trace of the spectrum of the DUT is obtained. Since the temporal crop window can be arbitrarily defined, even any desired subset of the DUT contributions can be chosen for the reconstruction. An example of amplitude spectral reconstruction is find for the example AWG in Fig. 2.3 at the top right.

Apart from a crystal clear DUT amplitude spectrum visualization, there are another scenarios where this processing step is useful related, according to our experience, to daily photonics experimental tasks. There are situations where, for a variety of reasons, the DUT response optical power is weak and pretty close to the OFDI system noise floor. In the interferogram, it is noted by noise oscillations in the order of the DUT ones. In the time domain, the temporal contributions are partially or totally undertaken in the noise floor making them bad defined and hard to distinguish from noise. For instance, this might be case of a reflectometry experiment interrogating a weak Bragg grating (BG). The amplitude response of these devices in the time domain are wide contributions corresponding to the back-reflected field along the BG length. The shape of this amplitude contribution provides a mean to identify whether the BG design has been the expected, e.g. a constant or a Gaussian profile. However, if this contribution is weak and difficult to identify in the time domain, as BG are filters with a given bandwidth around

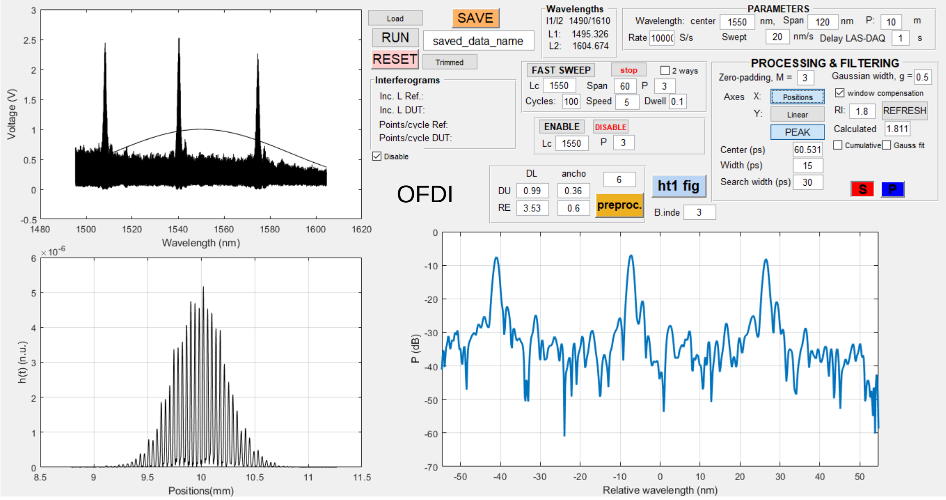

saved_data_name

**Wavelengths**
l1/l2 1490/1610
L1: 1495.326
L2: 1604.674

**PARAMETERS**
Wavelength: center 1550 nm, Span 120 nm P: 10 m
Rate 1000( S/s Swept 20 nm/s Delay LAS-DAQ 1 s

**Interferograms**
Inc. L Ref.:
Inc. L DUT:
Points/cycle Ref:
Points/cycle DUT:
☑ Disable

FAST SWEEP ☐ 2 ways
Lc 1550 Span 60 P 3
Cycles: 100 Speed 5 Dwell 0.1

Lc 1550 P 3

DL ancho 6
DU 0.99 0.36
RE 3.53 0.6
B.inde 3

**PROCESSING & FILTERING**
Zero-padding, M = 3
Gaussian width, g = 0.5
Axes X: Positions
Y: Linear
☑ window compensation
RI: 1.8
Calculated 1.811
☐ Cumulative ☐ Gauss fit
Center (ps) 60.531
Width (ps) 15
Search width (ps) 30

**Figure 2.4:** OFDI measurement and processing developed GUI in Matlab screenshot.

a single $\lambda_{\mathrm{BG}}$, one way to certify its presence is by defining little crop windows around the candidate contributions and systematically reconstruct its spectrum. When hitting the target, the characteristic notch at $\lambda_{\mathrm{BG}}$ should be visualized in the spectral reconstruction.

Another scenario where spectral reconstruction is useful is the following: to trace frequency phase response variation (i.e. the GD defined in Eq. 2.4) systematically from single temporal contributions provides a mean to get important optical parameters about the propagation of light along the DUT waveguides. As explained above, there are difficulties and some ambiguity around computing absolute phase, as well as amplitude, assessments with OFDI, more concretely with a setup of our characteristics. However, relative information comparing values from the same measurement take can be always retrieved. This idea has allowed us to develop a technique to assess chromatic dispersion of integrated waveguides from relative measurements of the spectral phase reconstruction, amongst other interesting parameters. This technique is covered in detail in chapter 3, section 3.2, of this thesis manuscript.

During the thesis, a graphic user interface (GUI) application has been developed to control all the OFDI system, from measurement to basic processing. This application is developed in Matlab, and a screenshot of it is shown in Fig. 2.4. The application communicates with TL source and DAQ to execute a measurement under the user parameters. The captured interferograms are shown in the window at the top, along with other items as for example, the apodization window or the TL sweep ramp, that allows the user to check whether the take is OK. An automatic processing is performed, again under the specified parameters, and the time domain response is obtained, and shown in the window below. This window axes can be manipulated to visualize the response in linear / logarithmic scale, and in time or positions. A crop window can be defined in a region of the time domain and the corresponding spectral reconstruction is shown in the window at the right. Each take can be saved to disk, and in turn, the application can load each saved data for a fast processing review.

## 2.4 Chromatic Dispersion

Due to the fact OFDI is a frequency/wavelength domain interferometric technique, the presence of chromatic dispersion affects the measurements. Different scenarios can be contemplated, depending on whether there is significative dispersion on the DUT and both interferometer waveguides, as well as the relation between them. In the case of using an external fiber-based OFDI to test integrated devices, there is typically a great dispersion offset, while in the integrated OFDI that we deal with in chapter 4 we have a particular case where propagation properties are almost the same for DUT and interferometer waveguides, having its implications and particularities. Let us analyze in this section what are the effects in these regards.

The presence of chromatic dispersion in the waveguides of the DUT manifests as a quadratically varying phase in the DUT interferogram, as given by $\beta$ model in Eq. 2.2 through $D$ parameter, and it is superimposed to all other phase contributions. Thus, for a given wavelength span $\Delta\lambda$ around $\lambda_0$, the interferogram FSR varies in a given longer range. FSR of the fringes, which in the ideal case is univocally related to a given PLD, and in turn to a position in the time domain for the corresponding contributions, is now a broader quantity implying a broader region for all the temporal peaks. In other words, this is the temporal broadening effect of a dispersive light pulse. Since the temporal peak width determines the spatial resolution of the system, this is affected by DUT waveguides dispersion [37] as given by:

$$\delta z_{\mathrm{disp}} = \sqrt{1 + \left(\frac{c\Delta\lambda^2 Dz}{4\pi\lambda_0^2}\right)^2}\,\delta z_{\mathrm{id}}, \tag{2.20}$$

where $\delta z_{\mathrm{id}}$ is given by Eq. 2.18, and $z$ is the associated length in the time domain. In Fig. 2.5, ideal and dispersive spatail resolutions are plotted in dashed and bold curves, respectively, against wavelength span $\Delta\lambda$. For this example, CNM silicon nitride platform [1] waveguide parameters has been used, measured in this thesis, having $n_{\mathrm{g},0} \simeq 1.89$ and $D = -1.43$ ps/(nm m). Spatial resolution is poor, presenting high numbers for very narrow wavelength spans ($< 15$ nm), as expected. In these cases, dispersion does not affect too much since it is a multiple-wavelength phenomenon. Therefore, as $\Delta\lambda$ increases, even though there is an improvement in the spatial resolution in the presence of dispersion, it starts differing from ideal value. In fact, this reduction of $\delta z_{\mathrm{disp}}$ experiences a minimum given by:

$$\delta z_{\mathrm{disp,min}} = \frac{\lambda_0}{n_{\mathrm{g}}}\sqrt{\frac{c\,|D|\,z}{2\pi}}, \text{ for } \delta\lambda_{\mathrm{min}} = \sqrt{\frac{4\pi\lambda_0^2}{c\,|D|\,z}}, \tag{2.21}$$

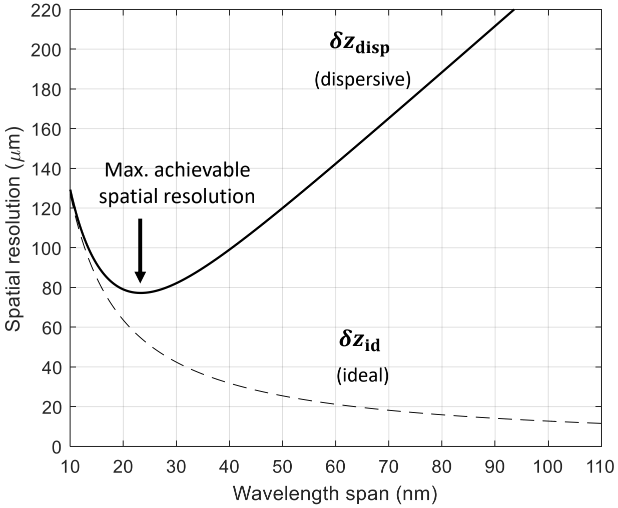

**Figure 2.5:** Ideal versus dispersive spatial resolution in OFDI for DUT waveguides of CNM technology platform [1] as example.

i.e. the maximum achievable spatial resolution. From that point on, chromatic dispersion dominates and $\delta z_{\text{disp}}$ increases with $\Delta\lambda$. This is the principal effect of chromatic dispersion in OFDI measurements: although ideally spatial resolutions close to 10 µm can be achieved for sufficiently broad sweeps around 100-120 µm, the typically high dispersion of integrated waveguides limits this figure to very high values (around 77 µm in our example), which in turn is critical to resolve temporally the commonly spatially near events of the integrated devices. In these cases, some post-processing must be carried out to de-embedd dispersion, as for example by substracting a dispersive phase model in the interferograms by search-algorithm until reaching the ideal spatial resolution [47]. However, specially if a 'brute force' search is performed, some care must be taken: as we have observed in numerical simulations, given two nearby peaks there are phase situations (different than the one representing the actual dispersion) under which the peaks, instead of destroying each other in amplitude, get in phase resulting into an apparent amplitude dispersion compensation.

Let us examine an OFDI system where we have optical fiber for the interferometers, and consider a DUT with different and higher dispersion. Chromatic dispersion is related to the nonlinear variation of the refractive index $n(\lambda)$ with frequency/wavelength in the working band. We account for it through a nonlinear definition of the propagation constant by invoking the $\beta$ series expansion in Eq. 2.2. Let us consider an OFDI experiment where a DUT having a trivial phase response ($\phi_{\text{D}} = 0$), a propagation constant $\beta_{\text{D}}$ different from the MZI waveguides $\beta$, and a physical length $l_{\text{D}}$, is embedded in a MZI with $\Delta l$. We assume a second-degree model for both $\beta_\mathrm{D}$ and $\beta$. In this way, the TRIG-MZI defined by $\Delta l' > \Delta l$ provide the linearization sampling points given by condition in Eq. 2.12:

$$\beta_0 + \beta_1 \Delta\omega_m + \frac{1}{2}\beta_2 \Delta\omega_m^2 = \frac{2\pi m}{\Delta l'},\ m \in \mathbb{Z}. \tag{2.22}$$

By solving this equation for $\Delta\omega_m$, we obtain:

$$\begin{gathered}\Delta\omega_m = -A_1 \pm \sqrt{A_1^2 - 2A_0 + \delta m},\ \text{where:}\\ A_0 = \frac{\beta_0}{\beta_2};\ A_1 = \frac{\beta_1}{\beta_2};\ \delta = \frac{4\pi}{\beta_2 \Delta l'},\end{gathered} \tag{2.23}$$

i.e. the $\omega_m = \omega_0 + \Delta\omega_m$ points we are resampling and employing for linearization process. Strictly speaking, this set is observed not to be exactly linearly spaced.

On the other hand, we consider DUT interferogram AC part $\propto \cos\left(\beta\Delta l + \beta_\mathrm{D} l_\mathrm{D}\right)$ in which we substitute the $\beta$ and $\beta_\mathrm{D}$ models. The cosine argument:

$$\begin{gathered}\Phi_\mathrm{D} = F_0 + F_1 \Delta\omega + \frac{1}{2} F_2 \Delta\omega^2,\ \text{where:}\\ F_i = \beta_i \Delta l + \beta_{\mathrm{i,D}} l_\mathrm{D},\ i = 0, 1, 2.\end{gathered} \tag{2.24}$$

When substituting sampling frequencies of Eq. 2.23 into this, the argument leaves:

$$\begin{gathered}\Phi_\mathrm{D,m} = \left[F_0 - F_1 A_1 + F_2\left(A_1^2 - A_0\right)\right] + \left[\frac{1}{2}F_2\delta\right] m\\ \pm\left[F_1 - F_2 A_1\right]\sqrt{A_1^2 - 2A_0 + \delta m}.\end{gathered} \tag{2.25}$$

One can easily notice from here that, analytically, the only way the nonlinear $m$ term vanishes is when $F_1 \simeq F_2 A_1$, i.e. when the proportion between the first and second order accumulated phases is the same for the MZI and DUT waveguides, something that is not true in general. However, we can rearrange the square root argument, that depends on the MZI waveguides propagation coefficients, as $A_1\sqrt{1 + \frac{\delta m - 2A_0}{A_1^2}} = A_1\sqrt{1 + 2\frac{\beta_2}{\beta_1^2}\Delta\beta}$. In the case of optical fiber and the typical sweeps of about $\Delta\lambda = 100$ nm around $\lambda = 1550$ nm, it is easy to see that $2\frac{\beta_2}{\beta_1^2}\Delta\beta \ll 1$ and, therefore, we may use the linear series approximation $\sqrt{1+x} \simeq 1 + x/2$. When assuming this approximation, $\Phi_\mathrm{D}$ becomes linear in $m$:

$$\Phi_\mathrm{D,m} = \text{constant} + \frac{\delta}{2}\left[F_2(1 \mp 1) \pm \frac{F_1}{A_1}\right] m. \tag{2.26}$$

We want now to know, under these circumstances, what is the OFDI measured accumulated dispersion for the DUT, i.e. $[\beta_2 L]_\mathrm{meas}$. To evaluate this, we can estimate it as the second derivative of the retrieved phase in the frequency domain $\Phi_\mathrm{D,m}$ with respect to the angular frequency $\Delta\omega_m$, which is the ideal derivation step. Therefore,

$$[\beta_2 L]_\mathrm{meas} = \frac{d^2\Phi_\mathrm{D,m}}{d\Delta\omega_m^2} = \frac{\delta}{2}\left[F_2(1 \mp 1) \pm \frac{F_1}{A_1}\right] m'', \tag{2.27}$$

where $m'' = \frac{d^2 m}{\Delta\omega_m^2} = \frac{\Delta l' \beta_2}{2\pi} = \frac{2}{\delta}$. By substituting all the coefficient definitions (and keeping to the valid solution, the one that does not make fade $F_2$ above), we get:

$$[\beta_2 L]_{\text{meas}} = \left(\beta_{2,\text{D}} - \beta_2 \frac{\beta_{1,\text{D}}}{\beta_1}\right) l_{\text{D}}. \tag{2.28}$$

This is an important result: with an external fiber-based OFDI setup, the measured dispersion is a slightly underestimated value of the DUT dispersion $\beta_{2,\text{D}} l_{\text{D}}$. Roughly, the subtraction between DUT and fiber dispersions (weighted by the fiber and DUT group indexes ratio), being fiber dispersion low and well-known. This result is in perfect accordance to OFDI numerical simulations we have performed and evidences that the DUT dispersion can be measured with OFDI, as we propose in next chapter, section 3.2.

## 2.5 Light Polarization

Even considering just the single-mode regime for both the interferometer optical fibers and the integrated waveguides, the light propagation can be understood as a superposition of two polarization fields, denoted transverse electric and magnetic (TE and TM), indicating the electric field oscillating along one of the two axes of the plane perpendicular to the light propagation direction. Single-mode optical fibers hold an hybrid mode which can be interpreted as the superposition of the two degenerate TE and TM modes, ideally identic and orthogonal due to circular simmetry. Small birefringence is present though due to slight assymetries in real fibers, leading to polarization-related phenomena such as polarization mode dispersion, which causes crosstalk [63]. Something similar occurs with integrated waveguides. In this case, the rectangular single-mode regime waveguides are more or less birefringent depending on whether the cross section is squared or not By convention, in the case of integrated waveguides, the TE mode corresponds to the (quasi) linear-polarized mode along the chip plane (horizontal axis in the cross section picture), whereas TM mode corresponds to the orthogonal (vertical axis). Similarly as with optical fibers, polarization coupling or rotation happens with special impact in small radius bend cross sections (small in relation to the electromagnetic field confinement, weak in fibers and much pronounced in high-contrast integrated technologies).

The OFDI setup developed during this thesis is not a polarization diverse measurement system. However, we make partial setup approaches that allow to study polarization-related behaviour and alleviate their negative effects on light interference. Regarding polarization control over the DUT, input and output polarization to a chip can be controlled by employing the coupling strategy shown in Fig. 2.6(a). In a mounted stage, guided light from the optical fiber is delivered to free-space collimated propagation. In this stage optical path, light passes through a linear polarizer, consisting of a thin layer of sodium-silicate that absorb light not aligned to the transmission axis of the polarizer. The input fiber polarization state is controlled by means of fiber polarization controller prior to the stage (not

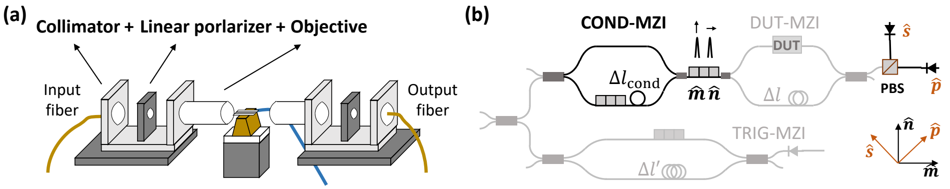

**Figure 2.6:** (a) Chip input/output controlled polarization coupling approach, employing stage including fiber collimator, linear polarizer and objective. (b) Optical vector analyzer, modified polarization-diversity OFDI setup.

shown in this figure, P1 in Fig. 2.1), so that transmission light power can be maximized. The same mounted stage is set at the output of the chip, so that TE or TM mode coupling and output filtering can be ensured. This kind of survey, that provides the four possible polarization combinations, permits to study light polarization features of the DUT in detail.

Polarization state of light in the MZI arms affect light interference. The misalignment of the polarization states of the superimposed light cause interference fringes fading. And specially in optical fiber, polarization state is unstable. Due to their weak guidance regime, any physical movement and bend in the fiber pigtails entails a change in the polarization state. It is also strongly affected by the external conditions of pressure and temperature, although this is not a big deal in OFDI due to the fast few seconds measurement takes. It must be taken into account as well the wavelength dependance of these polarization state concatenated rotations along the MZI arms. Taking this into consideration, the fiber setup must be kept minimal, with not too tight fiber bends, and fixed during the measurement take. Then, given the arbitrary polarization state in the DUT arm, employ a polarization controller in the reference arm (P2 in Fig. 2.1) and find the aligned polarization state that maximizes the fringes amplitude. The same strategy can be applied to the TRIG-MZI as well, with the advantage that any of its optical paths need to be changed during a measurement session and no additional DUT optical loss is present. A different approach to deal with this is explained in [39], where the authors propose to use a polarization beam splitter (PBS), as if it were a sort of polarization differential detection, as represented in Fig. 2.6(b) at the right part. Even though the splitting polarization basis is arbitrary, both captured processed traces can be combined in the processing a full time domain response picture. Besides, some information about the polarization rotation taking place in the device can be obtained in the frequency domain. Beyond, polarization-maintaining optical fibers may be considered to find more stability in the interferometric part of the setup.

Finally, for a working polarization diverse OFDI characterization, there exist the so-called optical vector analyzer (OVA), which is described in [64] and physically implemented in a Luna Technologies Inc. commercial product [40]. As shown in Fig. 2.6(b), the OVA is a modified OFDI setup that basically includes an additional MZI inserted serially prior the DUT-MZI. This polarization conditioning

MZI is intended to prepare the state of light entering the DUT-MZI: by controlling the polarization states of both arms of it, interference fringes are minimized, meaning their output light polarization states are orthogonal, along the vectors of a given arbitrary basis $\{\hat{m}, \hat{n}\}$. Besides, it is an unbalanced MZI with PLD $\Delta l_{\mathrm{cond}}$, so that two orthogonal and delayed light signals enter the DUT-MZI. These two orthogonal polarization interrogate the DUT and, after that, the resulting interferogram is again split into orthogonal polarizations of a different basis $\{\hat{s}, \hat{p}\}$, through the use of a PBS, similarly as explained above. An additional polarization controller is used in the middle of both MZIs to rotate $\{\hat{m}, \hat{n}\}$ and ensure an even splitting of this basis onto $\{\hat{s}, \hat{p}\}$, thus forming a $\pi/4$ angle. As a result, there are two different interferograms for the DUT, each of them containing two versions of the time domain response of the DUT, constituting the four complex elements of the DUT transfer function (a rotated version of it). As detailed in [64], these elements can be related between them for visualization and for obtaining important polarization-related parameters, in addition to the conventional, such as GD or polarization mode dispersion (PMD)

In the development of this thesis, this OFDI modified setup was studied in detail and partially implemented. However, due to the fact that this implementation is more demanding technically speaking (more channels to be acquired, permanent and time-consuming calibration of the system, etc.), we decided to leave it. Conversely, in the philosophy of a simple OFDI implementation, we addressed successfully the polarization negative issues and polarization DUT phenomena by means of the techniques described above, many times comparing the results to commercial OVA measurements showing a great level of agreement.

## 2.6 Conclusions

Along this OFDI introductory chapter, we provide what in our experience are the pillars of OFDI technique to test integrated devices. After many iterations and test, we built a fully-developed and functioning OFDI setup in the laboratory, as described in 2.1, that has become a really valuable tool in our labs. When compared to other common laboratory equipment like OSA, providing spectral response of the integrated DUTs, OFDI additionally provides the time domain response, both in amplitude and phase. This is the strong point in this thesis: when dominated, this information reveals as extremely useful to optically test PICs, waveguides and devices integrated on chips, that are fabricated in relatively mature technologies but still under development and thus, presenting fabrication errors. Not only that, in our research the access to the time domain picture of the DUTs has opened us the door to develop all the characterization applications in this thesis work, covered in the following chapters.

We provide an extensive explanation of the OFDI processing in section 2.3. The important linearization process, which makes necessary the existence of the TRIG interferometer and prepares the interferograms to be transformed to the time domain picture. After that, the receipt to understand all the features appearing in this picture are given. In the two last sections, two important light characteristics considerably affecting OFDI, chromatic dispersion and light polarization, are covered. Indications on how to deal with them are provided. However, it is not a surprise at all that there are some points regarding both the OFDI setup and the processing susceptible to be revisited and improved, either because we missed them in the way, we postponed them in favor of other developments (because maybe we did not need it by the time), or we just did not get to them yet.

Amongst all of them, those points that are related to the foundations or the processing are more in position to be immediately implemented. For example, a relevant one concerns the sampling strategy in the linearization. In the first steps of our OFDI setup, we adopted 1 S/TRIG oscillation and we stuck to it along the thesis, together with an indirect sampling approach. The reason we use this criterion in the first place is that, as argued in this chapter, most of the commercial DAQs have the capability to make direct sampling at that rate, i.e. by taking the growing zeros of the TRIG sinusoidal, so we inherited it. However, in the indirect sampling, the TRIG interferogram is resolved and nothing prevents to raise the number of sampling points. For example, this number can be easily doubled by taking the decreasing zeros of the sinusoidal too, and even higher rates may be considered to be implemented, always taking care of not make phase error mistakes. Bearing in mind the Nyquist criterion, the number of sampling points we take per TRIG oscillation directly impacts on the required PLD of the TRIG-MZI. We conserved the 1 S/TRIG oscillation criterion in our OFDI setup just because there was not urgency of revision: fiber has low loss, its footprint is not relevant, the TL linewidth has quality enough and the photodetection part is sufficiently fast to resolve the TRIG fringes. Nonetheless, even though with an external OFDI setup this possible update is not specially relevant, it has quite stronger implications when considering an integrated OFDI structure as covered in chapter 4. The footprint and high loss of the large integrated spiral waveguides length, implementing the required PLDs, have a considerable impact. Just going to the straightforward 2 S/TRIG approach would allow to reduce them roughly to a half. Beyond, related to the topic of linearization, other interesting approaches are in the literature that may be investigated, e.g. [65].

On the other hand, there are some refinements at a setup level that, for some of the reasons aforementioned, we did not implemented at the thesis time. A good example of this is the adaptation of the OFDI setup to the OVA approach described in section 2.5 that, as mentioned there, we tried and left since it entails a trade-off between setup complexity and real demands of our research targets. Other point which has to do with the hardware part is the adoption of a high-quality absolute wavelength referencing. During this thesis, we used the electric ramp provided by the used TL for wavelength referencing, providing the starting and final sweep wavelengths. Although it has been enough for our purposes, there are more serious approaches which may be employed, e.g. make use of an Hydrogen Cyanide gas-cell [39].

As a final point, in situations where an OFDI measurement as described in previous sections (i.e. by measuring interferograms through just one MZI output) lacks of sufficient power, the well-known differential detection may be adopted to the OFDI setup as a possible solution. It basically consists of measuring both MZI outputs (0 and 1 in Fig. 2.1) and, after that, subtract them. In this way, if we invoke Eq. 2.11 and do the operation $I_1 - I_0$, we achieve reduction of the DC part (in fact, in the best case where $\kappa = 0.5$ it goes to zero) so as to enlarge the AC part in a factor 2. Conversely, the main drawback when using differential detection is that we need to get an additional output take. Not only that, exactly as it happens with the OVA approach in the preceding subsection, for the sake of precision we would need to assure that the two involved PDs has the same responsivity, something generally untrue even the PDs being the same model. As well as with the DAQ output voltage, that it is not trivial either as we have observed in the laboratory when pushing the DAQ to its sampling limit (e.g. when testing the OVA approach in the laboratory). As sampling rate gets to the limit, electrical phenomena like channel signal ghosting happens and the order in which these are defined for the measurement session begin to be important, adding complication to the measurement system.

# Chapter 3
# OFDI applications in PICs

In this thesis work, after the first steps of learning about optical frequency domain interferometry (OFDI) technique doing bibliography review and having built an OFDI setup, the first tests were performed. Apart from a fiber pigtail (the most trivial device under test, DUT), the very first test over more complex devices was performed for a telecom grade arrayed waveguide grating (AWG), fabricated on silica technology, a friendly case given the quality of a commercial device on a mature technology. After that, other AWG models were tested in different photonic integration technologies, silicon-on-insulator (SOI) and indium phosphide (InP), and the results are part of a past PhD thesis of our group [66]. Besides, in the same period of the thesis, other integrated devices were tested involving interferometers and thus, different light paths followed, multimode interferometers (MMI), etc. All these results were gathered in a conference paper [67] and we review them in section 3.1

Ring resonators (RR) are central devices in photonic integrated circuits (PIC) and concretely in our thesis work, where they are employed as test structures: the multiple recirculations provide a rich time domain picture where we are able to observe polarization-related phenomena. Further, they are suitable to retrieve multiple optical parameters related to the RR propagation, as chromatic dispersion of the RR waveguides, and about the coupler characteristics, simultaneously. Results on this are reported for RRs in silicon nitride (SiN) and silicon-rich nitride in conferences [51, 52], as a part of a publication [10], and reviewed in section 3.2.

Afterwards, waveguide propagation loss with OFDI, and optical coupler characterization, are addressed in the next section. Considering a technique reported in [41], we revisited it allowing us to test propagation loss of integrated waveguides in different technologies employing the reflectometric mode of our OFDI setup. Some results of this work are part of some publications by our research group as [10, 68]. The results are analyzed in detail in the context of a technology characterization in a thesis work of our group [11]. We review the technique in section 3.3.1. Next, we cover an application proposal to characterize waveguide

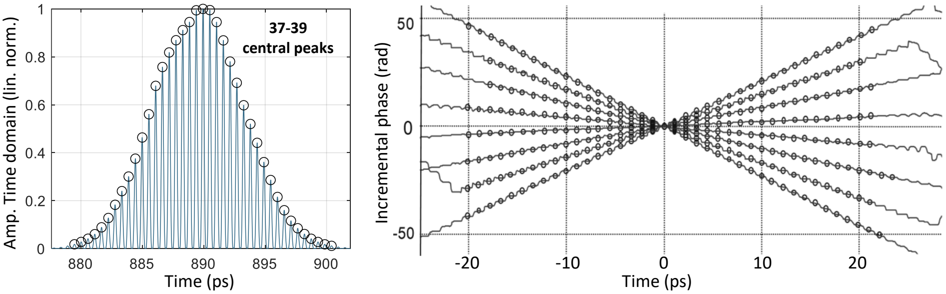

**Figure 3.1:** At the left, the amplitude time domain response of the silica-based AWG, output 9. At the right, the unwrapped temporal phase traces for outputs 1,3,5,7,9,11,13 and 15, referenced to the central waveguide. In both plots, waveguide positions are highlighted with black circles.

propagation loss and characterize power splitting ratio of optical couplers in 3.3.2. This work is reported in conference [53] with description, theoretical and numerical analysis, and no experimental results. However, the technique was experimentally validated with success in the context of a private research project [69] and other collaborations in our research group.

In the final section, we delve further into OFDI relative phase measurements, introduced in section 2.3.2 and carried out in several parts of this thesis. Here, we cover two cases where phase retrieving has allowed us to characterize metal heaters and chip heat crosstalk.

## 3.1 First validations of OFDI with integrated devices

In this first section, we cover the first relevant OFDI tests over integrated devices in this thesis work, which took place during the development of the OFDI setup. Although they are not the only tests, they were the chosen for a conference communication [67]

On the one hand, we tested a silica-based telecom grade AWG, whose OFDI processing is shown as an example in Fig. 2.3. As mentioned, the AWG has $18 \times 18$ inputs/outputs, FSR $= 14$ nm and OFDI measurements are performed for $\Delta\lambda = 50$ nm around $\lambda_0 = 1545$ nm, at $v_{\mathrm{TL}} = 40$ nm/s tunable laser (TL) scanning speed and digital acquisition card (DAQ) rate of $10^5$ S/s. In that processing chart, the AWG measurement corresponding to the central input and output (number 9) is shown in the different stages: DUT and TRIG interferograms, the time domain response both in amplitude and phase, and the amplitude spectral reconstruction.

In the time domain amplitude response (shown also in Fig. 3.1 at the left) the expected Gaussian shaped train of pulses is perfectly observed with a peak separation of 0.55 ps, according to the FSR device specification. The resolution of the measurement, which is about 0.18 ps, is enough to resolve the peaks and no secondary lobes are observed since a Gaussian apodization is used prior the inverse fast Fourier transform (FFT). The time domain phase can be computed to assess the incremental phase between the waveguides in the array, that ideally should follow a linear trend that, otherwise, is detrimental to the AWG spectral behaviour, affecting the main to secondary lobe ratio (MSLR) and the dynamic range [19]. To do so, as shown in Fig. 2.3 at the bottom left, the raw phase trace comes wrapped in the $-\pi$ to $\pi$ region. To compute the phase corresponding to each contribution, the phase must be evaluated at the corresponding waveguide positions indicated by the black circles and take into account the $2\pi$ phase jumps. Then, the incremental phase is obtained by subtracting them. Besides, as we argued in section 2.3.2, there is a global phase contribution coming from the setup that varies from one measurement take to another, so referencing to one of the contributions is performed. In the case of this AWG, in Fig. 3.1 at the right we show the unwrapped version of the phase trace, for central input 9, and a group of outputs (1,3,5,7,9,11,13 and 15), all of them referenced to the central AWG waveguide (i.e. we set zero phase for it). Again, the positions for the 37-39 central waveguides are indicated by black circles. What it is observed is a phase response which is pretty close to what it would be expected in the ideal case: each trace shows a great level of linearity, while the slopes of them change in $2\pi/9$ steps as the output is changed in steps of two. Not in vain, this phase characteristics leads to a telecom-grade spectral response, shown in Fig. 2.3 at the top, with a MSLR of 40 dB and a dynamic range of about 60 dB. Not shown in the figure is the measured trace with optical spectrum analyzer (OSA, see [67]), which shows an almost perfect agreement with the reconstructed spectral response.

Integrated AWGs in a SOI technology [70], designed in the context of a past PhD thesis of our group [66], were tested using OFDI to evaluate possible fabrication imperfections and discard design errors, given its non-ideal spectral response measured with OSA. The samples were manufactured through electron-beam lithography (EBL) and dry-etching, as described in [71]. As shown in the microscopy picture in Fig. 3.2 at the left, two AWG models are included: a conventional AWG consisting of $7 \times 7$ inputs and outputs with channel spacing of 1.6 nm an FSR = 22.4 nm, and the equivalent reflective AWG model based on Sagnac loop reflectors. Here, we show the OFDI characterization for the conventional AWG; more detail on the results and the reflective model can be found in [71].

Then, regarding the conventional AWG, its spectral response presents an asymmetric main lobe and quite low MSLR, as shown in Fig. 3.2 at the bottom, in solid curves with different colors corresponding to each output (and same central input) OFDI measurements were performed for all these cases. For each output case, the phase of the 19 central waveguides in the array are retrieved, and the incremental phase is computed, and shown in Fig. 3.2 at the top, upper plot. All of them coincide pretty well, sign of the technique reliability, except for waveguide 5. Very often, this does not concerns the DUT. It is probably a matter of the technique processing since, in some cases, under some specific processing parameters, the

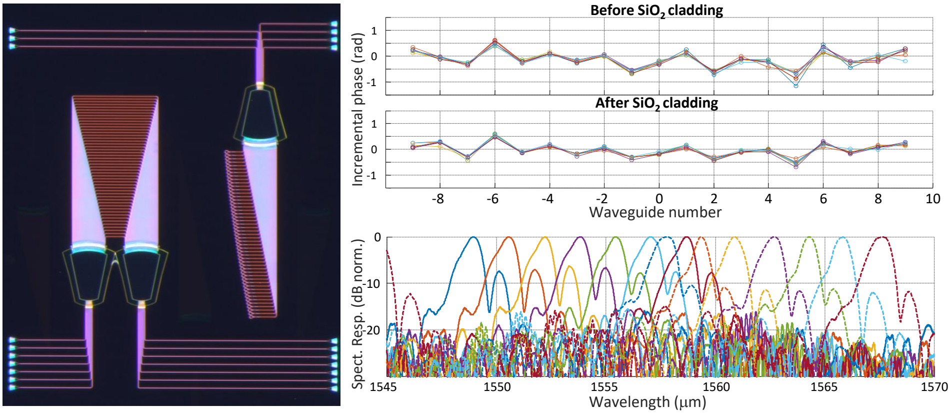

**Figure 3.2:** At the left, a microscopy picture of the fabricated AWGs. At the right, from top to bottom, the incremental phase traces of the central AWG waveguides after OFDI measurements, and the corresponding spectra, before and after SiO$_2$ cladding deposition, in solid and dashed curves, respectively.

evaluation of the temporal phase is trickier as the phase trace is more intricate than a perfect set of local maxima or minima, like in the case of the silica-based AWG. Indeed, it occurs for less ideal DUT tests where there is higher insertion loss (and thus, less dynamic range), more temporal contributions superposition, etc. In any case, strong deviations from linearity are observed for the AWG arrays, as the source of its non-ideal behaviour.

With the aim of reducing the sensibility of the array waveguides phase errors, a SiO$_2$ cladding was deposited onto the Si waveguides using plasma-enhanced chemical vapor deposition (PECVD), which reduces waveguides refractive index contrast and, ultimately, the channel crosstalk. The resulting spectrum is shown in Fig. 3.2 at the bottom, in dashed curves. An improvement of 5 dB is observed in the MSLR and also, as a side effect, a shift in the central wavelength of the device of about 9 nm. This improvement is corroborated with the phase assessment through the OFDI measurements shown in Fig. 3.2 at the top, the second plot. It is still observed the same incremental phase landscape, but the phase jumps are softer than in the previous case with no SiO$_2$ cladding, supporting the observed spectrum improvement.

Apart from these SOI AWGs, a different AWG model fabricated in an InP technology platform was similarly characterized with OFDI in the context of the mentioned PhD thesis.

The most direct utility of having the time domain response of a DUT at disposal is to identify (in its amplitude) the expected paths taking place in the DUT, and also to find out possible spurious events. A very good example of it is in the obtained time domain response for special Mach-Zehnder interferometer (MZI) designs, which were delimited by 2 × 2 MMI at the left and 3 × 3 MMI at the right,

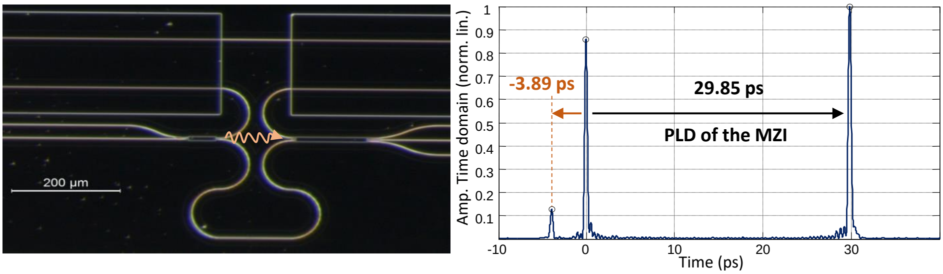

**Figure 3.3:** Microscopy picture of a MZI design with 2 × 2 and 3 × 3 MMIs delimiting it. At the right, the corresponding time domain response showing the two main peaks and a third smaller peak.

as shown in Fig. 3.3 at the left in a microscopy picture. These balanced MZIs are fabricated on a SiN platform and several of them with increasing path length difference (PLD) were measured, for wavelength sweep of $\Delta\lambda = 80$ nm around $\lambda_0 = 1550$ nm. In all the cases, when measuring any of the available outputs, two peaks are expected in the time domain separated the designed PLD. These are identified as the two strongest peaks in the time domain response shown for one of the cases in the figure at the right, separated the expected 29.85 ps. From this experimental time separation and the designed PLD, the average group index in the working band can be estimated by employing Eq. 2.19, obtaining $n_{g,0} = 1.785$.

The successful retrieving of the time domain response of the DUT with the presence of the two expected peaks is not the only result. In fact, the time domain response reveals the presence of a third peak, reduced in power when compared to the mains, and appearing in all the MZI cases exactly at the same temporal distance from the first peak, 3.89 ps before the shorter arm contribution. When inspecting the possible DUT paths giving rise to this, we realized that it corresponds exactly to the short straight separation between both MMIs (as highlighted in the microscopy picture), which is the same for all the designs and are in perfect alignment. This is a revealing evidence of an unexpected coupling between both MMIs, which means that a relevant part of the light literally transmits the first MMI and its coupling to the 3 × 3 MMI is facilitated by the unused central input waveguide.

## 3.2 Ring Resonators

In this section, we present an application to retrieve very valuable casuistry and some essential parameters about light propagation through the involved photonic blocks by employing RRs and OFDI measurement. In a first work [51], we retrieve group velocity dispersion (GVD) from an MMI-coupled RR in CNM SiN platform [1], intentionally designed for this purpose. Besides, thanks to the time domain picture, we are able to get information about the birefringence of the wave-

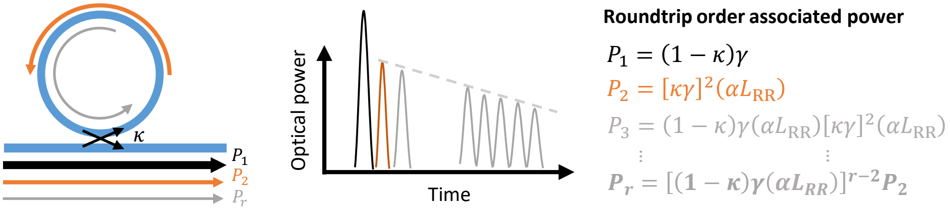

**Figure 3.4:** Sketch and power description of a conventional RR in the time domain.

guides. This same technique is employed in the same technology, different wafers, to characterize GVD and the results are included in [10]. Later on [52], we extend the technique over high-Q RRs, which are essential for frequency comb generation [72], optical clocks [73] and high-precision sensing [74] (in this last reference, an alternative method to retrieve GVD in high-Q RRs is shown). These samples are designed and fabricated in Chalmers university, MC2 SiN platform [75]. In this case, GVD is retrieved too, that is a critical design parameter as it influences the four-wave mixing efficiency in the formation of the combs, where anomalous dispersion is required to initiate the process. A reliable assessment of GVD from manufactured devices is crucial in this context so as to provide fully informed feedback to the design flow step. Besides, we utilize RR model fitting to obtain the RR coupling and roundtrip parameters as we show in what follows.

As it is shown schematically in Fig. 3.4, the most basic RR consists of a bus waveguide which guides light to a $2 \times 2$ optical coupler, characterized by coupling ratio $\kappa$. A part of a light pulse would go on throughout the bus waveguide and the other part is coupled to the RR cavity, where the light travels its body until reaching the optical coupler through the other input. Again, part of the light exits the cavity, while the other part keeps on recirculation (discarding light attenuation in the optical coupler given by its intrinsic loss $\gamma$, as modeled by Eq. 2.6). This makes the time domain picture of a RR to be formed by a train of decaying energy contributions separated the length of the cavity $L_{\mathrm{RR}}$, signature the consecutive recirculations of light along the RR. Depending on the coupling condition given by $\kappa$, there will be more or less visible contributions. In a strong coupling scenario, a great amount of light power is firstly coupled to the RR and in turn, in each subsequent passing through the coupler more power is expelled too, resulting into a fastly decaying group of peaks. When having a weak coupling, that is the case of high-Q RRs, the smaller amount of initial power coupled to the cavity is more evenly shared between the different roundtrip order contributions, which makes an enlarged and more even distribution of peaks to be expected, as long as their power is over the noise floor. This relation ultimately determine the number of peaks that are visible in the time domain well over the noise floor, and in the available temporal window.

When light makes a RR roundtrip, experiences waveguide attenuation and chromatic dispersion. Furthermore, it hits the coupler experiencing more attenuation (governed by $\kappa$ and $\gamma$). In a spectral picture, the RR regime can be classified by the criticial coupling, that takes place when rountrip propagation loss equals the coupler loss (for further description of a RR in this picture, see [76, 77]). Beyond, polarization-related phenomena may take place too: keeping to the single-mode regime of the waveguides, in the accumulated bend sections of the RR, polarization rotation between the two fundamental TE and TM modes can happen. If birefringence is non-zero, temporal peaks for TE and TM will be separated. In case of zero birefringence, this phenomena can be explored by the use of TE/TM filter combination at the input and output of the chip.

Taking into account all this rich casuistry, the time domain response of the RR can be exploited to extract valuable information. There are multiple contributions which are related to each other by a number of roundtrips and thus, propagation and optical coupler features. This makes the RR a suitable structure to do statistics with the retrievable parameters. On the one hand, from the peaks separation, we can obtain the average group index $n_{\mathrm{g},0}$ of the RR cavity waveguides by applying $n_{\mathrm{g},0} = cL_{\mathrm{RR}}/\Delta t$, as mentioned in section 2.3.2. Besides, there is a relation between energies carried by the contributions that can be used to fit the known response from theoretical models [78], governed by the coupler parameters $\kappa$ and $\gamma$, as well as the waveguide propagation loss $\alpha$ of the RR. The equations in Fig. 3.4 at the right, standing for the accumulated loss in the different light pathways, can be related. The first-to-second peak relation ($A = \frac{P_2}{P_1}$) and the slope of the decaying of the peaks ($B$) can be calculated and provide the following equations:

$$A = \frac{\kappa^2 \gamma \left(\alpha L_{\mathrm{RR}}\right)}{1-\kappa};\ B = (1-\kappa)\,\gamma\left(\alpha L_{\mathrm{RR}}\right). \tag{3.1}$$

These two equations can be related to get $\kappa$ and the roundtrip loss $\alpha_{\mathrm{RR}} = \gamma\alpha L_{\mathrm{RR}}$ (with $1-\kappa$ de-embedded), as:

$$\kappa = \frac{A-\sqrt{AB}}{A-B};\ \alpha_{\mathrm{RR}} = \frac{B}{1-\kappa}. \tag{3.2}$$

Finally and very interestingly, there is also phase information, that allows to ultimately retrieve the dispersion of the RR waveguides. Instead of computing phase measurements in the time domain, each peak corresponding to RR roundtrip order $r$ can be isolated, apply a crop window to it, and transform it individually to the frequency domain by FFT. In each individual peak spectral reconstruction, the frequency-resolved phase information $\phi_r(\omega)$ gives as a mean to obtain the group delay (GD, also expressed as $\tau_{\mathrm{g}}$), by doing the derivative of $\phi(\omega)$ with respect to the angular frequency $\omega$ along the measured range, according to Eq. 2.4). So after this step, we have a set of GD traces $\tau_{\mathrm{g},r}(\omega)$. A linear fitting can be applied to this traces in order to obtain dispersion information. Although in this way, as we shall see for the simple RRs in CNM technology, there is a contribution to the measured phase coming from the setup and any waveguide towards light has propagated. If, instead, relations between pairs of them are made, separated $M$ roundtrips, GVD or more specifically, the dispersion parameter $D$ (see relation between them in Eq. 2.3), can be extracted de-embedding any phase contribution

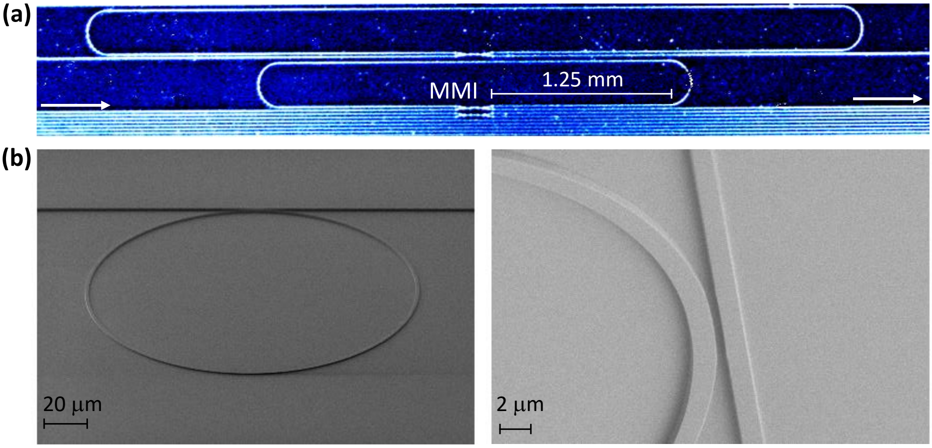

**Figure 3.5:** (a) RR in CNM (b) RR in Chalmers technology

but the RR roundtrip, as:

$$D \simeq \frac{\tau_{\mathrm{g},r+M} - \tau_{\mathrm{g},r}}{M L_{\mathrm{RR}}}, \tag{3.3}$$

where the length of the roundtrip length $L_{\mathrm{RR}}$ is used. If the group is sufficiently large, the relations can be made between further orders (greater $M$) of RR recirculations and therefore, more accumulated dispersion leading to more reliable estimations of $D$. These independent combinations (by pairs) result into different measurements of the accumulated phase for the given length increment, due to the presence of dispersion on the waveguides. It allows to eliminate the possible instabilities on the measurement setup, leading to a self-calibrated strategy to extract the GVD of the waveguide forming the RR.

### 3.2.1 Simple RRs in Silicon Nitride

The devices were fabricated in CNM SiN technology platform [1], on a 100 mm Si wafer, composed of a $SiO_2$ buffer (2.5 µm thick, $n = 1.464$) grown by thermal, following a low pressure chemical vapor deposition (LPCVD) $Si_3N_4$ layer with 300 nm thickness ($n = 2.01$) and a 2.0 µm thick $SiO_2$ ($n = 1.45$) deposited by PECVD. The routing waveguides have a width 1.0 µm. A set of RR were designed to be tested, as shown in Fig. 3.5(a). The bend radius was set to $R = 150$ µm for which no significant additional loss is expected. The length of the measured RR cavity (the one shown with white arrows) is $L_{\mathrm{RR}} = 6.63$ mm, while the bus straight waveguide from facet to facet has a length of $L_{\mathrm{SW}} = 11$ mm.

For this work, we employed a more sofisticated version of the OFDI setup [64], as reviewed in section 2.5: the time responses of the DUT in this configuration can be isolated after an FFT of the interferograms and provide the complete Jones Matrix description of the DUT on the polarization beam splitter (PBS) base. This polarization diversity setup is envisaged to avoid the environmental and

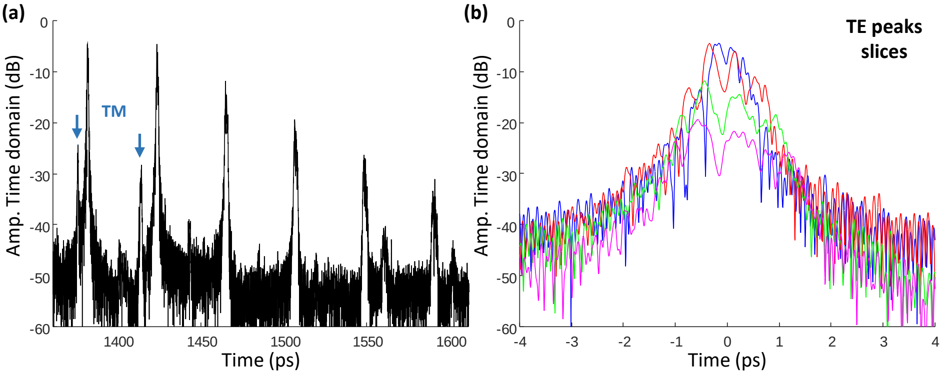

**Figure 3.6:** (a) CNM RR time domain (b) Peak slices, dispersion broadening effect onto multiple recirculations.

manipulation polarization changes on optical fiber pigtails and the rest of OFDI elements. However, we did not make use of all the potential of this measurements in this work. We just avoided to deal with polarization in this case, by collapsing all the time domain responses into one as a the sum of their modules For the measurements, we set a TL sweep of $\Delta\lambda = 100$ nm centered at $\lambda_0 = 1555$ nm, and a scanning TL speed of $v_{\mathrm{TL}} = 40$ nm/s.

After all the processing, the (amplitude) time domain response of the RR is shown in Fig. 3.6(a), where the multiple time recirculating contributions from the RR can be easily identified. As expected, the train of pulses (6 of them are well visible) show a $\simeq 3$ dB per contribution decaying energy slope, from the first to the last, as expected for an optical coupler of $\kappa \simeq 0.5$ (50:50 MMI). Not only that, but also the fundamental TE and TM modes splitting in time is observed revealing strong differences in propagation losses and GD between polarizations. Taking into account the designed length of the cavity, the group index can be estimated for each mode, resulting into $n_{\mathrm{g},0}^{\mathrm{TE}} = 1.892$ and $n_{\mathrm{g},0}^{\mathrm{TM}} = 1.717$.

Moreover, the amplitude time domain response of the RR shows also a clearly visible broadening effect due to chromatic dispersion: each contribution order shows an increasingly broader profile due to the accumulated dispersion along the ring cavity. As mentioned before, GVD or $D$ parameter can be extracted from the retrieved signals. So we proceed by selecting the desired TE pulses (recirculations) and slicing the corresponding time responses (in our case, both $h_s(t)$ and $h_p(t)$ separately) around ±4 ps from its center. We truncate each peak and show them all together in Fig. 3.6(b), where it is noted more clearly this progressive broadening. After this, each truncated response is transformed into frequency domain picture by FFT, where the phase information allows to get each $r$ contribution group delay $\tau_{\mathrm{g},r}(\omega)$, with $r = 0, 1, 2, \ldots$. Once these $\tau_{\mathrm{g},k}$ traces are obtained, they are fitted in the $\lambda = [1514, 1594]$ nm region to obtain the dispersion parameter $D$ (in ps/(nm m) units), as shown in Fig. 3.7(a). Each trace has a different absolute $\tau_{\mathrm{g}}$ that is unified for better representation. If we perform the calculation of $D$

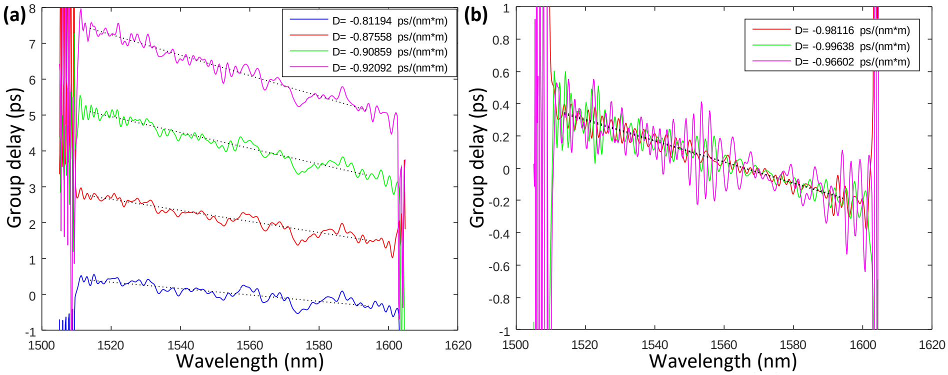

**Figure 3.7:** (a) GD curve and GVD measured for each temporal pulse, (b) GVD difference between pulses.

parameter in each case, by taking the corresponding physical lengths $L_{\mathrm{SW}}+rL_{\mathrm{RR}}$, the obtained $D$ values (included in the figure) are not constant. In fact, $D$ grows almost linearly with the cavity roundtrip order. This result suggests that a positive value of dispersion is being added to the one coming from the chip itself, and are likely originated at the measurement setup. Fortunately, at the core of the technique is that RR multiple recirculations can be related between them to isolate a single roundtrip pass along the ring cavity, and do some statistics with these values. By doing so, in Fig. 3.7(b) it is shown the GD difference between adjacent time samples $\Delta\tau_{\mathrm{g},r,r+1}$, including their linear fitting and the estimated dispersion calculated over $L_{\mathrm{RR}}$. These obtained values no longer show the previous growing behaviour, leading to an average dispersion of $D = -0.981$ ps/(nm mm) with ±1.5 % of relative error. From these value, it is straightforward to obtain the dispersion offset from the setup to be $DL_{\mathrm{setup}} = 0.00178$ ps/nm.

The described technique in this section was also applied in the context of the optical characterization of the same SiN technology platform [1]; the results are included in a co-authored publication [10] and are also a part of a past PhD thesis of our group [11]. The employed RR designs are the same, and the measurements are performed onto different wafer chips, under similar OFDI conditions. Again, the TE and TM modes are temporally separated and perfectly observable, forming two different RR temporal sets. Indeed, in the time domain shown in an included figure in [10], TM contributions are more present, permitting to notice that the second TM peak is stronger than the first, which is an evidence of RR roundtrip polarization rotation. If the experiment is set to filter TE and TM mode excitation at the input and output of the chip (as described in section 2.5), and for more peaks resolved, there is the opportunity to resolve several TE-TM rotations an thus, infer the strength and periodicity (per bend section) of this phenomenon. We had the opportunity to experimentally observe this in a private research project [69].

The TE and TM group indexes are, in this case, found to be $n_{\mathrm{g},0}^{\mathrm{TE}} = 1.892$ and $n_{\mathrm{g},0}^{\mathrm{TM}} = 1.717$, while a birefringence is determined to be $B = \left|n_{\mathrm{g},0}^{\mathrm{TE}} - n_{\mathrm{g},0}^{\mathrm{TM}}\right| = 0.168$.

The same procedure results into a waveguide anomalous dispersion $D = -1.43$ ps/(nm mm) with a relative error of ±1.5%, that is in agreement with the obtained value with the numerical model. Besides, the dispersion offset from the setup in this case is $DL_{\text{setup}} = 0.0014467$ ps/nm. We use this experimental value $D$ for this SiN technology waveguides in some parts of this thesis, e.g. to show theoretical and numerical dispersion effects onto the spatial resolution in sections 2.4, 3.3.2 and 4.1.

### 3.2.2 High-Q RRs in Silicon-rich Nitride

In comparison to the simple RR in previous subsection, in this case we find that the time domain response consists of a very long train of pulses or time contributions with significantly lower power, due to the much lower coupling regime. Besides, the GVD differences between adjacent time contributions are expected to be smaller, since shorter RRs with low dispersion waveguides are designed. However, the group of peaks is sufficiently resolved over the noise floor in the time domain and, the fact it is a numerous group, allows to estimate GVD reliably, as we show below.

Regarding the samples, two different RRs with circular shape of radius $R = 80$ µm where designed and fabricated in silicon-rich nitride Chalmers University MC2 laboratories [75]. The RRs are coupled to the bus straight waveguide by the evanescent field of the ring/straight waveguides. The two samples differ on the gap between the straight bus waveguide and the RR, so we refer to them as gap 1 (467 nm) and gap 2 (517 nm). The designed height and width of RR waveguides are 645 nm and 1650 nm respectively, targeting for anomalous dispersion in optical telecommunication C-band for the TE mode. However, the waveguide width in the RRs after fabrication was 1570 nm due to some dimension loss. The height and width of the bus straight waveguides are 645 nm and 1000 nm. As for the fabrication process, it was very similar to previous work in [79], but using $SiH_2Cl_2$: $NH_3$ = 3.9 instead. Scanning Electron Microscope (SEM) images of one of the fabricated samples, prior to cladding deposition, are shown in Fig. 3.5(b).

For the measurements, the TL is set to sweep $\Delta\lambda = 80$ nm centered at $\lambda_0 = 1550$ nm, with a scanning speed of $v_{\text{TL}} = 20$ nm/s. In order to control polarization mode excitation on the chip waveguides, the linear polarizer ($\text{LP}_{\text{in}}$) between a fiber collimator and an objective approach shown in Fig. 2.6(a) is employed, which ensures TE/TM mode excitation, and of course together with the fiber polarization controller (P1 in Fig. 2.1). The same polarization control stage is utilized at the output of the chip (linear polarizer $\text{LP}_{\text{out}}$). Furthermore, it is employed a PBS at the DUT-MZI output to circumvent the unwanted polarization instabilities in the fiber setup, that cause signal fading as explained in 2.5 of this thesis. The OFDI measurements were performed for different combinations of the $\text{LP}_{\text{in}}$ and $\text{LP}_{\text{out}}$ polarizers. Among them, the best resolvable impulse response was observed for TM/TM combination (input excitation/output filtration). This is in agreement with simulations, where the TE mode is not coupled to the ring, after the dimensional loss from fabrication and thus optical coupler and waveguide change. Hence, for TM/TM, we performed measurements corresponding to the

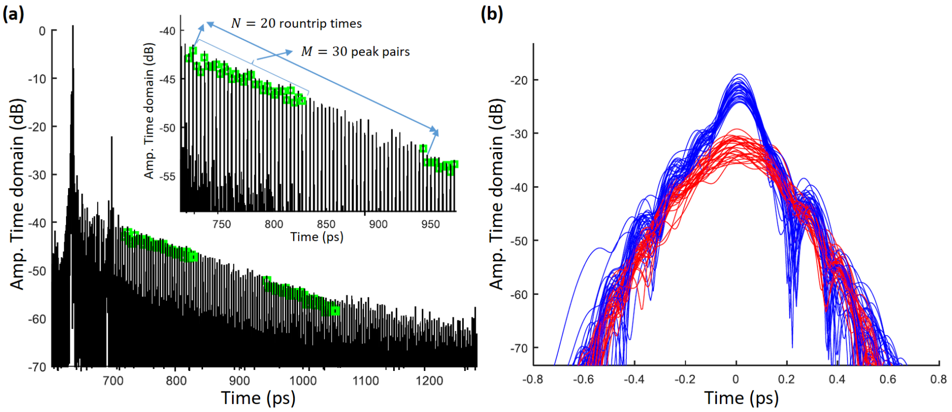

**Figure 3.8:** (a) Time domain response of gap 1 RR, where multiple round-trip contributions can be seen. Labelled in green, pulses that are selected to be truncated are filtered and shown together in (b), the first set in blue and the second one in red.

aforementioned gap 1 and gap 2 RRs.

After all the OFDI processing, in Fig. 3.8(a) the obtained time domain response for gap 1 RR is shown, exhibiting a large number of recirculation pulses well defined over the noise floor. The direct contribution from the straight bus waveguide (the highest) is also visible. Furthermore, the peak corresponding to the facet to facet chip Fabry-Perot (the second highest) can be observed as well. From the time difference between the pulses $\Delta t = 3.74$ ps and the known RR roundtrip length $L_{\mathrm{RR}} = 2\pi R$, the average group index for the TM mode of the RR waveguides is $n_{\mathrm{g}}^{\mathrm{TM}} = 2.23$. In green, a first set of $M = 30$ consecutive pulses (order $22 - 51$) are isolated to be compared later on with pulses separated $N = 60$ roundtrip times (pulses $82 - 111$ in the sequence).

The isolated pulses are then truncated over a given time range. They are all shown together in Fig. 3.8(b), the first set in blue and the second one in red, where the slight degradation due to the accumulated dispersion can be noticed. When truncating single roundtrip contributions, there is a trade-off between artificial GD distortion and the effect of the noise floor: a Gaussian window is applied to reduce the noise, but an excessive time truncation leads to artificial distortion of the GD curve resulting from the FFT, thus introducing errors in the estimation of the GVD. A compromise value of 0.8 ps of Gaussian window width is chosen for this processing step. After performing the FFT to the selected set of pulses, their corresponding GD is obtained by doing the derivative of the optical phase with respect to the angular frequency $\omega$ along the measured $\omega$ range. Then, the GD traces of the pulses are subtracted to obtain the differential GD, and from it the GVD is derived through a linear fitting procedure. The differential GD between the selected pairs of pulses $\Delta\tau_{\mathrm{g},k,k+1}$ is computed one to one ($N = 60$ accumulated roundtrips) for the GVD calculation, and produces the expected linear trend, but

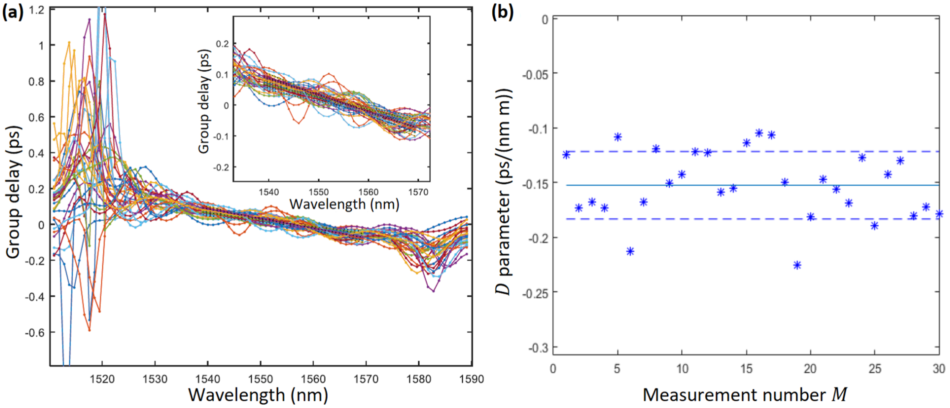

**Figure 3.9:** Differential GD (a) for the selected pulse-pairs for gap 1 measurements. In the inset, a zoom of the chosen fitting range for the GVD estimation is shown, with the results plotted in (b), where the average $D$ and the corresponding $\pm\sigma$ (standard deviation) are traced in continuous and dashed lines, respectively.

with oscillations due to the aforementioned causes, that influence the quality of to the linear fitting process, and gives some uncertainty in the resulting GVD value. In this case, we average the GVD obtained for the $M = 30$ pairs of pulses processed, in a chosen safe wavelength range of $\lambda = [1540, 1570]$ nm, as shown if Fig. 3.9(a). The availability of multiple pairs of pulses allows to do statistics and reduce the uncertainty by averaging the fitted GVD value as shown in Fig. 3.9(b), where the obtained average $D$ is also given along with the corresponding standard deviation $\sigma$.

The same procedure has been also applied to the analysis of gap 2 RRs. In this case, the plotted time domain response in Fig. 3.10(a) shows the recirculation peaks closer to noise floor in comparison to gap 1 samples, with a dynamic range about 10 dB lower. This is in agreement with a larger gap in the evanescent coupling region, corresponding to a weaker coupling. In this case, the second contribution from the facets reflections hampers in the selection of pulses to be processed for GVD estimation as described previously. For this gap 2 RRs, the first set of pulses starts just after the second facet reflection, with a lower separation $N = 30$ and a reduced number of pulse pairs $M = 20$ can be selected, since the noise floor prevents extending the time range further. Proceeding similarly as described for gap 1 RR, the set of differential GDs are shown in Fig. 3.10(b), and the resulting estimations for the GVD by linear fitting are given in Fig. 3.10(a) as well as an inset.

A summary of the results is provided in Table 3.1 for the GVD values and associated standard deviations $\sigma$. The differences for the three first GVD measurements of gap 1 RRs are in the order 0.008 ps/(nm m), corresponding to a relative $\approx 5\%$ error. The two available GVD measurements for gap 2 RRs show larger

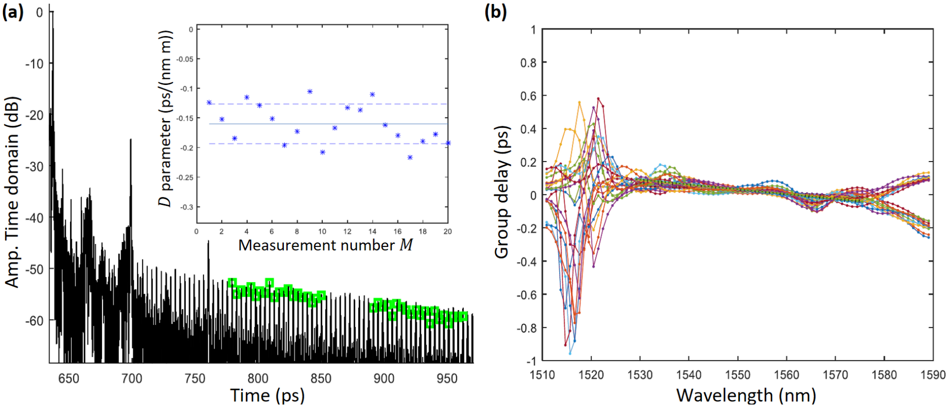

**Figure 3.10:** Time domain response (a) of gap 2 RR, where multiple round-trip contributions can be appreciated. Labelled in green, the selected set of pulses for GVD estimation. In the inset, different GVD estimations calculated by fitting differential GDs shown in (b).

difference. The fourth measurement for gap 1 has been performed for $N = 40$, giving a GVD estimation slightly away from the others. This result, along with the fact the estimations for gap 2 are around the values for gap 1 (as expected, since the waveguide cross-section within the ring is the same), suggests the higher reliability onto the measurements for the first device, which showed contributions further away from noise floor when still keeping to $N = 60$ (where accumulated dispersion is higher and then better resolved). Mode solver simulations (with COMSOL Multi-Physics software, see Fig. 3.11 in one of the insets) confirm the measurements, yielding an average value of $D = -0.137$ ps/(nm m) for the range where we have fitted the measurements and derived the GVD values ($\beta_2 \simeq 175$ ps$^2$/km for $\lambda = 1550$ nm). This in turn provides a good general agreement between the estimated GVD from measurements of this method and the numerical simulation.

Finally, we took advantage of the presence of the two spurious chip facet reflections in gap 2 measurements to estimate the $D$ parameter corresponding to the straight bus waveguide. The procedure is the same as above, but with only two pulse contributions, yielding a value of $D = -0.274$ ps/(nm m). This slightly different dispersion in the straight waveguide, compared to the waveguides forming the RR cavity is attributed to the different waveguide width, 1000 nm for the straight bus waveguide, and 1570 nm for the RR bend waveguide.

Fig. 3.11 shows the complete time domain response normalized in amplitude to the main pulse ($P_1$) that, as mentioned previously, corresponds to the direct bus straight waveguide contribution (from input to output of the chip). The normalization to this time contribution removes the total input/output coupling losses to the chip leading to a relative vertical axis (in dB scale). What it is left is only related to the cavity evanescent coupling $\kappa$ and $\gamma$, and the RR internal propaga-

**Table 3.1:** Different measurement results for $D$ parameter, for both gap 1 and gap 2 RRs

| Device | # Measurement | D [ps/(nm m)] | $\sigma$ [ps/(nm m)] |
|---|---|---|---|
| gap 1 | 1 | -0.145 | 0.051 |
| | 2 | -0.153 | 0.031 |
| | 3 | -0.150 | 0.045 |
| | 4 | -0.164 | 0.050 |
| gap 2 | 1 | -0.160 | 0.034 |
| | 2 | -0.137 | 0.027 |

tion losses $\alpha L_{\mathrm{RR}}$. In Fig. 3.4, it is a schematic description and the formulae for the power contributions corresponding to sequential pulses in the RR. In order to properly extract these parameters we start from the raw OFDI temporal trace depicted in Fig. 3.11. Observe that the pulse amplitude distribution deviates from the expected linear decay given by complete RR roundtrip $B = (1-\kappa)\,\gamma\,(\alpha L_{\mathrm{RR}})$. The discrepancy is due to the pulse distortion effects of the GVD (pulse temporal broadening) over multiple time spans. Notice that the measurements are made along a $\Delta\lambda = 80$ nm range leading to input equivalent time pulses of $\sim 0.1$ ps (see Fig. 3.8 (b)) which are sensitive even to low GVD. To remove this effect, we integrated the total energy contained around the time center of each pulse, in a time interval of $\sim 1-2$ ps, so that the effect of dispersion is compensated and only the linear decay due to loss (coupling and propagation losses) is left. In Fig. 3.11 at the bottom, the measured peak powers (green squares) are shown together with the corrected points after the energy integration (red dots). After this, the RR amplitude in time domain is fitted to the theoretical model. First, we find the second contribution in time (marked in Fig. 3.11 at the bottom as $P_2$) to be related to the main $P_1$ (0 dB in our normalized scale) to get $A$ in Eq. 3.1. Then, a linear fitting is performed (shown as dotted red line) for the corrected set of time contributions, along the available temporal range, and for those free from spurious and well over the noise floor. Reflections on facets were localized and excluded properly. By applying Eq. 3.2, for the shown device (gap 1) it is obtained $\kappa = 0.011$ and $\gamma L_{\mathrm{RR}} = 0.987$. Additionally, the processing of the approximately $\sim 130$ pulses yield an average roundtrip elapsed time of 3.74 ps. In Fig. 3.11 inset, the simulated spectral response of the RR is shown, employing the analytical expression for the RR [78] and the estimated values as discussed. It is observed a FSR of 267.7 GHz ($\sim 2.2$ nm) and 8.2 pm of -3 dB notch bandwidth that agree with the acquired spectral traces.

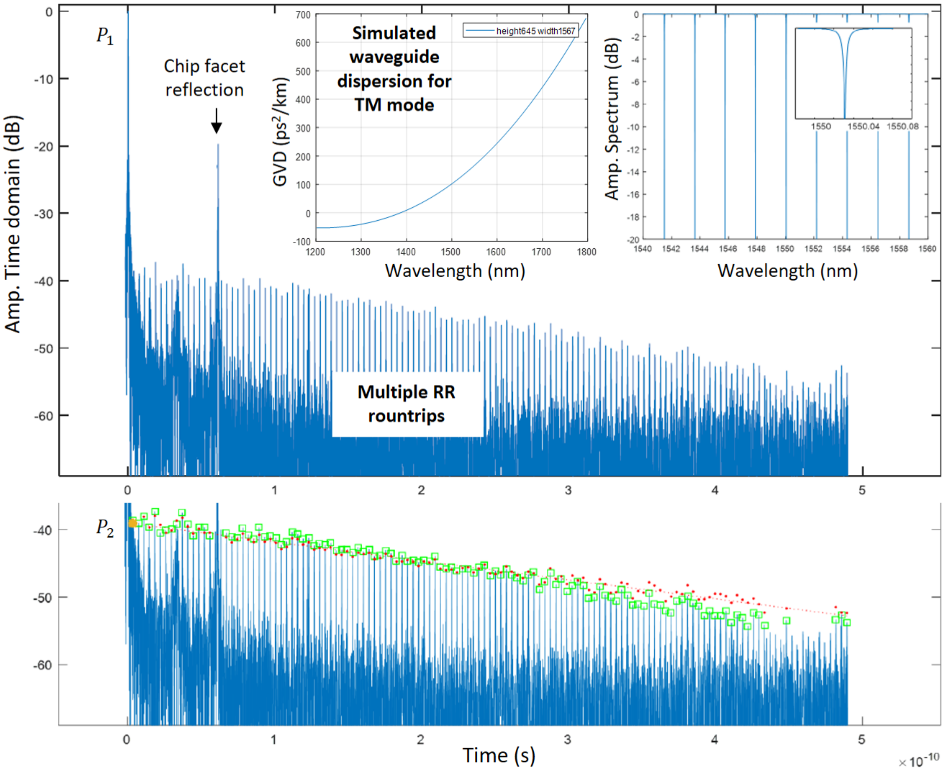

**Figure 3.11:** Time response measured for the gap 1 RR superimposed to the fitted analytical model. The right inset shows a zoomed over a range for some pulse contributions, for both the measurement and the analytical model as well. The left inset provides the reconstruction of the spectral response -with sharp notches- provided by the analytical model.

## 3.3 Waveguide Propagation Loss and Optical Coupler characterization

In this section, techniques using OFDI to characterize waveguide propagation loss are covered. First, we review a proposed technique that makes use of the reflectometry mode to measured backscattered light in integrated waveguides [41], allowing to obtain propagation loss, and that we have employed in several cases with our OFDI setup (some results are included in [10]). In the subsection following it, relying on OFDI measurements we propose a test device that allows to characterize both propagation loss and power splitting ratio of optical couplers [53].

### 3.3.1 Waveguide Propagation Loss by Reflectometry

The major part of the OFDI applications developed in this thesis are set in transmission mode. Here we show an application where it is indispensable to do OFDR as such, i.e. actual reflectometry. At a setup level, as explained in chapter 2, this mode can be adopted easily from the typical MZI-based setup by employing an optical fiber circulator.

Light propagation through the integrated waveguides experiences, among other phenomena, severe attenuation in comparison to optical fiber. Two physical mechanisms gives to rise to attenuation [80,81], and material absorption is one of them. However, and by far, the most significant mechanism is by scattering on the high sidewall roughness present on integrated waveguides due to the fabrication process. The propagating optical mode, that can be more or less confined in the waveguide, notes this roughness as a continuum optical interface, suffering from continuous Fresnel reflections and thus, attenuation. Part of this reflected light is radiated outside the waveguide, but there is another part of it that reflects in perfect ‘zero’ angle and therefore, couples to waveguide and propagates backwards. Let us consider a light signal propagating through a straight waveguide, such that the field at $x$ is $a(x) = a_0 e^{-\alpha x/2} e^{-i\beta x}$, where $\alpha$ is the (linear) propagation loss of the waveguide, $\beta$ its propagation constant, and $a_0$ the input field amplitude. At each point $x$, a portion of light $ra(x)$ reflects and propagates backwards, where $r$ is the reflectivity. This amount of light, back to input 0 is:

$$\begin{aligned} a_{\mathrm{R}}(x,0) &= (ra(x))\, e^{-\alpha x/2} e^{i\beta x} \\ &= r a_0 e^{-\alpha x}. \end{aligned} \tag{3.4}$$

Therefore, at the reflected field resolved spatially, we expect $a_{\mathrm{R}}(x,0)$, which is function of $\alpha$. If we transform this to the logarithmic scale, by computing $10\log()$ operation, we get:

$$a_{\mathrm{R,dB}}(x,0) = 10\log(ra_0) - \alpha_{\mathrm{dB}} x \tag{3.5}$$

where we have used the propagation loss in dB/cm given by Eq. 2.2. This is, the reflected field in the amplitude time/spatial domain, in dB scale, is expected to be a linearly decaying ramp with slope $\alpha_{\mathrm{dB}}$ (independently of the input field

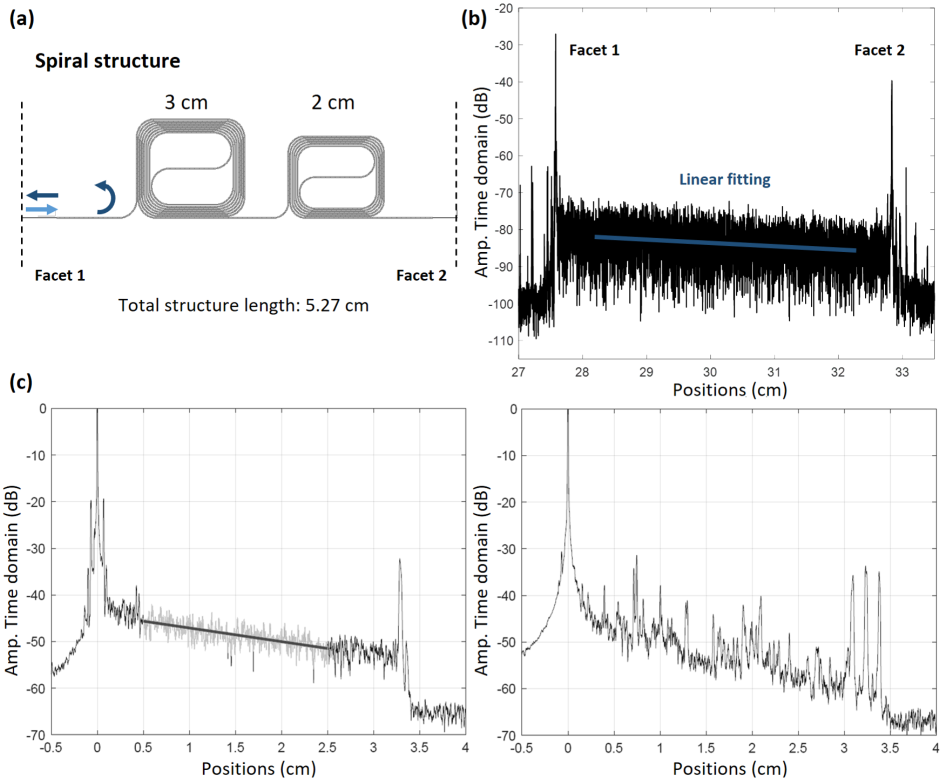

**Figure 3.12:** (a) Spiral design for OFDI reflectometry propagation loss retrieving. (b) Amplitude time domain response of the reflectometric measurements on a SiN platform, showing the expected decaying ramp. (c) Two other ramp traces obtained for a different SiN platform, where averaging is performed and spurious reflections are observed for one of the cases.

amplitude or the waveguide reflectivity). Besides, the initial field amplitude $a_0$ and the reflectivity of the waveguide $r$ determine the initial point of the ramp.

As demonstrated in [41], a reflectometric OFDI measurement provides this curve and thus, a way to obtain the waveguide propagation loss by linear fitting of the time domain response data (alternative ways to retrieve propagation loss with interferometry are in the literature, e.g. [82]). We have applied this technique in several experiments, for waveguides in different technologies. Leaving aside the results as such, we show and comment on some details about the technique for some measurements performed in two different SiN technology platforms. The employed test structure as a DUT for this experiment is quite simple: a waveguide spiral implementing a considerably large delay line. The employed design picture is shown in Fig. 3.12(a), where a delay line of more than 5 cm is implemented through two spirals of 3 and 2 cm, respectively, plus the routing waveguide sections.

After OFDI processing is applied to the measurements, the resulting decaying ramp corresponding to the backscattered light is shown in 3.12(b) for waveguides fabricated in a SiN platform in a private research project [69]. In principle, the ramp fashion looks pretty linear decaying in the dB scale, as expected. Besides, no spurious contributions are found along it, although pretty large amplitude noise is present, something that makes more difficult the linear fitting. The two high peaks delimiting the ramp stretch correspond to reflections onto input and output facets of the chip.

In a previous work, the same type of measurements with almost the same test structure (2 and 1 cm spirals instead) were performed in the context of a SiN platform [1] characterization, whose the results are included in [10,11]. In Fig. 3.12(c) again, as in (b), the decaying ramp is observed over the noise floor. However, in any of the cases the ramp curve is too far from it. In our practical experience, it is tricky to obtain this temporal structure sufficiently over the noise floor since $r$ is typically small. Besides, once it is achieved, it is still pretty much present noise on it. A straightforward strategy to reduce noise is by averaging over several measurement takes. The result of doing this is a cleaner ramp as the one shown in Fig. 3.12(c) at the left. This operation, apart from leaving a better look curve more ready to be fitted, it also reveals the possible waveguide local imperfections too, which are those contributions not disappearing with averaging and that are intrinsic to the device. The presence of them can entail a serious problem for the linear fitting, and in specially strong imperfections cases as the one shown in Fig. 3.12(c) at the right, even making it an impossible task. The two cases in Fig. 3.12(c) correspond to different wafers: at the left, an additional oxidation process after waveguide etching helps in reducing damage on the waveguide sidewalls.

Summarizing, the technique can be suitable to obtain an estimation of the propagation losses, and also to have a landscape of the possible waveguide imperfections manifested into peaks in the reflectometric temporal ramp. However, in our experience, the technique is not the most robust. It is difficult to get the ramp traces over the noise floor and averaging to reduce the present noise is more than recommended. The possible waveguide local reflection peaks disturb the linear fitting too. But even when these are not present, there is some degree of arbitrariness in the estimation, since the obtained values for $\alpha_{\mathrm{dB}}$ from linear fitting vary considerably when changing the starting and final points of the linear fitting. Besides, the shorter the DUT is, the more ambiguity in the linear fitting. Therefore, in the direction of optimizing this estimation, i.e. maximize curve smoothing and reduce the possibility of undesired spurious peaks:

- Employ large delay lines, implemented by spirals.
- Use large radius bends in the spiral structures, or even adiabatic bends to discard a possible waveguide reflection source.
- Average over multiple measurement takes to reduce noise amplitude in the curve.

In a conventional OFDI measurement, a given bandwidth $\Delta\lambda$ is swept. Therefore, estimated $\alpha_{\mathrm{dB}}$ corresponds to an average for that band. If wavelength resolution is desired for $\alpha_{\mathrm{dB}}$, piecewise OFDI measurements explained at the end of section 2.3.2, may be performed. In what follows, we propose an alternative method to retrieve propagation loss with OFDI (and other parameters); in this case, by adopting a transmission mode.

### 3.3.2 Power Splitter Test Device

The direct characterization of more than one input and/or output device is subject to the uncertainty of optical power coupling efficiency, which typically varies from one channel to other due to chip fabrication errors and varying measurement conditions. This is the case for $2 \times 2$ and $1 \times 2$ optical couplers or power splitters (PS), of ubiquitous use in any PIC and commonly implemented by MMI and directional couplers. A straightforward strategy to approach this issue comprises the using of a cascade of the same devices having multiple outputs to be measured and fit the outcome data to a linear function [83], implying a sequence of measurements, the more the better for an accurate mean value. This same task might be overcome with a single OFDI reflectometry measurement of this cascade test structure, by introducing an slight PLD between the different paths, and taking advantage of the chip–air Fresnel reflections. In the time domain, the peaks energy can be related between them to get the coupler parameters, getting rid of the different output measurement uncertainty in the off-chip coupling positioning. In any case, this approach is unable to decouple the coupling ratio $\kappa$ from the excess loss $\gamma$ of the device. Not in vain, this is device is temporally like

Here, we present an OFDI application that exploits the strength of the time domain response of the DUT to evaluate the power splitting ratio of the optical couplers, and also the integrated waveguide propagation losses, wavelength-resolved in a fast single or double measurement scheme. This application is enabled by the use of two integrated power splitter test device (PSTD) versions, that we explain in what follows along with their application range, the corresponding numerical validation, and discussion on the physical implementations.

As argued along this thesis, the time domain response of a DUT is composed of the different events taking place on it. Provided that they are spatially separated, they can be isolated and their contained information (position, power, optical phase) can be related. Apart from localizing and identify unexpected events, this feature is demonstrated to be extremely useful to relate optical phase and positions to characterize performance or derive propagation parameters (e.g. with RRs in previous section 3.2). Here we exploit the optical power relation of the temporal peaks, by intentionally proposing a test structure, to characterize the optical coupler performance (coupling ratio $\kappa$) and the integrated waveguide propagation loss $\alpha$.

The main version of the PSTD (that we call 2-PSTD) is shown in Fig. 3.13 at the left, and comprises a serial combination of two MZIs and three optical couplers (MMIs). There is one path in each MZI having a length $l_0$, being $l_1$ and $l_2$ the lengths of the other arms in the first and second MZIs, respectively, fulfilling

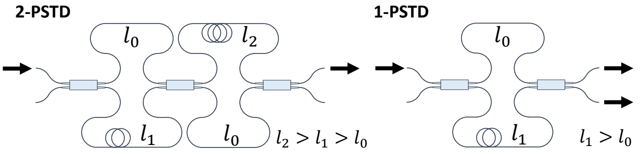

| | 1-PSTD | | 2-PSTD | |
|---|---|---|---|---|
| | 2 × 2 | 1 × 2 | 2 × 2 | 1 × 2 |
| Supported | Yes | Yes | Yes | No |
| IW losses | Yes | No | Yes | - |
| Num. takes | 2 | 1 | 1 | - |

**Figure 3.13:** Sketch the proposed PSTD test structures, including a summary table of their applicability.

$l_2 > l_2 > l_0$. The time domain transfer function of this structure is composed of 4 contributions corresponding to the 4 possible paths: the shortest one going through the shorter MZI arms (length $2l_0$), the next going through the arms below $(l_0 + l_1)$, and so forth for the remaining 2 combinations, corresponding to lengths $l_0 + l_2$ and the longest, $l_1 + l_2$. In this way, each followed path hits the three optical couplers the same times, but in a different combination of bar/cross states and integrated waveguide lengths. The optical coupler under test, a 2 × 2 type in this case, have bar (0-to-0 and 1-to-1 channels) and cross (1-to-0 and 0-to-1) connections, and it can be modeled by the matrix $\hat{M}$ in Eq. 2.6, where $\gamma$ stands for the excess loss of the coupler and $\kappa$ determines its power ratio. On the other hand, in order to model the light propagation we employ propagation matrix $\hat{P}_{a,b}$ as given in Eq. 2.7, describing the propagation regions in the MZIs for integrated waveguide lengths $l_a$ and $l_b$ (being $a, b = 1, 2$ and 3), where the propagation is governed by $\beta$, and the propagation loss is given by $\alpha$. The transfer function of the 2-PSTD is computed by concatenating these matrices as:

$$\hat{H}_{\text{2-PSTD}} = \hat{M}\hat{P}_{2,0}\hat{M}\hat{P}_{0,1}\hat{M}. \tag{3.6}$$

By setting a normalized input field $F_0$ on the upper input of the 2-PSTD, i.e. $F_0 = \left(\begin{smallmatrix}1\\0\end{smallmatrix}\right)$, after some basic algebra the associated power coefficients $\Lambda_i$ for each temporal contribution $i = 1, 2, 3$ and 4 can be obtained:

$$\begin{aligned}
\Lambda_1 &\propto \kappa^2 (1-\kappa)\, e^{-2\alpha l_0}, \\
\Lambda_2 &\propto \kappa^2 (1-\kappa)\, e^{-\alpha(l_0+l_1)}, \\
\Lambda_3 &\propto (1-\kappa)^3\, e^{-\alpha(l_0+l_2)}, \\
\Lambda_4 &\propto \kappa^2 (1-\kappa)\, e^{-\alpha(l_1+l_2)}.
\end{aligned} \tag{3.7}$$

If besides, we choose $l_1 = l_0 + \delta l$ and $l_2 = l_0 + \delta l$, these contributions are separated exactly $\delta l$ in the time domain, such that:

$$\begin{aligned}
\Lambda_1 &\propto \kappa^2 (1-\kappa), \\
\Lambda_2 &\propto \kappa^2 (1-\kappa)\, e^{-\alpha(\delta l)}, \\
\Lambda_3 &\propto (1-\kappa)^3\, e^{-\alpha(2\delta l)}, \\
\Lambda_4 &\propto \kappa^2 (1-\kappa)\, e^{-\alpha(3\delta l)};
\end{aligned} \tag{3.8}$$

so that all of them are under the same proportionality conditions (the $\gamma$ and $e^{-2\alpha l_0}$ are common terms). By trivial relations between them, we have a mean to obtain $\kappa$ and $\alpha$,

$$\kappa = \frac{1}{1+\sqrt{\frac{\Lambda_2\Lambda_3}{\Lambda_1\Lambda_4}}}; \; \alpha_{\mathrm{dB}} = \frac{10}{3}\frac{\log\left(\Lambda_1/\Lambda_4\right)}{\delta l}, \tag{3.9}$$

where Eq. 2.2 has been applied. Therefore, in a single-measurement scheme, the 2-PSTD allows to characterize both MMI coupling ratio $\kappa$ and waveguide propagation loss $\alpha$. Besides, since this is achieved with an OFDI measurement (of span $\Delta\lambda$ and PLDs set to $\Delta l$ and $\Delta l'$), a piecewise processing can be applied to a sequence of portions of the whole band (as discussed in section 2.3.2), allowing to obtain the wavelength dependance of these magnitudes, $\kappa = \kappa(\lambda)$ and $\alpha = \alpha(\lambda)$, along $\Delta\lambda$. This is confirmed by numerical simulation: in Fig. 3.14(a), the time domain response of the 2-PSTD is shown, for which the chosen lengths are $l_0 = 2$ mm, $l_1 = 3$ mm and $l_2 = 4$ mm. This is obtained after a simulated OFDI measurement with wavelength sweep span $\Delta\lambda = 100$ nm centered at $\lambda_0 = 1550$ nm, and PLDs set to $\Delta l = 20$ cm and $\Delta l' = 80$ cm (describing the conventional fiber-based OFDI system that we employ along this thesis). Regarding the integrated waveguides, it is considered a second-order dispersion model for the $\beta$, as given by Eq. 2.2, with $n_{\mathrm{eff},0} = 1.57$, $n_{\mathrm{g},0} = 1.9$ and $D = -1430$ ps/(nm km), resembling the CNM SiN technology waveguides used in this thesis [1, 10]. Besides, a varying nonlinear propagation loss from 2.2 to 1.8 dB/cm along $\Delta\lambda$ is simulated, as shown in the black solid line in the corresponding inset. Similarly, the MMI power ratio has been chosen to vary in the range $\kappa = [0.4, 0.55]$. The processing of the resulting interferograms has been performed piecewise, as explained at the end of section 2.3.2, to have 10 evenly distributed data along $\Delta\lambda$, where the distance between the contributions is more than enough to keep them away from each other after the corresponding time domain broadening of the peaks in the sub-bands. To account for this temporal broadening and the induced by integrated waveguide dispersion, the coefficients $\Lambda_i$ are obtained by integrating each peak independently. The recovered $\kappa$ and $\alpha$ by employing Eq. 3.9 are plotted in blue points, in the corresponding insets above and below, respectively. These results show an almost perfect agreement with the simulated parameters. The estimation of $\alpha$ is observed to be a little more sensitive to the measurement conditions. Still, the method is verified to be robust against dispersion and different coupling conditions.

An alternative version to the 2-PSTD is also considered, and this is a simpler device formed by a single MZI and two optical couplers as shown in Fig. 3.13 at the middle (1-PSTD). Similarly as for 2-PSTD, the transfer function of this device is given by $\hat{H}_{\text{1-PSTD}} = \hat{M}\hat{P}_{0,1}\hat{M}$. However, as summarized in the applicability table in Fig. 3.13 at the right, the derived coefficients for each one of the outputs is not enough to get $\kappa$ and $\alpha$ as in the 2-PSTD. One of the measured outputs permits to obtain $\alpha$, and this needs to be used as input to obtain the optical coupler power ratio $\kappa$ with the other output measurement. By proceeding as for the 2-PSTD case, now two contributions are taking place in the time domain for each measurement, so that the associated power coefficients $\Lambda_{i,j}$ with $i = 1, 2$ (peaks) and $j = 0, 1$,

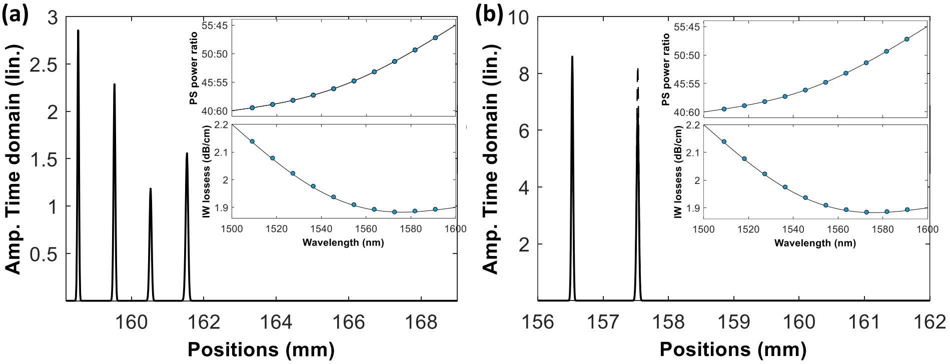

**Figure 3.14:** (a) Numerical simulation of the time domain response of the 2-PSTD. In the inset, the waveguide propagation loss and PS power ratio targeted (solid lines) are recovered by the technique (dots). (b) The same plots for 1-PSTD: in the main plot, the time domain responses corresponding to both outputs are shown (solid and dashed lines).

the output, are given by:

$$\begin{aligned} \Lambda_{1,0} &\propto (1-\kappa)^2, \\ \Lambda_{2,0} &\propto \kappa^2 e^{-\alpha(\delta l)}, \\ \Lambda_{1,1} &\propto \kappa(1-\kappa), \\ \Lambda_{2,1} &\propto \kappa(1-\kappa)\, e^{-\alpha(\delta l)}. \end{aligned} \tag{3.10}$$

The coefficients ratio corresponding to output 1 give a mean to get the propagation loss of the waveguides. This value, which is worth to remind that is free from measurement conditions variations, is then used to be related with the coefficients of output 0 to obtain $\kappa$, as it follows:

$$\kappa = \frac{1}{1+\sqrt{\frac{\Lambda_{1,0}\Lambda_{2,1}}{\Lambda_{1,1}\Lambda_{2,0}}}}; \ \alpha_{\mathrm{dB}} = 10\frac{\log\left(\Lambda_{1,1}/\Lambda_{2,1}\right)}{\delta l}. \tag{3.11}$$

The corresponding numerical simulation by employing 1-PSTD is shown in Fig. 3.14, using the same parameters as described above for the 2-PSTD. In this case, we have 2 contributions in the time domain response for each output: the two ones corresponding to the upper output 0 (solid line) and the ones for output 1 (dashed line). After processing under the same conditions as in 2-PSTD simulation, $\kappa$ and $\alpha$ are obtained, showing again a perfect agreement with the designed parameters.

The 1-PSTD test structure is also used for the same purpose in [84], where the method is based on an analysis of the spectral response instead. However, the fact the proposed technique is based on OFDI, enables the time domain response that paves the way to untangle the different contributions involved. Amongst the benefits, this allows to design a more complex structure as it is the case of the 2-PSTD, enabling a single-measurement characterization, and also makes the technique robust against the presence of chromatic dispersion by integrating the temporal peaks. Beyond, there is room to obtain estimations of other parameters such as the waveguide dispersion, by comparing peaks similarly as done in section 3.2.

In an implementation of the technique presented in this section, some attention must be paid to the setting of the PLDs of the MZIs. Apart from being sufficiently large for the corresponding temporal contributions to be separated enough to be resolved individually (taking into account spatial resolution $\delta z$ of the measurement, through $\Delta\lambda$ and waveguide dispersion $D$ as given by Eq. 2.20), it is recommended to set a larger $\delta l$ to resolve the waveguide propagation loss. If, for example, the expected waveguide loss is around 1 dB/cm, at least $\delta l \simeq 1$ cm should be considered in the design of the test structure. It is observed that, when having too small $\delta l$, the associated power of the involved temporal peaks are quite similar and the value for $\alpha$ gets lost in the uncertainty of the measurement. When employing the 2-PSTD, this necessary $\delta l$ is shared between $l_1$ and $l_2$ paths. However, when using 1-PSTD approach, all the delay must be carried onto the PLD of the MZI. Finally, just mention that 1-PSTD can be easily adapted to test $1 \times 2$ PS power ratio.

We have experimentally validated this technique by employing 1-PSTD in a private project [69] to test a technology platform. The fabricated devices were 1-PSTD models, including spirals in both arms only differing in their straight waveguide sections to implement the required $\delta l$, given the expected propagation loss in the technology platform. This is a fine-tuning optimization of the test structure that makes both MZI arms more comparable as it distinguishes between waveguide cross sections, cancelling out the bend sections when having exactly the same in both arms. The technique shows more robustness when compared to the other technique to retrieve waveguide propagation loss in the previous subsection, or other techniques to estimate coupler power splitting ratio [83].

Beyond, although not included here, the 2-PSTD model may be adapted to characterize optical coupler excess loss $\gamma$ of the optical couplers (MMI) as well. This can be carried out by inserting an MMI in one of the arms of one of the MZIs, in the role of a defect: this creates an asymmetry in the number of MMI hits between the different paths of the test structure that, when analyzed in the formulae 3.8, it can be solved for $\kappa$ and $\alpha$ as shown, and also for $\gamma$.

## 3.4 Relative phase measurements

Along the different of part of this thesis, OFDI direct time domain phase is retrieved. As argued in section 2.3.2, a powerful and robust assessment is the comparison between the phase retrievals corresponding to different contributions of the same measurement take. A good example are the incremental phase measurements between the array waveguides of an AWG that has provided us a mean

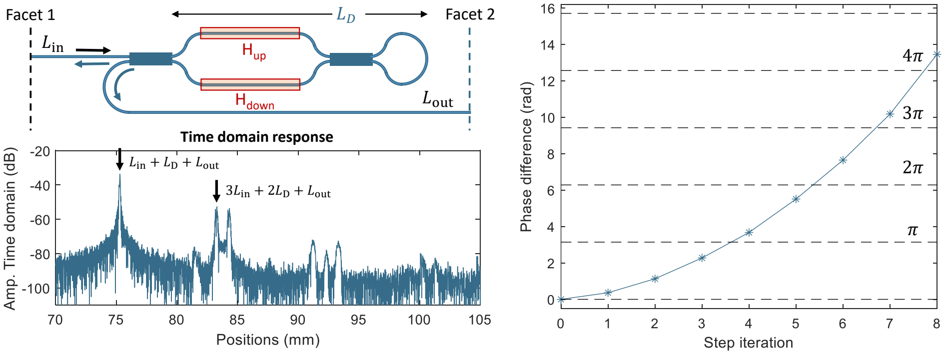

**Figure 3.15:** Sagnac interferometer based universal mirror: the device is represented at the top, while the retrieved time domain response is shown below. At the right, the phase curve after several heating iterations, is shown.

to assess phase errors (nonlinearities) coming from imperfect fabrication of the device. A silica-based telecom grade and other integrated AWGs in section 3.1. Also, the AWGs included in next chapter of this thesis regarding an integrated OFDI. Furthermore, in section 3.2 we have retrieved spectral phase measurement from individual temporal contributions of RRs as a mean to obtain chromatic dispersion of the waveguides. In this section, we want to include a couple more cases where temporal phase measurement has provided very valuable information about the measured device.

First case we want to review is a participation in a research work where an integrated device is proposed, a Sagnac interferometer tunable based mirror [85,86] where OFDI measurements were performed to aid in its characterization. The DUT is represented in Fig. 3.15 at the top left. It comprises a balanced MZI delimited by two MMIs whose outputs are connected to form a Sagnac interferometer. By controlling the electric voltage on the metallic thermal heaters put over each arm of the MZI ($H_{\text{up}}$ and $H_{\text{down}}$), the output MZI power ratio and phase is controlled, so that the input/output of the whole device (i.e. what is reflected and transmitted, through the MZI inputs), is controlled as well giving rise to a tunable universal mirror.

The most straightforward strategy to characterize a metal heater is by inspection of the spectral changes of a MZI where the heater is put over one of the arms and the voltage is increasingly raised, so that one entire FSR shift corresponds to a $2\pi$ phase shift between both MZI arms. As a result, the phase shift versus voltage curve can be obtained. However, if the heaters contained in a more complex device like the tunable mirror we are dealing with are intended to be tested directly, this approach may be not valid due to its more complicated spectral response or any other reason (e.g. this device has two outputs, reflected and transmitted, thus coinciding one of them with the input. With an OFDI measurement (in transmission mode in this case), the different involved paths of the DUT can be isolated in the time domain response. As it is customary, the virtual temporal light pulse can reflect on several parts of the DUT and on the chip facets as well. By following the light paths in this DUT, there is one direct transmitted contribution whose PLD is just the total length from facet 1 and 2, i.e. $L_{\text{in}}+L_{\text{D}}+L_{\text{out}}$, corresponding to the most powerful peak in Fig. 3.15 at the bottom. In this case, light hits the DUT once (and therefore the heaters), and the part of light that transmits reaches facet 2. In the immediately higher reflection order, we have two contributions. On the one hand, a part of the previous light pulse reaching facet 2 reflects back to the DUT. On the other hand, the portion of light that firstly hit the DUT and leaves it in reflection, goes to the facet 1 and reflects back to the DUT. Again, in both cases, a part of the light hitting the DUT for second time exits the DUT in transmission towards facet 2. An this dynamic goes on for higher order groups with increasing number of contributions and reduced power, as visualized in Fig. 3.15.

Taking advantage of this, the idea is to compare the phase of two peaks corresponding to different DUT hits in the same measurement take $n$, and associated to a heater applied voltage $V$. In this case, the indicated peaks in the figure, that we call $\phi^V_{1,n}$ and $\phi^V_{2,n}$. Assuming the retrieved phase for each has a constant phase $\phi_{0,n}$ that only depends on the measurement take (as argued in section 2.3.2), the retrieved phases are $\phi^V_{m,n}=\phi_{0,n}+\phi^V_m$ and computing their difference, $\Delta\phi^V=\phi^V_2-\phi^V_1$, we eliminate $\phi_{0,n}$. The phase difference $\Delta\phi^V$ contains the accumulated phase between the followed passive paths, $\phi_{\Delta x}$, which is invariant, and the action of the heater at voltage $V$, i.e. $\phi^V_2-\phi^V_1=\phi_{\Delta x}+\Phi_V$. So far, let us notice that this is the same phase assessment approach as in other works, with the added idea of comparing two contributions hitting the DUT once and twice, thanks to the chip facet reflections. As done for the AWG cases mentioned above, this is not restricted to two contributions comparison, but also for a group of several contributions. But we con go beyond: the phase comparison as $\Delta\phi^V$ is free from take variability and is comparable to the same phase assessment in other take. In this second-order relative phase assessment, if a parameter is changed from one take to the next, even any invariant phase contribution is eliminated and the actual phase change originated by that parameter can be directly evaluated. Therefore, if we do this operation for different iterations corresponding to different increasing voltages $V_i$ applied to one of the heaters, we can compare the quantities $\Delta\phi^{V_i}$ and eliminate $\phi_{\Delta x}$ too. Then, by normalizing $\Delta\phi^0=0$ to $V=0$ (step iteration 0), we finally have a curve resembling $\Phi_V$, as shown in the experimental curve in Fig. 3.15 at the right. The shape of the curve is what is expected for even steps of voltage increments, while the achieved phase difference is compatible to the expected for the device (for more details on the specific devices obtained conclusions, see manuscripts [85, 86]).

In a similar way, in a private research project [69], this type of phase measurements allowed us to assess heat crosstalk along the DUT. In this case, the addition is that the DUT comprised multiple different waveguide paths with different distances between them, all of them routed to the output facet of the chip. To get a measure of all of them in the same take, a reflectometric OFDI measurement through main input is performed, so that a set of temporal contributions corresponding to each path is well observed in the time domain. By comparing all of them to a single one reference, not involved in the chip directly (the temporal peak corresponding to input chip facet reflection), and heating a thermal heater placed in a specific position of the DUT, we were able to assess individual heat crosstalk to each of the DUT involved paths. This test, which gathers all the phase assessment ideas exposed in this thesis, turned out to be extremely useful as we found out a lot more heat crosstalk than expected at the beginning, having a revealing experimental evidence at our disposal.

## 3.5 Conclusions

In this chapter, we first provided some of the first OFDI real and successful tests over integrated devices. After that, a varied group of characterization applications using OFDI and different test structures is proposed and reviewed. All these applications, along with other existing ones, can be combined to form a whole highly equipped test structure characterization set. In fact, we have already explore this idea in a research project [69] where, summarizing, we have employed the following test structures using OFDI measurements:

- PSTD structure, to get propagation loss $\alpha_{\mathrm{SW}}$ and MMI splitting ratio $\kappa$. The test structure is optimized by the use of similar spiral structures, so that both MZI arms are only differing in straight waveguide section, having exactly the same number of bend sections and bend-straight waveguide transitions. Beyond, PSTD should be considered to be combined with integrated OFDI structures covered in next chapter.

- Set of RRs, using characterized $\alpha_{\mathrm{SW}}$ and $\kappa$, and changing slightly the employed cross-sections and bend-straight waveguide transitions, to get $\alpha_{\mathrm{B}}$, chromatic dispersion, bend-straight waveguide transition losses, also for different radii of interest, etc.

- Double RR, consisting of sorting two identical RRs serially, but mirrored with respect to the bus waveguide. In the time domain, both RR individual time domain responses are visualized, plus a set of contributions which makes a different number of roundtrips on each cavity, meaning different rightwards and leftwards bends travelled. In this way, additional evidence and characterization of bend polarization rotation is tested.

- Besides, test structures to double-check the obtained values, such as spirals to retrieve loss by reflectometry and MMI cascade to characterize MMI power splitting ratio [83].

Finally, in the characterization of the waveguides it is interesting to incorporate a technique to obtain $n_{\mathrm{eff}}$ [87], that would make the test structures set more complete.

## Chapter 4

# Integrated OFDI structures

In this last chapter of the thesis, we gather the results which have been obtained raising from the idea of integrating an OFDI architecture. Apart from the genuine exploration and demonstration, there are reasons that make conceive this approach as interesting to be applied by the photonics community.

In the first place, there are technological reasons, i.e. those arising from the advantages of using integrated waveguides instead of optical fiber. The most evident is the miniaturization of the system, which not only implies to have less bulky components, but also a re-scaling in the size and accuracy of the path length differences (PLD) which can be tailored. The shorter interferometer arms compensates the higher integrated waveguide propagation loss, as well as their typically high chromatic dispersion. However, the latter is a specially critical issue to take into account as it limits the spatial resolution in an OFDI measurement (section 2.4) of an integrated device under test (DUT), which in turn typically presents very near temporal contributions. Fortunately, as we show in section 4.1 there exist a dispersion de-embedding mechanism that is inherent to the fact that DUT and interferometers are made of the same waveguides. Integrated waveguides allow to achieve small PLD that translates into larger interferogram free spectral range (FSR) in the frequency domain, more readily resolvable in terms of wavelength resolution and accuracy by the photodetection and acquisition part of the setup, thus opening up door to other common laboratory equipment. The integrated waveguides as such stand out for their stability against external conditions, which does improve the measurement quality in terms of repeatability.

There are advantages at the layout level too: in some cases, unwanted contributions may be expected coming from cavities generated by on-chip reflections on chip facets, stitching transitions, unwanted reflective events, etc. Mach-Zehnder interferometer (MZI) path lengths can be engineered to avoid them to couple to the DUT response, even making a wider time domain window to pre-allocate them, so that an integrated OFDI is versatile against these possible contributions. Besides, it is remarkable the versatility provided by the employment of MZIs, in the sense that they are potentially adaptable to transmission or reflection interrogation of the DUT and allow any coupling strategy to chip (either butt or vertical coupling). They also minimize, in comparison to other interferometers, the presence of higher-order beatings feedback.

With all in mind, the integration of an OFDI as an external characterization instrument may be conceived. However, this approach is not straightforward: on the one hand, the optical connection between the integrated MZIs with an arbitrary DUT, which would be in different chip, must include an optical fiber pigtail as an interconnection optical medium, fixed to the interferometers. Taking into account different length scales between integrated and optical fiber waveguides, this would generate a great $\Delta l$, to be reduced with long delay line in the reference arm of the DUT-MZI. Further, the DUT may show arbitrary length characteristics (average length $l_\mathrm{D}$ and width $\delta l_\mathrm{D}$). This forces the integrated MZIs PLDs to be large enough to hold a given DUT maximum length as an specification or, conversely, to have tunable PLD capabilities which may be implemented by tunable optical delay lines, involving active parts in the body of the MZIs [88–91], or well by considering any external strategy as for example optical fiber to do the task, involving again off-chip optical connection and more complexity due to the use of different waveguides with the corresponding optical transitions in the same MZI. Definitely, each of these different solutions may be contemplated, although they imply a more complex implementation out of a purely passive integration. It is sticking to the passive approach where an integrated OFDI interferometric part may be conceived as test structure, which would make a significative leap in the characterization of integrated DUTs, or even to be combined with techniques such those developed in this thesis and covered in chapter 3, to aid in the fabrication workflow of the development of PICs.

This is the direction followed in our research and thus, the contents of this chapter. First, as a preamble we describe the integration of an OFDI in the following section. After that, we show the results in section 4.2 for the first attempt of integrating the interferometric part of an OFDI along with an arrayed waveguide grating (AWG) in silicon nitride (SiN), which were published in [54]. Finally, in section 4.3 we go for the last step we took in pursuing a more established and practical test structure, which involves a novel inteferometric structure (a three-way MZI), giving all the technique details and a wider experimental proof in SiN and silicon-on-insulator (SOI), different DUTs, external source and photodetection part, etc., that was published in [55]. Of course, in the last section we draw our conclusions and discuss perspectives.

## 4.1 OFDI waveguides integration

The description of the integrated version of an OFDI system is formally similar to the conventional external one. In fact, it can be considered as a special case. The co-integration of the interferometric part of the OFDI setup along with the DUT is sketched in Fig. 4.1 at the top: the MZIs are implemented through integrated

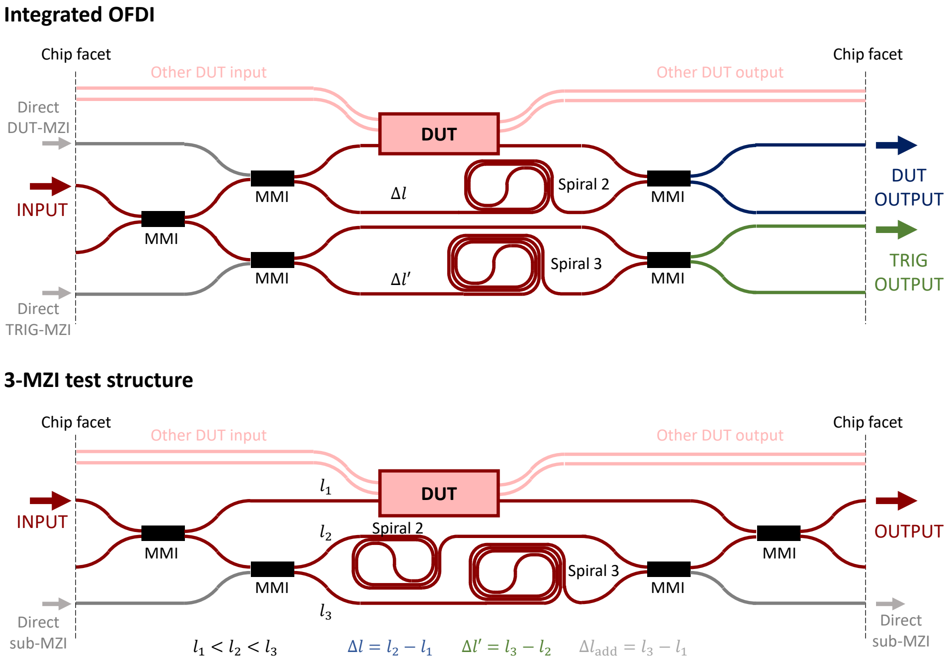

**Figure 4.1:** Sketch of the integrated OFDI models in this chapter: at the top, the direct co-integration of the interferometric part along with DUT. At the bottom, the novel interferometric test structure forming a three-way MZI.

waveguides and the optical couplers are typically $2 \times 2$ MMIs in our case, for convenience in terms of compactness and better broadband behaviour than other implementations. The required optical delays can be implemented by means of spiral structures, as represented. The whole device has a single duplicated input, and two duplicated outputs for both the DUT and TRIG interferometers (in blue and green color, respectively). Besides, the $2 \times 2$ MMIs allow for direct access to each MZI and other DUT input/output can be accessed independently whether that is the case.

Let us recall the interferogram expressions for both DUT and TRIG cases in Eqs. 2.11 and 2.9 in section 2.2, respectively. On the one hand, we have a DUT-MZI interferometer characterized by its $\Delta l$ and its propagation constant $\beta$ for the waveguides forming it (sticking to the limit of lossless waveguides). The DUT is described by its transfer function given by eq. 2.10, where $l_{\mathrm{D}}$ is its average length and $\beta_{\mathrm{D}}$ the propagation constant. The AC part of the resulting DUT-MZI interferogram is governed by $I \propto |H| \cos(\beta\Delta l - \beta_{\mathrm{D}} l_{\mathrm{D}} + \phi_{\mathrm{D}})$, i.e. the expected cosine function modulated by $H(\omega)$ modulus and recording both propagation features of the MZI and the DUT waveguides, as well as the optical phase response of the DUT, $\phi_{\mathrm{D}}$. As for the TRIG-MZI, the oscillatory part of the resulting interferogram $I'$ provides the set of sampling points $\beta'_m$ as the rising roots of the sinusoid, according to the linearization condition in Eq. 2.12:

$$I' \propto \cos\left(\beta \Delta l'\right) \rightarrow \beta_m = \frac{\frac{3\pi}{2} + 2\pi m}{\Delta l'}, \text{ where } m \in \mathbb{Z}. \tag{4.1}$$

Following the OFDI process, the points $\beta_m$ in Eq. 4.1 resample the DUT-MZI interferogram in order to remove nonlinearities coming from the tunable laser (TL) sweep (not included in this model) and provide a linearization in $\omega$, a required condition to properly apply the fast Fourier transform (FFT) algorithm. In a conventional OFDI setup, optical fibers are the common waveguides employed for the MZIs, and due to its low dispersion it can be assumed $\beta(\omega) \propto \omega$ in the working bandwidth, so that a proper linearization in $\omega$ can be assured, as argued in chapter 2. In this case, the presence of DUT dispersion given by $\beta_{\mathrm{D}}$ manifests as a chirp in the DUT-MZI interferogram entailing a broadening of the time domain events that, in turn, limits the ideal spatial resolution in OFDI $\delta z_{\mathrm{id}} = \lambda^2 / \left(n_g \Delta\lambda\right)$, determined by the sweep span $\Delta\lambda$ and being $n_g$ the average group index. A technique to de-embed dispersion would be required, being the common way to assume a second-order model to fit the interferogram so that once parameters are deduced, interferogram is inversely chirped (e.g. by a nonlinear resampling) [37,47].

However, in light of Eq. 4.1, when the condition $\beta(\omega) \propto \omega$ cannot be met (as it is the case when we consider integrated waveguides), it can be only ensured a linearization in $\beta$ with a step of $\delta\beta = 2\pi/\Delta l'$. In this way, for arbitrary non-trivial $\beta$ we have a complicated scenario where the resampling is made, in general, nonlinearly in $\omega$ of a DUT response whose waveguides have a different propagation constant $\beta_{\mathrm{D}}$. Nonetheless, it is reasonable to make an important assumption in the case of integrated OFDI: the integrated waveguides conforming the DUT and the MZIs can be considered the same in terms of propagation conditions, provided that the DUT possible different sections are short and/or not too different. This consideration can be adopted in the analysis by computing $\beta_{\mathrm{D}} = \beta$, so that by introducing 4.1 in the DUT interferogram, we obtain the resampled DUT interferogram as:

$$I_m = 2\left|H\left(\beta_m\right)\right| \cos\left(\left(\frac{3\pi}{2} + 2\pi m\right)\frac{\Delta l}{\Delta l'} - \phi\left(\beta_m\right)\right). \tag{4.2}$$

In Eq. 4.2 we have, on the one hand, the amplitude of the DUT modulating a cosine. Within, depending on the PLDs ratio $\Delta l/\Delta l'$ there is a constant phase, and a linear term on $m$ that basically traces the cosine function. Last, and most importantly, there is the optical phase response of the DUT sampled linearly in $\beta_m$ (as given by Eq. 4.1) as the only arbitrarily varying phase term. Any nonlinear $\beta$ dependence is automatically cancelled, having a very special case where *integrated OFDI inherently provides a compensated version of the DUT response regardless of the degree and order of present dispersion of the waveguides.* This is a remarkable characteristic as it permits to tighten the actual spatial resolution of the system to the ideal one, especially important when considering integrated

DUTs where feature sizes are particularly small and dispersion is often some magnitude orders above than in optical fibers. From another point of view, what we formally obtain after applying inverse FFT with this particular linearization in $\beta$, which is ultimately responsible of the dispersion de-embedding mechanism, is the spatial domain response of the DUT, a version of the impulsive domain free from time-related effects like temporal broadening.

Under these special circumstances, we get automatically the spatial domain response of the DUT with a perfect compensation of any order of dispersion, but we also lose the possibility of directly quantifying propagation properties, since the corresponding phase contributions overlap the TL sweep nonlinearities in the interferograms and cancel out in the linearization. For example, the typical way from which $n_{\mathrm{g},0}$ is deduced 2.19 in chapter 2 is no longer valid. There is still one way to proceed: from Eq. 4.1, the step $\delta\beta = 2\pi/\Delta l'$ determines the $\beta$ span as $\Delta\beta = N_{\mathrm{osc}}\delta\beta$, where $N_{\mathrm{osc}}$ is the number of oscillations in the swept band. On the other hand, assuming a second-order dispersive medium, it is straightforward to relate to wavelength as $\Delta\beta = 2\pi n_{\mathrm{g},0}\frac{\Delta\lambda}{\lambda_1\lambda_2}$ (it is straightforward to show that this expression for $\Delta\beta$ is only affected by odd order terms of the $\beta = \beta(\omega)$ series). By equating both expressions, $n_{\mathrm{g},0}$ can be solved as:

$$n_{\mathrm{g},0} = \frac{\lambda_1\lambda_2}{\Delta\lambda\Delta l'}N_{\mathrm{osc}}, \tag{4.3}$$

in such a way that $n_g$ can be estimated by relying on sweep wavelength boundaries, the designed $\Delta l'$ for the TRIG-MZI, and the observed number of oscillations $N_{\mathrm{osc}}$, in a derivation equivalent to the employed in [92]. In order to estimate higher-order propagation parameters, a reliable reference to actual frequency would be required to isolate dispersion effects in the interferogram. Therefore, in case of being interested on calculating dispersion parameters in this context, an approach as the followed in [47] might be employed: a TL step-by-step scanning avoiding nonlinearities, so the contained phases in the interferogram would come only from the integrated waveguides dispersion, then computing a fitting to a theoretical model.

To illustrate the effects of dispersion in the time domain, in Fig. 4.2(a) is shown a simple numerical simulation of the time domain of an AWG with a FSR of 32 nm and 41 waveguides in the array (same design, with less array waveguides, as the AWG in the following experimental section) measured with an external OFDI. As it is explained in chapter 1, in the AWG the light in the slab coupler illuminates the waveguides in the array with a natural Gaussian shape, then each propagating with increasing path length. The expected train of pulses separated 0.24 ps are completely superimposed and indistinguishable when measuring with MZI waveguides being fiber (i.e. $D_{\mathrm{fib}} \simeq 18$ ps/(nm km), lengths in the order of meters, PLDs in tens of cm) the AWG, whose integrated waveguides have a measured dispersion of $D_{\mathrm{iw}} = -1430$ ps/(nm km) [10]. In Fig. 4.2(b), the same AWG measured with an integrated OFDI, where the lengths are similar to the designed ones for the real device in the following section (few centimeters), shows an almost perfect comb of contributions, being the slight distortion of the Gaussian

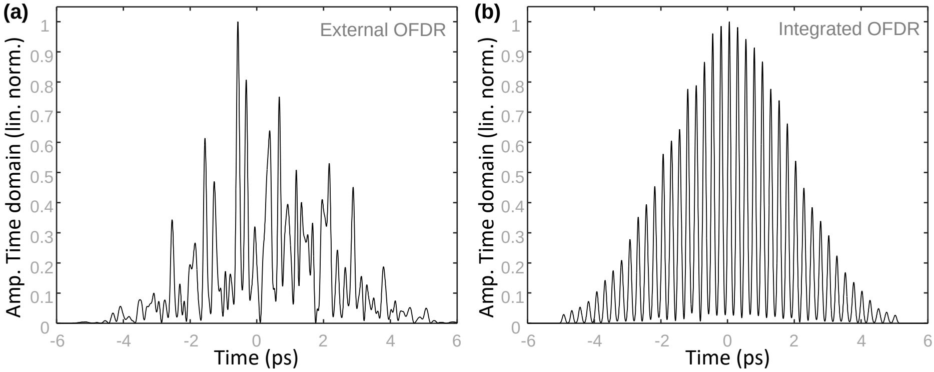

**Figure 4.2:** Numerical simulation of the time domain response of a 41-waveguide AWG (a) measured with an external OFDI and, (b) with an integrated OFDI system.

envelope the only visible effect due to the weak interaction between the adjacent contributions.

## 4.2 Proof of concept

In this section we report the experimental validation of the first integrated OFDI. The device chip was fabricated on the CNM-VLC SiN platform [1], where a $Si_3N_4$ guiding film height of 300 nm is fabricated by low pressure chemical vapor deposition (LPCVD) over a 2.5 $\mu$m $SiO_2$ buffer platform, and covered by a deposited 2.0 $\mu$m $SiO_2$ cladding by plasma-enhanced chemical vapor deposition (PECVD) [1,10]. Deeply etched rectangular waveguides of 1 μm width designed for single-mode operation at $\lambda = 1550$ nm are employed for the routing.

A picture of the fabricated device is shown in Fig. 4.3. The device is fed via one of the two central inputs at left facet, then reaching a first optical coupler to split optical power implemented by a 50:50 MMI. Next, the signal is routed to the MZIs, where DUT and TRIG interferograms are correspondingly generated. The DUT is a $5 \times 5$ channel AWG designed with 59 waveguides in the array and a FSR of 32 nm (4 THz), having an average length of approximately 3 mm and a difference between the shortest and the longest arm, or a width, of $\delta l_{\mathrm{D}} = 2.285$ cm. In order to engineer the spatial domain parameters, an spiral of 13 mm implements a PLD for the DUT-MZI of $\Delta l = 9.8$ mm to account for the DUT length. For the TRIG-MZI, an spiral of 40 mm is chosen to have $\Delta l' = 36.9$ mm. These PLDs fulfill Nyquist criterion for the conventional sampling of 1 S/TRIG oscillation (which results into 3.7 resampling points for the DUT interferogram in the linearization) and are intentionally set large enough to ensure room for the proof-of-concept. In an optimized design, PLD may have been tighten up to 0.30 and 0.85 mm, approximately. The beating signals are simultaneously collected at two of each pair, DUT and TRIG, of available outputs to be photodetected.

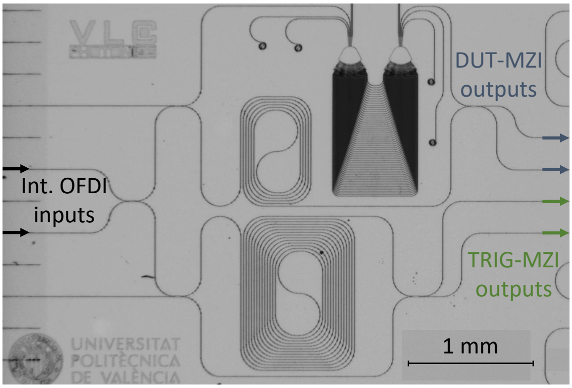

**Figure 4.3:** Microscopy picture of the fabricated integrated OFDI in SiN. The AWG is accessed through their central input/output, whereas the others are terminated or accessed externally (above, not shown in the picture). The corresponding PLDs are implemented through spiral structures, while the whole input and outputs are indicated with black and color arrows.

For the measurements, the TL provides the swept signal that is horizontally coupled to the chip, making use of a polarization controller plus microscope objective and a linear polarizer to ensure fundamental TE mode excitation. After travelling through the chip circuitry, the light is collected simultaneously at both the TRIG and the DUT outputs by means of a lensed fiber array. Both signals are photodetected and the resulting electrical signal is converted to digital data by means of the DAQ, stored and ready to be processed. The employed measurement equipment can be found in section 2.1. The TL scan span is $\Delta\lambda = 80$ nm centered at $\lambda_0 = 1550$ nm and the resulting interferograms are shown in Fig. 4.4. A compromise between scan speed $v_{\mathrm{TL}} = 20$ nm/s and acquisition rate (100 kS/s per channel) is adopted so the interferograms are properly sampled. As designed, the TRIG-MZI generates interference fringes (green) with a FSR close to a fourth the corresponding ones to the DUT-MZI. The extinction ratio decreases for increasing wavelength, due to the combined wavelength dependance of different factors such as the MMIs splitting ratio or the chip coupling. In the interferograms shown, the DC contribution have been removed as specified in section 2.3.1. Next, after applying the processing and inverse FFT to the DUT interferogram, the spatial domain response is obtained. From the number of sampling points in the working wavelength span, using formula 4.3 we deduce $n_g = 1.894 \pm 0.001$. In Fig. 4.5(a) (black solid curve) the AWG spatial domain response is shown: the train of waveguide pulses, whose measured average separation is $37.3 \pm 0.1$ $\mu$m (corresponding to the designed FSR) is perfectly distinguishable with a high visibility and with the characteristic slab coupler far field gaussian envelope [19, 93]. The deviations from the Gaussian envelope are likely due to a combination of actual events such as waveguide imperfections and polarization fading, as well as the previously il-

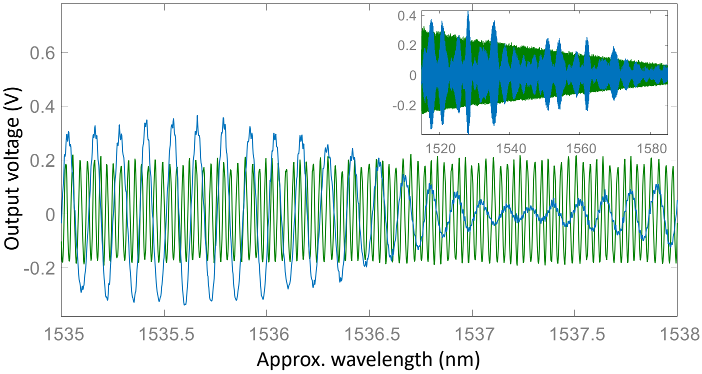

**Figure 4.4:** Interference fringes corresponding to the TRIG-MZI (green curve) and to the DUT-MZI (blue curve). In the inset, the same plots in a broader wavelength range.

lustrated measurement induced pulse overlap (as we observed in the simulations in Fig. 4.2(b)).

The experimental spatial resolution of the system can be estimated by computing the full width at half maximum (FWHM) of fitted Gaussian functions to the AWG peaks of a selected set, in particular the 34 central ones enclosed by the grey dashed vertical lines in Fig. 4.5(a). The calculated average spatial resolution is $\delta z_{\text{exp}} = 18.5 \pm 1.7\ \mu\text{m}$, whose associated error contains the ideal value that we calculated to be $\delta z_{\text{id}} = 17.4\ \mu\text{m}$, corresponding to the analyzed (slightly reduced) $\Delta\lambda$ and derived $n_g$. This constitutes a robust proof of the dispersion de-embedding mechanism described above. In Fig. 4.5(b), the phase difference between consec-

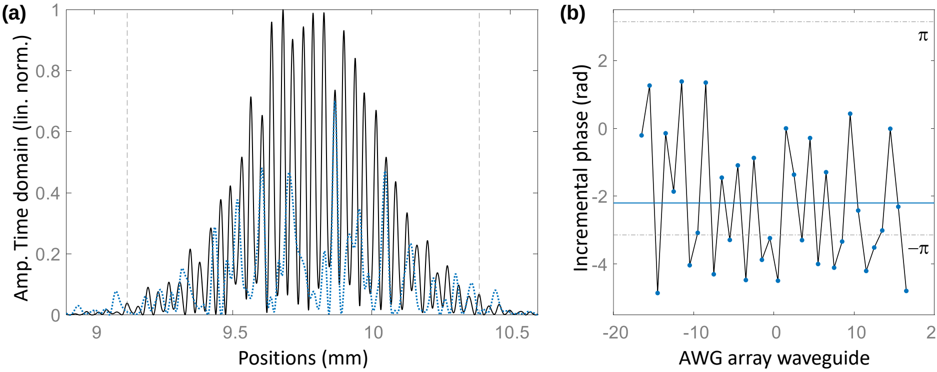

**Figure 4.5:** (a) Spatial domain response of the AWG obtained with integrated OFDI (black solid curve) and external OFDI (blue dotted curve) measurements. (b) Phase difference between the consecutive contributions enclosed by the vertical lines, resolved by integrated approach.

utive arrayed waveguides contributions (from the selected set, taken at the peaks) is shown. By design, the phase difference is constant since AWG is designed with a constant length difference between consecutive waveguides, as well as with perfect focusing from (to) the AWG input (output) waveguides in both slab couplers. For this particular and specially selected DUT, the measured phase errors [19] are sign of an AWG with degraded response [93]. For completeness, the observed average phase difference (represented by the blue straight line) is related to the global phase given by 4.2 [94] combined to the real mean phase corresponding to the incremental length of the waveguides in the AWG.

An external OFDI measurement of the AWG is performed to be compared with the integrated version. The use of an external OFDI setup to interrogate the DUT (the same combination of central input/output) is possible by accessing the device either through one of the main integrated OFDI inputs, or even the direct input to DUT-MZI above. Similarly, the resulting signal is collected from the chip through one of the main outputs. The external fiber-based MZIs have $\Delta l_{\mathrm{ext}} = 13$ cm and $\Delta l'_{\mathrm{ext}} = 83$ cm, so that it is possible to distinguish between the AWG and the reference arm contributions in a time domain window whose width is an order of magnitude wider. The use of the same waveguides for both the DUT and the MZIs (i.e. the same propagation constant) automatically provides a dispersion-compensated version of DUT response. When using fibers, due to the huge offset between the propagation constants we can assume the fiber as a non-dispersive medium in a first approximation, so the integrated waveguide dispersion is not compensated leading to a temporal broadening that corresponds to a spatial resolution of about 165 µm, according to Eq. 2.20 and Fig. 2.5 for this measurement. In Fig. 4.5(a), the resulting spatial domain response for this case is shown in blue dotted curve where, in agreement with the simulations in Fig. 4.2, the interference between the broadened consecutive peaks prevents to resolve the individual contributions. Not even if the measurement were set to the maximum achievable spatial resolution $\simeq 77.2$ µm for $\Delta\lambda = 23.3$ µm, according to Eq. 2.21, and considering the measured dispersion for this technology in section 3.2.

The FFT can be applied to selected parts of the impulsive domain at will, so that the spectral response of that selection is recovered. In Fig. 4.6 the spectral amplitude reconstruction of the AWG for the case of integrated OFDI measurement (black solid curve) and for the external OFDI (blue dotted curve) are shown. The almost perfect agreement between both traces demonstrates that even though the spatial response was not properly resolved by the external OFDI, the device works the same way in the spectrum. This is an important point: the integrated OFDI mechanism provides a mean to distinguish features temporally/spatially closer, but it actually does not change the performance of the device. In fact, as it can be seen in the Fig. 4.6, the defective performance of the AWG can be observed anyway. However, and remarkably, the integrated OFDI allowed us to locate the degradation source, and identify it as the strong phase deviation from linearity between the array waveguides (Fig. 4.5(b)) thanks to the dispersion de-embedding intrinsic mechanism, otherwise not straightforward with the external OFDI.

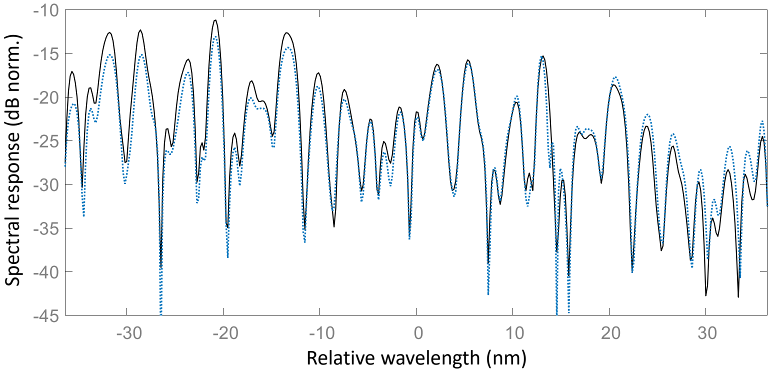

**Figure 4.6:** Spectral reconstruction of the AWG spatial domain response from the integrated OFDI (black solid curve) and external OFDI measurements (blue dotted curve).

## 4.3 Compact 3-MZI Test Structure

The most disturbing and impractical characteristic of the integrated OFDI discussed in previous section is the fact that two optical output channels are required to be active, monitored and detected. On the one hand, this implies that, apart from the input, two optical fibers have to be aligned, so that two pigtails are on the same side of the chip and sharing very little space for both. This is something that has to be addressed ad-hoc, taking into account that characterization setups on integrated optics are typically single input and single output (as in Fig. 1.2), or either through the use of an optical fiber array, with the more tricky alignment associated. Not only that, two optical fields have to be photodetected and sampled too (as explained in chapter 2, section 2.1).

In this context, a novel interferometric test structure, consisting of a three-way MZI (3-MZI), is proposed to strongly reduce these practical issues and being still capable to produce exactly the same data. Conversely, it involves a specific design associated to an additional pre-processing step, that we detail in what follows. This technique is broadly demonstrated for different DUTs in different photonic integration technologies, involving different coupling strategies, as well as employing different external equipment than the usual thanks to the advantages of the integrated approach mentioned in the introduction of this chapter. These results were fully published in [55], and previously and partially in some conferences [95–97].

### 4.3.1 Test Structure description

Let us consider a photonics platform where optical propagation through the routing waveguides is described by the propagation constant $\beta(\lambda)$. As shown in Fig. 4.1 at the bottom, the light follows three different paths in the 3-MZI structure. We define $l_2$ and $l_3$ as the corresponding lengths for the delay paths, that are implemented by spiral structures, whereas the short arm, with average path length $l_1$ such that $l_1 < l_2 < l_3$, is composed of routing waveguide plus the DUT, which gets described by its transfer function $H(\lambda) = |H(\lambda)| \exp(-i\beta_{\mathrm{D}} l_{\mathrm{D}}) \exp(i\phi_{\mathrm{D}}(\lambda))$ where its spectral phase response is represented by $\phi_{\mathrm{D}}(\lambda)$. Taking into account that $2 \times 2$ splitters are typically used (mostly implemented by MMIs), there are different combinations that may implement a 3-MZI. The most appropriated choice, qualitatively, is to leave the DUT path to be the least lossy one, as shown in the sketch. In this configuration, it is like having a conventional sub-MZI embedded into the reference arm of a DUT-MZI. Thus, in order to get the resulting field of superimposing the 3 contributions, we can take the MZI fields from Eq. 2.8, where it is assumed 3-MZI input through input 0 (i.e. the one at the top), and consider $\mu_1 H$ instead of $\mu_0$, and the output 0 contribution of a MZI $\gamma(\mu_2 - (\mu_2 + \mu_3)\kappa)$ replacing $\mu_1$, to account for the sub-MZI with $l_2$ and $l_3$ lengths. This operation, for both outputs, results into a field that is superposition of three terms as $C_1 H \mu_1 + C_2 \mu_2 + C_3 \mu_3$, where the path coefficients $C_i$ $(i = 1, 2, 3)$ stand for the accumulated propagation and optical splitters losses in each case, that are:

| | Field 0 | Field 1 |
|---|---|---|
| $C_1$ | $\gamma(1-\kappa)$ | $\gamma\sqrt{\kappa}\sqrt{1-\kappa}$ |
| $C_2$ | $-\gamma^2(1-\kappa)\kappa$ | $\gamma^2\sqrt{\kappa}\sqrt{(1-\kappa)^3}$ |
| $C_3$ | $\gamma^2\kappa^2$ | $-\gamma^2\sqrt{\kappa^3}\sqrt{1-\kappa}$ |

In order to get the optical field intensity which gives us what we call the superinterferogram, we calculate the modulus of the field that, after some algebra, can be expressed as $I_{3\text{-MZI}} = I_{\mathrm{DC}} + I_{\mathrm{AC}}$, where:

$$\begin{aligned} I^{\mathrm{DC}} &= C_1^2 \mu_1^2 H^2 + C_2^2 \mu_2^2 + C_3^2 \mu_3^2 \\ I^{\mathrm{AC}} &= 2\left(C_1 C_2 \,\mathrm{Re}\left(H^* \mu_1^* \mu_2\right) + C_1 C_3 \,\mathrm{Re}\left(H^* \mu_1^* \mu_3\right) + C_2 C_3 \,\mathrm{Re}\left(\mu_2^* \mu_3\right)\right). \end{aligned} \tag{4.4}$$

where we make some notation simplification with some complex numbers as $\mu^2 \leftrightarrow |\mu|^2$. The superinterferogram AC terms involving $H$ can be solved as$\mathrm{Re}\left(H^* \mu_1^* \mu_i\right) = |H|\, \mathrm{e}^{\alpha(l_1+l_2)/2} \cos(\beta(l_i - l_1) - \beta_{\mathrm{D}} l_{\mathrm{D}} + \phi_{\mathrm{D}})$, while the other AC term $\mathrm{Re}\left(\mu_2^* \mu_3\right) = \mathrm{e}^{\alpha(l_2+l_3)/2} \cos(\beta(l_3 - l_2))$. There are 3 oscillatory contributions superimposed, corresponding to each sub-MZI: the TRIG contribution, with PLD given by $\Delta l' = l_3 - l_2$, the DUT contribution at $\Delta l = l_2 - l_1$, and an additional one carrying DUT response as well at $\Delta l_{\mathrm{add}} = l_3 - l_1$. In this way, the AC term of the superinterferogram condenses the interferograms we require to do OFDI, superimposed at the different combinations of paths. In the next subsection, we describe how we need to design the device in order to carry out the pre-processing step that allows to isolate DUT and TRIG interferograms (and discard ADD one).

When the DUT has more than one different path lengths, thus having a DUT spatial width $\delta l_{\mathrm{D}}$, we consider it to have a set of $N_{\mathrm{D}}$ contributions placed at $l_{\mathrm{D},n}$, with the integer $n = 1, \ldots, N_{\mathrm{D}}$, in the range $[l_{\mathrm{D}} - \delta l_{\mathrm{D}}/2, l_{\mathrm{D}} + \delta l_{\mathrm{D}}/2]$, so that its transfer function can be expressed as:

$$H = \sum_n H_n \mathrm{e}^{-i\beta_{\mathrm{D}} l_{\mathrm{D},n}} \mathrm{e}^{i\phi_{\mathrm{D},n}} \tag{4.5}$$

In this case, the mentioned DUT and ADD contributions will be a group of contributions with an extent $\delta l_{\mathrm{D}}$ in the given range. Additionally, the DC contribution in Eq. 4.4 carrying $|H|^2$ will have an extent as well, as:

$$\begin{aligned} |H|^2 = H^* H &= \sum_n \sum_m H_n^* H_m \mathrm{e}^{-i\beta_{\mathrm{D}}(l_{\mathrm{D},m}-l_{\mathrm{D},n})} \mathrm{e}^{i(\phi_{\mathrm{D},m}-\phi_{\mathrm{D},n})} \\ &= \sum_n |H_n|^2 + \sum_{n\neq m} H_n^* H_m \cos\left(\beta_{\mathrm{D}} \Delta l_{\mathrm{D},mn} - \Delta\phi_{\mathrm{D},mn}\right). \end{aligned} \tag{4.6}$$

This constitutes what we call the DUT self-beatings, corresponding to the internal interferences of the DUT. All these contribution broadenings associated with the non-trivial DUT extent are at the starting point in the design of the device, that we address in the following subsections.

### 4.3.2 Pre-processing step

In order to recover DUT and TRIG interferograms, a pre-processing step is required, which basically comprises Fourier filters onto the super-interferogram. An inverse FFT is applied to the detected super-interferogram and, similarly as in OFDI, an impulsive domain picture of $I_{3\text{-MZI}}$ is obtained. According to the design PLDs of the device, the different contributions are identified, including those of interest at $\Delta l$ and $\Delta l'$ impulsive positions. Then, we define crop windows (i.e. defined unaltered regions, and zeros elsewhere) to separatedly isolate them. These crop windows may be apodized or not, depending on the necessities, although simple squared crop windows are enough since the impulsive domain traces shall not have the problem of sharp edges or Gibbs effect [61]. Once DUT and TRIG contributions are properly separated, the last step is to apply FFT to this cropped portions and trace the real part so that the phase information gets tracked by the well-known sinusoids. It turns out that the retrieved spectra coincide exactly with the OFDI unprocessed interferograms, containing essentially the same features as if they were measured separately, as those in previous section 4.2. The only remarkable difference is that, accidentally, the pre-processing step includes a Fourier filtering of $I_{DC}$ and any vestige of spurious events placed at different impulsive positions different than the PLD of the interferograms themselves, one of the strategies to de-embed DC contributions, mentioned in chapter 2, section 2.3.1. As for the rest, the interferograms conserve all the features related to the measurement, and of special importance those affecting the phase, including the whole phase information of the DUT, the sampling in wavelength (nonlinear in frequency, something that almost all commercial light source plus photodetection solutions in photonics provide), waveguides chromatic dispersion and scanning nonlinearities. Therefore, this would be the canonical starting point to apply OFDI processing. However, we must first quantify the effects of these phase contributions onto the impulsive features when doing the pre-processing step, since we need to determine $l_1$, $l_2$ and $l_3$ lengths of the 3-MZI such that the DUT and TRIG contributions do not overlap with any other in the impulsive domain (something that we address in the next subsection).

In an OFDI experiment, the finite bandwidth conditions of the sweep given by the span $\Delta\lambda$, centered at $\lambda_0$, restrict the width of the peaks in the time domain picture when applying inverse FFT to a frequency linearized spectral trace (i.e. the re-sampled interferogram). As detailed in section 2.3.2, chapter 2, this is a fundamental constraint that determines the ideal spatial resolution of the system to be $\delta z_{\mathrm{id}} = \lambda_0^2/\left(n_{g,0}\Delta\lambda\right)$, where $n_{g,0}$ is the group index for $\lambda_0$. Apart from this, in the real world spatial resolution gets worse when the employed waveguides are dispersive media [37], as explained in section 2.4 of the same chapter. Nonetheless, in the pre-processing step applied to the super-interferogram, we apply inverse FFT to a trace linearly sampled in wavelength, due to the wavelength scanning provided by common lab equipment. The fact the signal is non-linearly sampled in frequency and, altogether with the chromatic dispersion of the waveguides, entails an additional broadening of the contributions in the impulsive domain that we derive in what follows. We assume ideal wavelength linear scanning, as light source sweep phase errors are not deterministic and depends on the specific employed equipment (this may be considered ad-hoc).

Let us consider a simple interferogram whose AC part varies according to $I^{\mathrm{AC}} \propto \cos\left(\beta x\right)$, where $x$ is the PLD of the interferometer and $\beta$ the propagation constant of the waveguides composing it. We regard a second-order dispersion modelled by propagation constant series, as given by Eq. 2.2 but wavelength-resolved, $\beta = \beta\left(\lambda\right)$:

$$\beta\left(\lambda\right) = \frac{2\pi n_0}{\lambda_0} + 2\pi n_{g,0}\left(\frac{1}{\lambda} - \frac{1}{\lambda_0}\right) - \pi c \lambda_0^2 D \left(\frac{1}{\lambda} - \frac{1}{\lambda_0}\right)^2, \tag{4.7}$$

where $n_0$ is the effective index for $\lambda_0$, $c$ is the speed of light in vacuum and $D$ is the well-known dispersion parameter that relates to the group velocity dispersion. The presence of any phase contribution or nonlinearity is well recorded by the FSR of the interferogram. This figure can be retrieved from the interferometer resonance condition $\beta x = 2\pi m$, where $m \in \mathbb{N}$ is the interference order, by computing the variation of the $\lambda$ with respect to $m$ (i.e. per oscillation):

$$\Delta\lambda_{\mathrm{FSR}} = -\frac{2\pi}{x}\left(\frac{\partial\beta}{\partial\lambda}\right)^{-1} = \frac{\lambda_0^2}{n_{g,0}x}\,\frac{1}{\left(\frac{\lambda_0}{\lambda}\right)^2 + 2\chi\left[\left(\frac{\lambda_0}{\lambda}\right)^3 - \left(\frac{\lambda_0}{\lambda}\right)^2\right]}, \tag{4.8}$$

with $\chi \equiv -\frac{\lambda_0 c D}{2n_{g,0}}$ being the dispersion coefficient and $\chi \geq 0$ provided that we have normal dispersion (i.e. $D \leq 0$). In the center of the band, the FSR is $\Delta\lambda_{\mathrm{FSR}}(\lambda_0) = \lambda_0^2/\left(n_{g,0}x\right)$. Anywhere else, the FSR corresponds to a different $x_{\mathrm{eff}}$, such that $\Delta\lambda_{\mathrm{FSR}}(\lambda) = \lambda_0^2/\left(n_{g,0}x_{\mathrm{eff}}\right)$. The variation of $x$ in the whole band basically gives us an estimation of the impulsive contributions broadening:

$$\frac{\Delta x}{x} \simeq -\frac{\Delta\lambda}{x}\left.\frac{\partial x_{\mathrm{eff}}}{\partial\lambda}\right|_{\lambda=\lambda_0} = 2B_\lambda', \tag{4.9}$$

where $B_\lambda' \equiv B_\lambda\left(1+\chi\right)$ and $B_\lambda = \Delta\lambda/\lambda_0$ is the fractional bandwidth. Therefore, each single PLD generated in the super-interferogram will involve a range

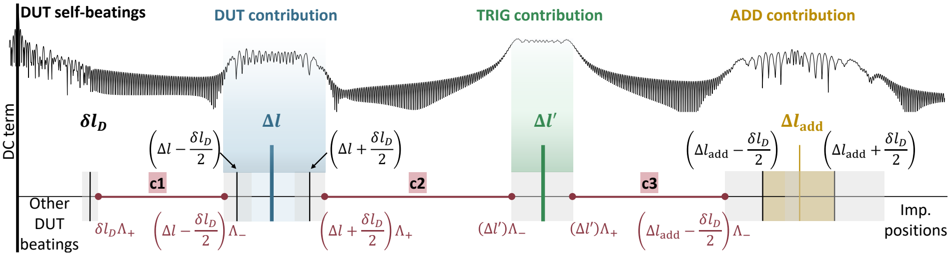

**Figure 4.7:** Schematic picture of the impulsive response of the super-interferogram: the different contributions are expected to appear at their impulsive positions, each of them with a given width. The non-overlapping conditions c1, c2 and c3 are imposed by choosing a given gap distance (thick red line) between these contributions.

$\{x\Lambda_-, x\Lambda_+\}$ in the impulsive domain, where $\Lambda_\pm \equiv 1 \pm B'_\lambda$, which depends on the wavelength band extent and the dispersion of the utilized waveguides. The predicted broadening in Eq. 4.9 can be straightforwardly confirmed by numerical simulation.

### 4.3.3 Test Structure design

Once it is known which are the impulsive contributions appearing in the impulsive domain, and what are there associated impulsive positions and widths due to the characteristics of the measurement and waveguides, we can establish design rules for the 3-MZI (i.e. ultimately determine $l_1$, $l_2$ and $l_3$) and thus ensure the proper functioning of the technique. Summarizing, we need to avoid DUT and TRIG contributions from overlapping to any other contribution and at the same time, ensure that Nyquist criterion is fulfilled. The former necessity can be imposed through the non-overlapping conditions, i.e. c1, c2 and c3 distances highlighted in thick red line in Fig. 4.7 to be greater than a safety distance $sx$.

Let us consider a DUT with a given spatial width $\delta l_{\text{D}}$ that, when inserted in the short arm of the 3-MZI test structure, has an average length $l_1$ that in general we try to minimize. The different combinations of the paths produce a landscape of contributions at the corresponding PLDs when switching to the impulsive domain after applying inverse FFT. They can be classified in one single contribution, and three group of impulsive contributions involving the DUT paths:

- **DUT self-beatings**, in the range $[0, \delta l_{\text{D}}]$,
- **DUT contribution**, in the range $\Delta l \pm \delta l_{\text{D}}/2$,
- **TRIG contribution**, in $\Delta l'$,
- **ADD contribution**, in the range $\Delta l_{\text{add}} \pm \delta l_{\text{D}}/2$,

where $\Delta l = l_2 - l_1$, $\Delta l' = l_3 - l_2$, $\Delta l_{\text{add}} = l_3 - l_1$ and from which we are interested in recover the second and the third. On the other hand, let us consider the experiment is planned under the wavelength scanning conditions of span $\Delta\lambda$ centered at $\lambda_0$, and the 3-MZI waveguides defined by $\beta(\lambda)$ as in Eq. 4.7, such that the impulsive contributions experience an added broadening as detailed in section 4.3.2. Let us consider, apart from the definitions therein, the parameter $\Lambda \equiv \Lambda_+/\Lambda_- = 1 + \delta\Lambda$, being $\delta\Lambda = 2B'_\lambda/(1 - B'_\lambda)$. We need to make sure that the impulsive contributions in the list above do not to overlap by imposing a safety distance $sx$ between them, so that the non-overlapping conditions are (see Fig. 4.7):

$$\begin{aligned} &\mathbf{c1}.\ (\Delta l - \delta l_\mathrm{D}/2)\,\Lambda_- - \delta l_\mathrm{D}\Lambda_+ \geq sx, \\ &\mathbf{c2}.\ \Delta l'\Lambda_- - (\Delta l + \delta l_\mathrm{D}/2)\,\Lambda_+ \geq sx, \\ &\mathbf{c3}.\ (\Delta l_\mathrm{add} - \delta l_\mathrm{D}/2)\,\Lambda_- - \Delta l'\Lambda_+ \geq sx. \end{aligned} \tag{4.10}$$

Apart from conditions **c1**, **c2** and **c3** in Eq. 4.10, in order to avoid aliasing in the linearization process once the DUT and TRIG interferograms are recovered, Nyquist condition must be fulfilled. By assuming the conventional sampling criterion where one sampling point per oscillation is taken from TRIG interferogram, Nyquist criterion can be split into the two following conditions:

$$\begin{aligned} &\mathbf{n1}.\ \Delta l - (\delta l_\mathrm{D}/2 + sx) \geq 0, \\ &\mathbf{n2}.\ \Delta l + \delta l_\mathrm{D}/2 + sx \leq \Delta l'/2. \end{aligned} \tag{4.11}$$

With input parameters $\{l_1, \delta l_\mathrm{D}, sx, \Delta\lambda, \lambda_0\}$, all these 5 conditions must be satisfied. This ultimately determines the minimum required values for $l_2$ and $l_3$ path lengths. The conditions **c2** and **n2** are the first to be inspected: they deal with the minimum distance between DUT and TRIG contributions to not overlap and assure correct linearization, respectively. This distance is governed by $l_3$ in function of the $l_2$ length that is decided afterwards. By solving the inequalities for $l_3$ and inspecting, it is straightforward to see that **n2** is always greater and therefore, we set auxiliary $l_{3,\mathrm{aux}} = 3l_2 - 2l_1 + 2sx + \delta l_\mathrm{D}$. On the other hand, the remaining conditions **n1**, **c1** and **c3** are the ones to determine $l_2$. By solving, using $l_{3,\mathrm{aux}}$ expression for **c3** and re-arrange conveniently we find:

$$\begin{aligned} &l_{2,\mathrm{min}}^{\mathrm{n1}} = l_1 + (0.5)\delta l_\mathrm{D} + sx, \\ &l_{2,\mathrm{min}}^{\mathrm{c1}} = l_1 + (1.5 + \delta\Lambda)\delta l_\mathrm{D} + (1 + 0.5\delta\Lambda)sx, \\ &l_{2,\mathrm{min}}^{\mathrm{c3}} = l_{2,\mathrm{min}}^{\mathrm{c1}} + \mathbf{P}, \\ &\text{where } \mathbf{P} = \mathbf{C}^{-1}\left((\mathbf{A})\delta l_\mathrm{D} + (\mathbf{B})sx\right), \text{ and:} \\ &\mathbf{A} = {B'_\lambda}^2 + 8B'_\lambda - 1,\ \mathbf{B} = -4B'_\lambda\,(B'_\lambda - 2)\,,\ \mathbf{C} = 5{B'_\lambda}^2 - 6B'_\lambda + 1. \end{aligned} \tag{4.12}$$

By simple inspection, $l_{2,\mathrm{min}}^{\mathrm{n1}}$ is discarded. The remaining two conditions can be merged to get $l_{2,\mathrm{min}}$ as shown in what follows, so that the final value $l_2 = l_{2,\mathrm{min}} + \delta l_2$ is established. By introducing this expression into $l_{3,\mathrm{aux}}$ above, we similarly get a final value for $l_{3,\mathrm{min}}$, such that the final length is $l_3 = l_{3,\mathrm{min}} + \delta l_3$, being:

$$\begin{aligned} &l_{2,\mathrm{min}} = l_1 + (1.5 + \delta\Lambda)\delta l_\mathrm{D} + (1 + 0.5\delta\Lambda)sx + \Theta(\mathbf{P})\mathbf{P}, \\ &l_{3,\mathrm{min}} = l_1 + (5.5 + 3\delta\Lambda)\delta l_\mathrm{D} + (5 + 1.5\delta\Lambda)sx + 3\delta l_2 + 3\Theta(\mathbf{P})\mathbf{P}. \end{aligned} \tag{4.13}$$

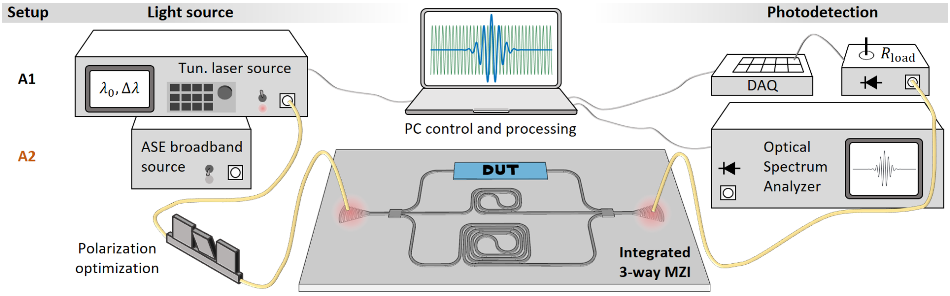

**Figure 4.8:** Sketch of the physical implementation of the technique: there are two different arrangements A1 and A2 for the light source and photodetection part. In the center, the integrated test structure, a 3-way MZI with the DUT in one of the arms, that is accessed by a single input and single output scheme.

where $\Theta$ is the Heaviside step function, which formally decides whether to use **c1** or **c3** for the determination of $l_{2,\mathrm{min}}$.

Therefore, we can summarize the design rules of the 3-MZI as follows:

- Consider the shortest possible DUT arm average length $L_1$, being the minimum and maximum involved lengths $l_1 \pm \delta l_\mathrm{D}/2$. Consider the wavelength conditions as well, through $\Lambda \equiv \Lambda_+/\Lambda_- = 1+\delta\Lambda$, being $\delta\Lambda = 2B'_\lambda/\left(1-B'_\lambda\right)$.
- $l_{2,\mathrm{min}} = l_1 + (1.5+\delta\Lambda)\,\delta l_\mathrm{D} + (1+0.5\delta\Lambda)\,sx + \Theta(\mathbf{P})\mathbf{P}$, so that we establish $l_2 = l_{2,\mathrm{min}} + \delta l_2$ in accordance with the tolerances of the real design.
- Finally, $l_{3,\mathrm{min}} = 3l_2 - 2l_1 + 2sx + \delta l_\mathrm{D}$,

where $\Theta$ is the Heaviside step function and the polynomial $\mathbf{P} = \mathbf{C}^{-1}\left((\mathbf{A})\delta l_\mathrm{D} + (\mathbf{B})sx\right)$, being $\mathbf{A} = {B'_\lambda}^2 + 8B'_\lambda - 1$, $\mathbf{B} = -4B'_\lambda\left(B'_\lambda - 2\right)$ and $\mathbf{C} = 5{B'_\lambda}^2 - 6B'_\lambda + 1$.

Since each impulsive contribution has a fundamental non-zero width due to the limited bandwidth (determining $\delta z_\mathrm{id}$, as explained above), the safety distance $sx$ should be chosen to be at least twice $\delta z_\mathrm{id}$ to prevent contributions overlapping. However in the real world, depending on the utilized wavelength scanning mechanism, there exists the possibility of some degree of nonlinearity on it. This turns into an added phase distortion in the super-interferogram that, similarly as it occurs with the aforementioned nonlinear frequency sampling, increases the broadening of the impulsive contributions. This effect should be characterize for the employed source in each particular experiment. We observed it and is covered in our experimental work in the following section.

### 4.3.4 Experimental results

The employed experimental setup is composed of the light source and photodetection parts, which together are in charge of performing a wavelength scanning for a given band. As shown in Fig. 4.8, we make use of two different approaches, part of a typical PIC characterization setup described in section 1.1, Fig. 1.2: on the one hand, arrangement A1 corresponds to the equipment that is customary in OFDI, a TL source performing the wavelength scanning and a photodetector plus a data acquisition card (DAQ) to digitize optical detected signal. For this setup, we employ already mentioned equipment (chapter 2, section 2.1), a Yenista TUNICS T100R/M providing 10 mW reliable source in the C-band (1490-1650 nm) with hop-free continuous scanning up to 100 nm/s, and Thorlabs FGA01FC InGaAs photodiodes mounted in a standard high impedance front-end without electronic amplification, providing an electrical voltage proportional to the optical intensity. This signal is digitized by the DAQ, a National Instruments USB-6259 ready to acquired 16-channel at 1 MS/s aggregated rate. On the other hand, we make use of an alternative approach A2, interesting since it makes use of other common laboratory equipment: it employs an ASE broadband source (NP Photonics C and L Band ASE, 19 dBm integrated power in the 1525-1610 nm band) and an OSA (Yokogawa AQ6370C, 0.02 nm resolution) in the photodetection part, which plays the wavelength scanning role. The OSA limited resolution is sufficient in this context thanks to the small PLDs which can be tailored in the integrated MZIs, giving rise to spectral FSRs easy to resolve. All this equipment corresponds to the typically used along this thesis, being customary OFDI A1 equipment specified in section 2.1.

### AWG in Silicon Nitride

Experimental validation of the technique is provided employing an AWG as a DUT. The AWG design is exactly the same as the one utilized in section 4.2 and is integrated on a chip fabricated on a later run of the same SiN technology platform, CNM-VLC [1]. In this occasion a $Si_3N_4$ waveguide layer of 280 nm height is deposited by LPCVD onto a 2.5 µm $SiO_2$ buffer, and again covered by a 2.0 µm $SiO_2$ cladding by PECVD (see [10] for CNM-VLC technology characterization). The single-mode waveguides employed for routing are quasi-rectangular 1 µm width designed for central wavelength $\lambda = 1550$ nm. Input/output light coupling to the chip is carried out by horizontal coupling making use of adiabatic tapers for better mode size matching. As for the AWG, it is 5 × 5 channel with 59 array waveguides and an FSR of 32 nm (4 THz), as shown in Fig. 4.9(a). The central input and output channels of the AWG are routed directly to input/output (left and right) facets of the chip (yellow arrows in the figure), aimed to be tested with external setup. A neighboring combination of input/output channels of the AWG is connected to the 3-MZI: light is coupled through one of the inputs (blue arrows at left), reaching a 50:50, 2 × 2 MMI that splits the signal in power. The upper output of the MMI is routed to the AWG and the bottom one is split again to feed the two delays lines implemented by spirals. All the paths are conveniently put together again by means of MMIs, so that the resulting beating signal is collected at one of the outputs. Not shown in Fig. 4.9(a) at the top is a similar 3-MZI device accessing the AWG with the complementary input/output channel

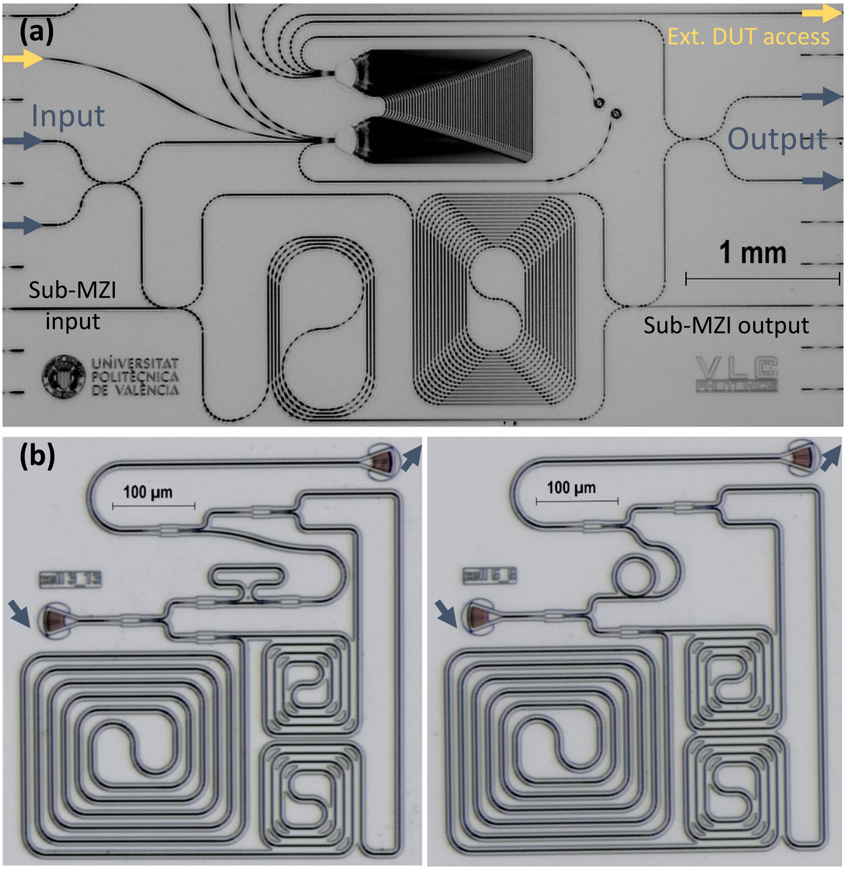

**Figure 4.9:** Microscopy picture of the fabricated 3-MZI test structures: (a) SiN with the AWG, and (b) SOI with MZI and RR, in left and right, respectively.

combination and with a different arrangement of the MMIs.

The different paths lengths of the 3-MZI are chosen to overtake the minimum requirements imposed by the design rules derived above. They are set considerably larger to minimize risk in this experimental analysis and validation. For the DUT arm, we have $l_1 = 6.756$ mm and $\delta l_\mathrm{D} \simeq 2.285$ mm. The experiment is planned to perform a wavelength scanning of $\Delta\lambda = 120$ nm centered at $\lambda_0 = 1550$ nm, and the waveguides are characterized by $n_{g,0} = 1.8245$ and $D = -1430$ ps/(nm km) [10]. The safety distance is chosen to be twice the ideal spatial resolution, $sx = 26.336$ µm. By applying the design rules detailed above, we get $l_{2,\mathrm{min}} = 10.589$ mm, but we make it longer such that $\delta l_2 = 6.206$ mm. This leaves a $l_{3,\mathrm{min}} = 39.211$ mm which again, we consider longer implying $\delta l_3 = 12.582$ mm. This lengths choice, that leaves $\Delta l \simeq 10.039$ mm and $\Delta l' \simeq 34.998$ mm, ensures the impulsive contributions isolation and Nyquist criterion proper application. Besides, it resembles similar PLD conditions as those for the first integrated OFDI in section 4.2. But, of course, shorter $l_2$ and $l_3$ may have been set, considerably reducing the spirals footprint.

Let us comment on a relevant remark regarding the different A1 and A2 setup arrangements, which involve two different wavelength scanning approaches: continuous TL sweep and OSA scanning, respectively. The effective wavelength conditions are $\Delta\lambda_\mathrm{A1} \simeq 109$ nm / $\lambda_{0,\mathrm{A1}} = 1550$ nm, and $\Delta\lambda_\mathrm{A2} \simeq 95$ nm / $\lambda_{0,\mathrm{A1}} = 1562.5$ nm, in such a way that the designed lengths are perfectly valid for both scenarios. In Fig. 4.10, the impulsive responses for A1 and A2 arrangements are shown from top to bottom, highlighting in green and blue the predefined crop regions for TRIG and DUT contributions, respectively, whose widths are calculated via Eq. 4.9. In the case of A2, the crop region perfectly covers the whole contributions of interest. However, in the case of A1 there is an offset between the region and the actual width of the contributions, which turns obvious when observing the TRIG. This entails an added phase distortion in the super-interferogram which is basically due to the presence of wavelength scanning nonlinearities. In A1 arrangement, it is unavoidable for a rapid TL continuous sweep to manifest some deviation from linearity in the scanning. This characteristic must be taken into account in the actual design when choosing the safety distance $sx$. Ideally, it would be enough to consider at least $sx = 2\delta z_\mathrm{id}$, to prevent overlapping of contributions. If it is the case though, it should be considered a larger $sx$ to leave room for the nonlinear wavelength scanning effect. The rigorous way to proceed includes the previous characterization of the wavelength scanning mechanism, in order to find out the average broadening associated to the introduced phase distortion.

The measurements of the 3-MZI test structure are performed with both A1 and A2 arrangements previously described and shown in Fig. 4.8. As done in section 4.2, the average group index can be retrieved from the OFDI measurements by computing the TRIG interferogram number of interferometric oscillations $N_\mathrm{osc}$ in the working band $\Delta\lambda$, using Eq. 4.3 and resulting in this case $n_{g,0} = 1.8245 \pm 0.0015$. Its value is slightly smaller in comparison to previous work waveguides but expected, since optical mode is less confined for some waveguide height reduction.

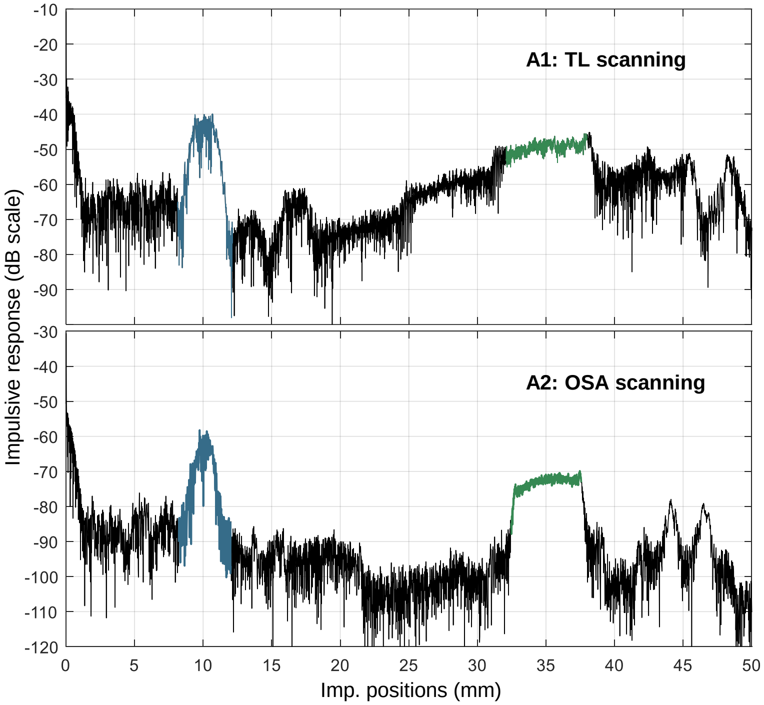

**Figure 4.10:** Impulsive domain responses of A1 and A2 arrangement setup measurements, at the top and bottom, respectively. In green and blue, the crop windows for TRIG and DUT contributions are emphasized.

In Fig. 4.11, a measurement performed with A1 setup and the corresponding pre-processing is shown. In (a), the obtained super-interferogram is shown in black curve for a sweep scanning of $\Delta\lambda = 109$ nm around $\lambda_0 = 1550$ nm. After applying the inverse FFT algorithm, the impulsive domain is obtained and its amplitude represented in (b), showing the expected symmetry with the DC contribution in the center and the different expected contributions around. Among them, the broadened contributions corresponding to the DUT (blue curve) and TRIG (green curve) interferograms are straightforwardly identified, then isolated by defining squared crop windows (i.e. filling with zeros everything else around) to finally, separately, apply FFT back to the frequency domain to recover the interferograms. In the inset, a zoom in the $\lambda = 1540$ nm region shows clearly how the structure of the super-interferogram is successfully decoupled into the two interferograms. Both DUT and TRIG interferograms appear at a lower level, with a marked symmetry around the $x$-axis: this is because the super-interferogram DC contribution is intentionally not included in the definition of the crop windows, along with any other contributions placed at different impulsive positions, resulting into smooth interferogram traces.

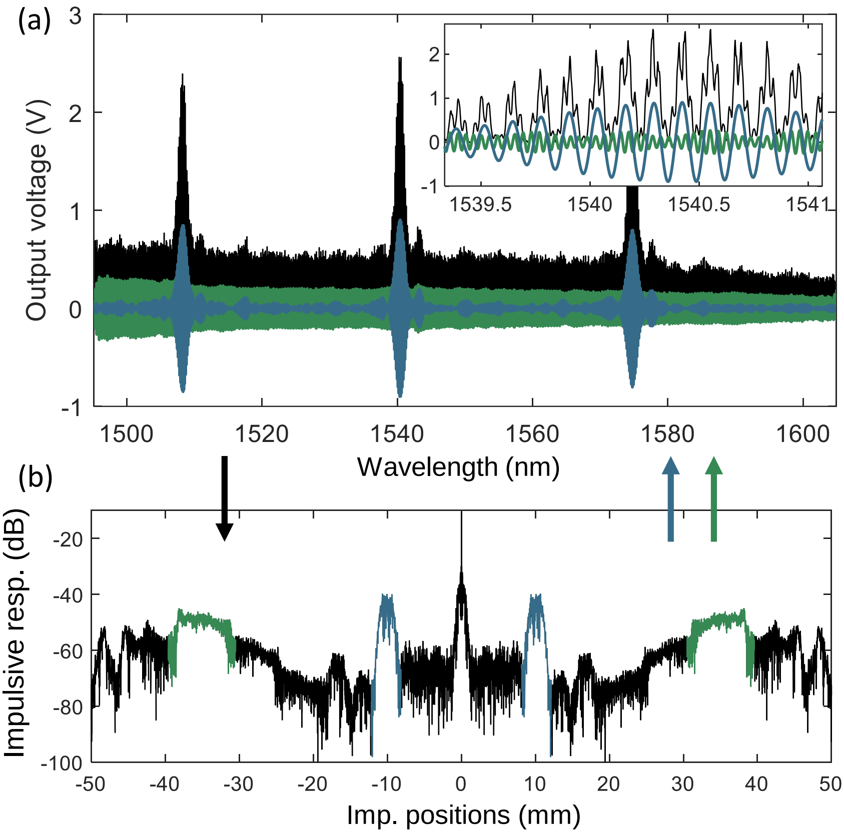

**Figure 4.11:** Super-interferogram processing to decouple DUT and REF interferograms. (a) In black line, the recorded super-interferogram and the recovered DUT and TRIG interferograms in blue and green lines, respectively. In the inset, a zoom around the $\lambda = 1540$ nm region. In (b), the obtained impulsive domain where the DUT and TRIG contributions are highlighted correspondingly.

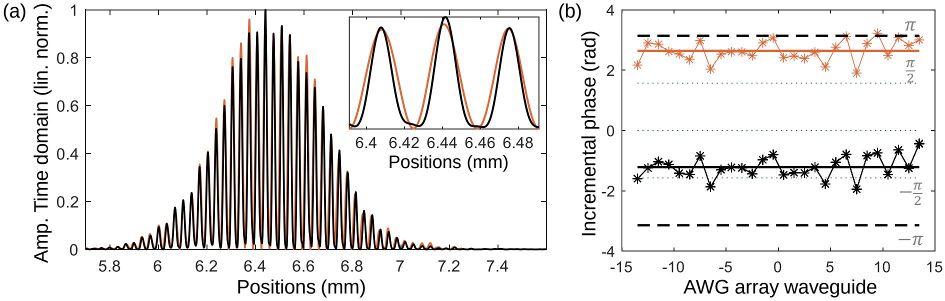

**Figure 4.12:** (a) Amplitude time domain response of the AWG, normalized in linear scale. A zoom in the inset shows the detail of the temporal contributions in the AWG central region. (b) Incremental optical phase between the 29 central waveguides of the AWG. In black line, the obtained trace with A1 arrangement, whereas the orange line corresponds to A2.

After OFDI processing of the obtained interferograms, the time domain response of the AWG is obtained and its amplitude is shown in Fig. 4.12(a), in black line. The $x$-axis is expressed in positions and it can be referred to as spatial domain too. Indeed, due to the dispersion de-embedding mechanism, the broadening of the temporal peaks, which is a temporal effect, is removed and thus it is strictly correct to refer to this picture as such. The train of consecutive peaks represents each path followed by light through the array waveguides, with an spacing which corresponds to the designed one $\delta l = 39.4$ µm. The expected Gaussian envelope as a consequence of the free space propagation in the AWG slabs is perfectly observed. A simple Gaussian fitting is applied to the peaks in order to get an estimation of the spatial resolution by computing the FWHM. By analyzing the 15 central contributions and average over 10 measurement takes, the obtained spatial resolution is $\delta z_{\mathrm{exp,A1}} = 12.6 \pm 0.2$ µm, which is pretty close the ideal one $\delta z_{\mathrm{id,A1}} = 12.1$ µm. The device is also measured employing A2 arrangement, for which the band $\Delta\lambda = 95$ nm centered at $\lambda_0 = 1562.5$ nm is considered. In this case, even though the ASE source presents a non-uniform spectral shape, the trace is normalized to the source by subtracting a reference measurement (i.e. propagation through a straight waveguide) to it. The obtained time domain amplitude is represented by an orange curve in Fig. 4.12(a), again reproducing the expected pattern. Same analysis of the peaks estimates $\delta z_{\mathrm{exp,A2}} = 16.5 \pm 0.8$ µm in this case, standing for the reduced bandwidth of the ASE source, for which the ideal spatial resolution is $\delta z_{\mathrm{id,A2}} = 14.1$ µm. In both A1 and A2 experiments, thanks to the dispersion de-embedding mechanism the obtained spatial resolution tends to the ideal one, permitting to directly observe and analyze nearby temporal contributions of the DUT, something which otherwise turns complicated, as demonstrated when measuring with an external OFDI system in section 4.2, due to the high chromatic dispersion of the integrated waveguides.

The time domain response provides also the phase response of the DUT. Apart from $\phi(\lambda)$, in practice the trace also contains an absolute phase component that varies from one take to another, which makes not straighforward to assess absolute optical phases. Nonetheless, as argued in section 2.3.2, that figure lacks of practical interest neither prevents to assess incremental phase between the different contributions inside one measurement take. In Fig. 4.12(b), the incremental phase between the 29 central contributions is shown for A1 and A2 arrangements, in black and orange lines, respectively. The averaged incremental phase over 10 takes in the case of A1 is around -1.21 rad with a standard deviation of 0.37 rad, while for A2 measurement is performed for one take and shows a great agreement with the former (standard deviation of 0.36 rad), observing some divergence only for the outer analyzed peaks of the AWG. The ideal functioning of the AWG relies on the generation of a linear phase response between the waveguides in the array, such that the incremental phase is a constant. The magnitude of the variations around this value is signature of the phase errors in the arrayed waveguides, and consequently the deviation from the ideal behaviour of the AWG which mainly manifests by the appearance of strong secondary lobes [19].

By applying FFT to the time domain response, the spectral response of the AWG is recovered and shown in Fig. 4.13 at the top, for the A1 and A2 arrangements (in black and orange line, respectively). Both traces coincide almost perfectly and show an AWG with a well-defined spectral response, presenting secondary lobes at about 15-20 dB below the main one, which in turn shows the expected shape. These traces are in perfect accordance with the external OSA take, shown at the bottom of the figure. Since this is measured by accessing the AWG throughout the external input/output combination (yellow arrows in Fig. 4.9(a)), a frequency shift is observed accordingly.

The drawn conclusions about the AWG in this case are in perfect agreement with what is observed for the integrated OFDI in section 4.2: in that case, the strong incremental phase measurements (deviation in the order of 3 rad) lead to the presence of strong secondary lobes in its spectrum. In the present case, probably due to some fabrication optimization, the AWG has an improved performance which is in accordance with the much lower incremental phase variation.

### RRs and MZIs in Silicon-On-Insulator

Some different 3-MZI test structure devices involving RRs and MZIs as DUTs were designed to be fabricated in Inphotech SOI technology platform [98], where the employed deep-etched cross-section is a rectangular waveguide of 480 nm width and 220 nm height designed to be single-mode at $\lambda = 1550$ nm, and patterned by electron beam lithography (EBL). In this technology, the expected propagation loss is $\alpha_{SOI} = 3$ dB/cm and the recommended minimum bending radius is around 10 µm. Due to the limited stitching area cells, characteristic of EBL, the design of the test structure units were optimized to stick to a small footprint of just $0.5 \times 0.5$ mm$^2$. In Fig. 4.9(b), two microscopy pictures of the test structure cells are shown, where chip optical input/output (blue arrows) is conducted vertically by the use of grating couplers (GC), the circuitry delay lines are implemented by

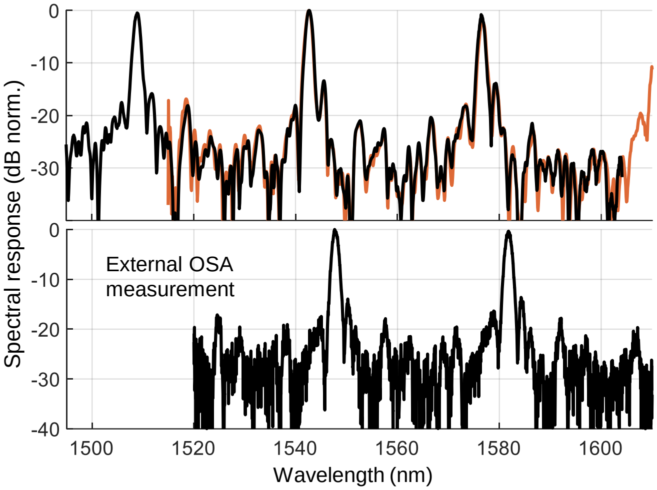

**Figure 4.13:** Spectrum of the AWG normalized in dB scale. At the top, the spectral reconstructions are shown in black and orange lines for A1 and A2 arrangement measurements, respectively. At the bottom, the spectral measurement of the AWG external input/output with OSA.

three spiral structures and the DUTs shown are a MZI with PLD equal to 200 μm in the picture at the left, and a RR at the right. The different paths are divided and joined where it is required by employing 1 × 2 MMIs.

The vertical coupling is of particular interest since it is indispensable for wafer scale testing of waveguides and devices, highly desired as it enables technology performance monitoring in intermediate steps of the PIC fabrication process. However, the GCs are TE mode filtering and have limited bandwidth. Since we are not implementing a polarization diversity characterization system, TE mode filtering does not entail an issue. Considering the limited bandwidth, as described in section 2.3.2, a processing step in the OFDI processing consists in applying an apodization window to the DUT interferogram in order to reduce secondary lobes of the peaks when switching to the time domain (at the cost of a reduced effective wavelength span, which in turn decreases the spatial resolution). The smoothly decaying fashion of the GC bandwidth curve can be considered as a partial implementation of the apodization window, so that it implements this processing step in a natural way. In the present case, the coupling efficiency presents a smooth Gaussian-like apodization window of about 45 nm centered at $\lambda_0 = 1570$ nm, so that we set up the TL to sweep $\Delta\lambda = 160$ nm around $\lambda_0$ in the measurements, in order to properly resolve this window.

An extremely important device to be utilized as DUT is the RR: these devices have been extensively utilized for a myriad of PIC applications. In general, the design of RRs is tricky because their performance involves delicate optical phenomena like evanescent coupling, birefringence or waveguide chromatic disper-

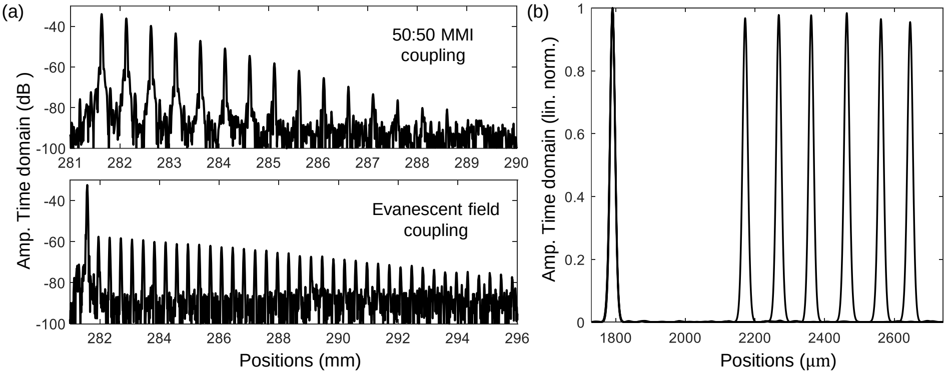

**Figure 4.14:** (a) Amplitude time domain response in dB scale of the measured RRs. The measurements are performed with external OFDI setup; for the 50:50 MMI coupled RR above, and for the evanescent coupled RR below. (b) Amplitude time domain response normalized in linear scale of the measured MZIs. The contributions correspond to the 6 different PLD cases, each of them composed of two peaks.

sion [76, 77]. Therefore, in order to optimize designs, a thorough characterization of these devices turns essential. Beyond, in the context of this thesis, RRs can be used as a test structure that, together with OFDI technique, provide a technology multi-parameter characterization platform (see section 3.2). The time domain response of the RR consists of a train of power decaying contributions corresponding to the light roundtrips in the RR, containing information about the RR coupling conditions, roundtrip loss and dispersion, and polarization effects such as, for instance, fundamental TE/TM mode coupling when using single-mode waveguides. Some RR models were included in the present SOI chip, both standalone and as DUT in 3-MZI structures. Unfortunately, the considerations about the DUT spatial width $\delta l$ (i.e. the number of resolvable roundtrips) turned out to be insufficient when setting the delay path lengths $l_2$ and $l_3$ in the 3-MZI structure, so overlapping of contributions in the impulsive domain and aliasing occurs. We have measured standalone RRs though with an external OFDI setup, and the resulting amplitude time domain response is shown in Fig. 4.14(a) for a RR coupled by 50:50 MMI with 150 μm roundtrip length at the top, and for an evanescent field coupled RR with 150 μm roundtrip length too, and a waveguide gap distance of 170 nm. The expected decaying power train of pulses is perfectly visualized in both cases. For the MMI coupled RR, up to 14 pulses are well-observed over the noise floor, with a constant slope (in dB scale) which includes the first-to-second peak power ratio, as expected when having $\kappa \simeq 0.5$ for the RR light coupling. In the case of the evanescent coupled RR, the first contribution is considerably more powerful standing for a weaker RR coupling, whereas a greater number of contributions with a flatter decay is visualized, signature of a higher Q factor RR. With the correct design, all this information can be also retrieved by the technique suggested in this manuscript.

Other DUTs which have been included to be tested in the 3-MZI test structures are MZIs. Specifically, 6 MZIs with different PLDs in the range $\Delta l = \{200, 250, ..., 450\}$ µm. The resulting amplitude time domain responses, after all the processing, are shown together in Fig. 4.14(b). The first peak at the left accumulates the different cases short arm of the MZI, whereas it can be perfectly checked how the separation of the remaining peaks increases by the designed step of 50 µm. In all the cases, the first peak is the one which carries more power while the second peak is slightly lowered. A subtle power decay can be noted between the peaks of the second group, standing for the accumulated propagation loss when the 50:50 performance of the MMIs can be assumed. As it happens with RRs, MZIs are very important devices diversely utilized in a broad range of applications in PICs, including in the context of characterization together with OFDI: as exposed in section 3.3.2, they can be used to design test structures which allows to obtain both waveguide properties (e.g. propagation loss and group index) and power splitting ratio of the used optical couplers. In the context of OFDI, MZIs and other type of interferometers can be also used to test active elements in a technology as, for example, thermal tuners (something that was not possible to implement in the present multi-project run). As shown for the AWG in SiN technology above, the incremental phase between different temporal contributions can be retrieved. In an interferometer, the increments of this calculated phase when tuning the active elements provide a mean to characterize the power needed to carry out a $\pi$-shift when a MZI is employed as an optical switch, or the thermal crosstalk when the active element is placed anywhere outside the device. This information may be retrieved from the FSR of a simple interferometer spectrum too, but the phase measurements with OFDI idea can be applied to test more complex devices such as, for example, tunable Sagnac loop interferometer based reflectors [85], as explained in section 3.4.

## 4.4 Conclusions

In this section, we have laid the foundations of what it may be considered the paradigm of this thesis, which is the merger of OFDI technique and integrated photonics. In these regards, we argued in the introduction which would be the possible functions of this combination. On the one hand, there is the possibility of considering an OFDI as an instrument in a compact integrated version. However, as we have discussed, this approach is not straightforward. Although not of easy implementation, integrated tunable lasers [99, 100] and photodetectors [101–103] are technologically a reality nowadays, and it would be mean a great leap forward in the miniaturization of an OFDI instrument. However, an OFDI instrument needs to be easily connectable to an arbitrary (integrated) DUT, an this is something difficult to conceive by any medium not being optical fiber. In consequence of the use of fiber pigtails, higher order of physical lengths are required to be compensated by integrated delay paths. Even if this compensation is passive (something that restricts the versatility of the system), the integrated waveguide high loss and footprint involved makes think to rule out this as a clever solution. It is this arbitrariness of the DUT and the instrument–DUT optical interconnect which makes this integrated OFDI conception as an instrument a difficult task, dubiously feasible at least in a short term.

What is quite more straightforward is the integration of the fully passive interferometric part, which leads to the conception of an integrated OFDI as a test structure. When the interferometric part is co-integrated with the DUT, some valuable advantages are found. The integrated waveguides provide compactness of the system and performance reliability as they are stable propagation media. Besides, they adapt to the integrated DUT dimensions and characteristics. This, on the one hand, allows to use OFDI technique for more limited wavelength resolution systems as the common laboratory equipment formed by a broadband ASE source in the C-band and an OSA performing the wavelength scanning. Furthermore, the presence of a TRIG-MZI in the integrated OFDI device enables an inherent dispersion de-embedding mechanism, allowing to keep the spatial resolution of the system to the ideal one (given by bandwidth $\Delta\lambda$), thus not requiring further post-processing needing to assume an approximated model to account for any degree of dispersion. In a first step, we justified all about this in [54]. Experimental proof is provided by testing an AWG in a SiN platform (section 4.2). We obtained the time domain response of the AWG and verified the dispersion de-embedding mechanism. Thanks to this, each temporal contribution is sufficiently isolated and, among other things, the accumulated phase between the waveguides in the array can be computed and identified as the error source of its behaviour in the spectral domain.

From a practical viewpoint, there is still a problem with the proposed integrated OFDI structure: this device has a single input, but two outputs have to be measured simultaneously. In this direction, we take one step forward in a second work [55] (section 4.3). A novel integrated test structure is proposed, a 3-way MZI holding the DUT in one of its arms, which generates a super-interferogram condensing all the necessary information to proceed with OFDI in a single input and single output measurement scheme. The same virtues are kept, at the cost of a bit more delicate design rules that are derived in detail, and a pre-processing step to decouple the OFDI interferograms. This consists of transforming the super-interferogram to its impulsive domain, where the contributions corresponding to the different 3-MZI path combinations appear at their impulsive positions. A set of non-overlapping conditions, together with sampling Nyquist criterion, give rise to the design rules of the 3-MZI arms lengths. Then, DUT and TRIG contributions can be isolated and transformed back to the frequency domain. A varied experimental validation of the technique is provided by testing an AWG in a SiN platform (same design and platform as in previous work) and MZIs in a SOI platform. In the case of the SOI platform, RRs were included as well but incorrectly designed, so OFDI measurements of the standalone RRs are measured and shown, as an example of what the technique could have allowed to resolve. The AWG measurements confirmed that the phase errors between waveguides in the array are, in this case, much lower, leading to a more ideal spectral response, due to some fabrication optimization. In SOI, it is remarkable the demonstration of the technique involving chip vertical coupling (by means of GCs) since it is the way to optically access the chip on a wafer-scale level. This scenario is much desired in the PIC community as it brings the opportunity to anticipate chip performance from critical fabrication steps, incorporating in-line photonic testing.

In the future, further refinements in the design of the 3-MZI might be considered. In the linearization part of the processing, we considered the common OFDI approach: the set of sampling points is given by the 'increasing' zeros of the TRIG interferogram sinusoid (those given by Eq. 2.12), 1 S/TRIG oscillation. Although it has not been taken into account during the design of these devices, as argued in the conclusions of chapter 2, this set is half of the available zeros, so there is room to double this number by including the 'decreasing' zeros as well, having 2 S/TRIG oscillation. Its implementation is straightforward in the processing and, when considered in the design, it involves a factor 1/2 in the Nyquist condition. This ultimately leads to more relaxed lengths of the delay paths ($l_2$ and $l_3$), resulting into shorter spirals and thus, better optical power conditions and a significant reduction of the test structure footprint. On the other hand, if several DUTs want to be tested, it can be considered to share delay paths between them. If it is the case of two DUTs and $2 \times 2$ MMIs has been employed for the MZIs, it can be used the MMI input left entering the delay sub-MZI (the sub-MZI input/output in Fig. 4.9(a)). In any other case, the use of optical switches turns required. The passive alternative to do this would be to connect the considered DUTs serially in the DUT path of the 3-MZI. However, although this would result into a half number of delay paths (when considering two DUTs), it is at the cost of being considerably longer to fulfill the design rules.

Beyond, even though optical circulators are non-reciprocal devices challenging to achieve in integrated chips (see [104] and references therein), we believe there is still the opportunity to do reflectometry with integrated OFDI and MZIs, by making use of $2 \times 2$ MMIs. The light enters the MMI through one input, reaches the device, and the reflected light comes back to the MMI, being its power shared between the two inputs (the one left can be used as the reflectometry output). In order to avoid this approach, an alternative would consist of doing without the MZI for the DUT interferometer, and employ Michelson-Morley, or even Fabry-Perot types. In theses cases, an integrated mirror of some kind must be employed for the reference paths though, either by taking advantadge of intra-chip reflections [41, 46, 47] or employing intended mirror devices [85, 105]. Nonetheless, the MZI approach allows to conceive a more complex device such as the one shown in Fig. 4.15, thought to test both the transmission and reflection transfer function of complex DUT made of Sagnac interferometer reflectors [86]. Without going into much detail, in this 3-MZI design both transmission and reflection responses are designed to be placed next to each other in the impulsive domain, so that the design of the device would be similar taking these two contributions as a whole DUT response. The 'unused' input of the MMI dividing DUT and reference arm paths in the DUT-MZI is in this case routed to the right part of the chip to be

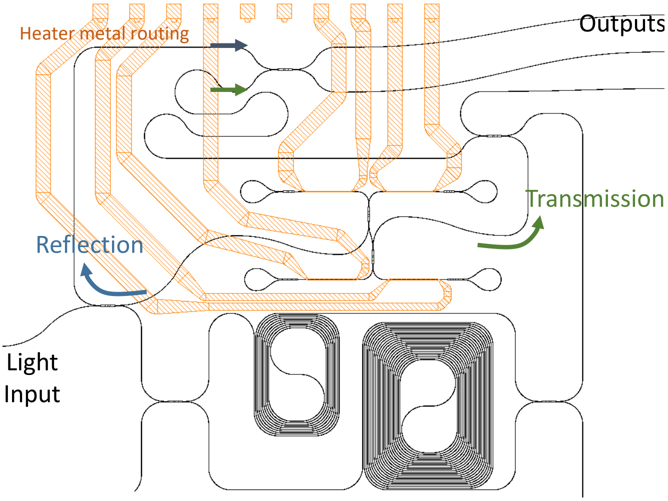

**Figure 4.15:** 3-MZI drawing design to test both reflection and transmission responses of a DUT, in this case a complex device made of reconfigurable mirrors.

joined with the rest of the paths.

Finally, the 3-MZI might be combined with applications based on OFDI which has been proposed in this thesis, in chapter 3, or any other, to obtain important parameters about a given technology. Furthermore, compact integrated test cells such as those in Fig. 4.9(b), remind the CMOS electronics test structures and may become their photonic counterparts. These are usually placed in the chip scribe line areas of the reticles, aimed at process step performance monitoring.

## Chapter 5

# Summary, conclusions and open research lines

## 5.1 Conclusions

The conclusions drawn from this PhD thesis work are summarized in what follows:

- Chapter 2: successfully, and after numerous tests, we built and mastered a working OFDI setup intended to explore its capabilities to interrogate photonic integrated devices. Although the associated casuistry is not straightforward to understand, the information that OFDI measurements are capable to deliver is highly valuable and have become a great quality step in our research group characterization laboratory. Apart from offering a landscape of the events taking place on the chip, the time domain contributions position, amplitude and phase can be related to deduce important parameters, giving rise to the applications developed in this thesis. Two of the principal light characteristics affecting OFDI measurements, dispersion and polarization, are analyzed in detail at the end of the chapter.

- Chapter 3: some of our first OFDI validations are covered, showing the potential of OFDI measurements. Afterwards, both existing and novel applications have been experimentally validated, using test structures designs to obtain important waveguide propagation and optical couplers parameters. With ring resonators (RR), thanks to the multiple temporal contributions corresponding to recirculations, statistics of group index and chromatic dispersion can be retrieved. These informations are obtained from position and phase of the temporal contributions, respectively, while optical coupler splitting ratio and RR roundtrip loss can be estimated from amplitude relations. Waveguide propagation loss can be inferred from reflectometric measurements of temporal decaying backscattering ramp slopes. Alternatively, we propose a test structure based on MZIs to obtain this parameter in a more robust way, along with optical coupler splitting ratio.

- Chapter 4: in the final part of the thesis, the co-integration of interferometric part of OFDI, implemented with integrated waveguides, with integrated DUTs is explored. Many advantages in terms of waveguides stability and adaptation to integrated DUTs are reasoned and experimentally validated. Amongst them, the capability to tailor small path length differences for the involved MZIs opens the door for less demanding external lab equipment, and a chromatic dispersion de-embedding mechanism is inherent to the use of integrated waveguides for the MZIs. The OFDI integration is envisaged as an advanced test structure, so that in a second work optimization of it is made through the introduction of a novel test structure with practical advantages, with an associated processing step, and with varied experimental work including different DUTs fabricated in different technologies, using alternative common lab equipment and both horizontal and vertical coupling to chip. This last point, compatible with wafer-scale testing, is of special interest in the PIC community since it brings the opportunity to test the chip performance from critical fabrication steps.

In the conclusions section of each chapter, further specific analysis is made.

## 5.2 Future work

After the work developed in this thesis, there are some open research lines that may be continued:

- Exploration of alternatives in the processing and analysis of the OFDI data.
- In the philosophy of a versatile implementation, validation of OFDI with less demanding laser sources and photodetection. For polarization setup control, solutions employing polarization maintaining fibers can be explored too.
- As detailed in the conclusions of chapter 3, to combine applications leading to more general purpose test structures.
- Integrated test structure refinements, to optimize (or even expand) its operation and easy implementation.

# Appendices

# Appendix A

# List of publications

During the thesis time, three SCI journal papers has been published with relation to the thesis work. Paper 1, a state-of-the-art review on Silicon Nitride strip waveguide photonic platforms, includes experimental technology characterization employing OFDI and techniques studied in this thesis. Paper 3, a more general review on Silicon Nitride photonics, includes some review on integrated OFDI structure as an application, which in turn is extensively covered in paper 2. The latter can be considered an exclusive of this thesis.

Regarding conferences, 18 works have been co-authored with some degree of relation to the thesis work. A group of them are technology characterization which makes use of OFDI. Others, are works related with the specific applications developed in this thesis.

## A.1 SCI Journal papers

1. P. Muñoz, G. Micó, L. A. Bru, D. Pastor, D. Pérez, J. D. Doménech, J. Fernández, R. Baños, B. Gargallo, R. Alemany, A. M. Sánchez, J. M. Cirera, R. Mas and C. Domínguez, “Silicon Nitride Photonc Integration Platforms for Visible, Near-Infrared and Mid-Infrared Applications,” *Sensors*, vol. 17, num. 2088, 2017.

2. L. A. Bru, D. Pastor and P. Muñoz, “Integrated optical frequency domain reflectometry device for characterization of complex integrated devices,” *Opt. Express*, vol. 26, num. 23, pp. 3000 – 3008, 2018.

3. P. Muñoz, P. W. L. van Dijk, D. Geuzebroek, M. Geiselmann, C. Domínguez, A. Stassen, J. D. Doménech, M. Zervas, A. Leinse, C. G. H. Roeloffzen, B. Gargallo, R. Baños, J. Fernández, G. Micó, L. A. Bru and D. Pastor, “Foundry Developments Toward Silicon Nitride Photonics From Visible to the Mid-Infrared,” *IEEE J. Sel. Top. Quantum Electron.*, vol. 25, num. 5, pp. 8200513, 2019.

4. L. A. Bru, D. Pastor and P. Muñoz, “Advanced and versatile interferometric technique for the characterization of photonic integrated devices,” *Opt. Express*, vol. 29, num. 22, pp. 36503 – 36515, 2021.

## A.2 Conference papers

1. L. A. Bru, B. Gargallo, G. Micó, R. Baños, J. D. Doménech, A. M. Sánchez, R. Mas, E. Pardo, D. Pastor and P. Muñoz, “Optical frequency domain reflectometry applied to photonic integrated circuits,” *18th European Conference on Integrated Optics (ECIO)*, p. o-08, Warsav, Poland, 18th – 20th May 2016.

2. P. Muñoz, G. Micó, L. A. Bru, D. Pastor and D. Doménech, “Linear and non-linear propagation properties of State of the art Silicon nitride waveguides,” *19th European Conference on Integrated Optics (ECIO)*, p. MP1.13, Eindhoven, The Netherlands, 3rd – 5th April 2017.

3. L. A. Bru, G. Micó, D. Pastor, D. Doménech, A. Sánchez, J. M. Cirera, J. Sánchez, C. Domínguez and P. Muñoz, “Full field Group Velocity Dispersion characterization of 300nm film height Silicon Nitride waveguides,” *19th European Conference on Integrated Optics (ECIO)*, p. MP1.4, Eindhoven, The Netherlands, 3rd – 5th April 2017.

4. G. Micó, L. A. Bru, D. Pastor, D. Pérez, J. D. Doménech, A. M. Sánchez, J. M. Cirera, J. Sánchez, C. Domínguez P. Muñoz,“C-band linear propagation characteristics for a 300 nm film height Silicon Nitride photonics platform” *19th European Conference on Integrated Optics (ECIO)*, p. T2.3, Eindhoven, The Netherlands, 3rd – 5th April 2017.

5. L. A. Bru, G. Micó, D. Pastor, B. Gargallo, D. Doménech, A. Sánchez, J. M. Cirera, J. Sánchez, C. Domínguez and P. Muñoz,“Fully Integrated Optical Frequency Domain Reflectometry” *19th European Conference on Integrated Optics (ECIO)*, p. M3.5, Eindhoven, The Netherlands, 3rd – 5th April 2017.

6. P. Muñoz, D. Doménech, C. Domínguez, A. Sánchez, G. Micó, L. A. Bru, D. Pérez and D. Pastor, “State of the Art of Silicon Nitride Photonics Integration Platforms,” *19th International Conference on Transparent Optical Networks (ICTON 2017)*, p. Tu.B5.3, Girona, Spain, 2nd – 6th July 2017.

7. L. A. Bru, G. Micó, D. Pastor, D. Pérez, D. Doménech, A. Sánchez, J. M. Cirera, J. Sánchez, C. Domínguez and P. Muñoz, “Linear propagation properties for a 300 nm film height Silicon Nitride photonic integration platform in the optical telecom C-band,” *in Advanced Photonics 2017 (IPR)*, p. IW2A.6, New Orleans, EE. UU., 24th – 27th July 2017.

8. G. Micó, L. A. Bru, D. Pastor, J. D. Doménech, J. Fernández, A. M. Sánchez, J. M. Cirera, C. Domínguez and P. Muñoz, “Silicon nitride photonics: from

visible to mid-infrared wavelengths," *SPIE Photonics West 2018 – Silicon Photonics XIII*, vol. 10537, pp. 33 – 41 San Francisco, California, United States, 27th January – 1st February 2018.

9. L. A. Bru and Z. Ye and D. Pastor and P. Muñoz,"Multi-parameter estimation of high-Q silicon rich nitride resonators using optical frequency domain reflectometry," *SPIE Photonics West 2018 – Integrated Optics: Devices, Materials, and Technologies XXII*, vol. 10535, pp. 148 – 155 San Francisco, California, United States, 27th January – 1st February 2018.

10. G. Micó, L. A. Bru, D. Pastor, D. Pérez, J. D. Doménech, J. Fernández, R. Baños, B. Gargallo, R. Alemany, A. M. Sánchez, J. M. Cirera, R. Mas, C. Domínguez P. Muñoz, "Silicon nitride photonic integration platform for visible, near-infrared and mid-infrared applications" *XIV European Conference on Optical Chemical Sensors and Biosensors (Europtrode XIV)*, Naples, Italy, 25th - 28th March, 2018.

11. L. A. Bru, D. Pastor, B. Gargallo, D. Doménech, C. Domínguez and P. Muñoz, "On-chip full-field test engine for photonic integrated devices based onoptical frequency domain reflectometry technique," *20th European Conference on Integrated Optics (ECIO)*, p. We.3.A.4, Valencia, Spain, 30th May – 1st June 2018.

12. G. Micó, L. A. Bru, D. Pastor, J. D. Doménech, A. M. Sánchez, C. Domínguez and P. Muñoz,"Impact of manufacturing processes on the optical amplitude, phase and polarization properties of silicon nitride waveguides" *20th European Conference on Integrated Optics (ECIO)*, p. P.26, Valencia, Spain, 30th May – 1st June 2018.

13. L. A. Bru, D. Pastor and P. Muñoz, "Integrated testing engine towards a complete characterization of complex photonic integrated devices," *XII Reunión Nacional de Óptica (RNO)*, Castellón, Spain, 3rd – 6th July 2018.

14. L. A. Bru, D. Pastor, B. Gargallo, D. Doménech, C. Domínguez and P. Muñoz, "Advanced Integrated Testing Engine towards a Complete Characterization of Photonic Integrated Devices," *44th European Conference on Optical Communication (ECOC 2018)*, pp. 1 – 3, Rome, Italy, 23rd – 27th September 2018.

15. L. A. Bru, D. Pastor and P. Muñoz, "On the characterization of integrated power splitters and waveguide losses using optical frequency domain interferometry," *21st European Conference on Integrated Optics (ECIO)*, p. W.Po1.25, Ghent, Belgium, 24th – 26th April 2019.

16. L. A. Bru, D. Pastor and P. Muñoz, "On the progress of advanced interferometric characterization of photonic integrated waveguides and devices," *XI Reunión Española de Optoelectrónica (OPTOEL 2019)*, p. SP3.MIC08, Zaragoza, Spain, 3rd – 5th July 2019.

17. J. Fernández, L. A. Bru, D. Pastor, D. Doménech, C. Domínguez and P. Muñoz, “Universal tunable integrated mirror: the Sagnac Loop Interferometer”, *XI Reunión Española de Optoelectrónica (OPTOEL 2019)*, p. SP3.MIC07, Zaragoza, Spain, 3rd – 5th July 2019.
18. J. Fernandez, L. A. Bru, D. Pastor, D. Domenech, C. Domínguez and P. Muñoz, “Sagnac Reflector Based Broadband Tunable Integrated Mirror,” *22nd International Conference on Transparent Optical Networks (ICTON)*, pp. 1-5, Bari, Italy, 19th – 23rd 2020.

# Bibliography

[1] "Centro nacional de microelectrónica (cnm) silicon nitride photonic integration platform, http://www.imb-cnm.csic.es/index.php/en/clean-room/silicon-nitride-technology."

[2] E. Hecht, *Optics (5h Edition)*. Pearson Eduaction, 2016.

[3] E. MILLER, "THE BELL TECHNICAL SYSTEM Integrated Optics : An Introduction," *THE BELL SYSTEM technical journal*, 1969.

[4] P. Muñoz, "Photonic integration in the palm of your hand: Generic technology and multi-project wafers, technical roadblocks, challenges and evolution," in *2017 Optical Fiber Communications Conference and Exhibition (OFC)*, pp. 1–3, 2017.

[5] R. Baets, A. Z. Subramanian, S. Clemmen, B. Kuyken, P. Bienstman, N. L. Thomas, G. Roelkens, D. V. Thourhout, P. Helin, and S. Severi, "Silicon photonics: silicon nitride versus silicon-on-insulator," in *Optical Fiber Communication Conference*, p. Th3J.1, Optical Society of America, 2016.

[6] A. Rahim, J. Goyvaerts, B. Szelag, J.-M. Fedeli, P. Absil, T. Aalto, M. Harjanne, C. Littlejohns, G. Reed, G. Winzer, S. Lischke, L. Zimmermann, D. Knoll, D. Geuzebroek, A. Leinse, M. Geiselmann, M. Zervas, H. Jans, A. Stassen, C. Domínguez, P. Muñoz, D. Domenech, A. L. Giesecke, M. C. Lemme, and R. Baets, "Open-access silicon photonics platforms in europe," *IEEE Journal of Selected Topics in Quantum Electronics*, vol. 25, no. 5, pp. 1–18, 2019.

[7] A. E.-J. Lim, J. Song, Q. Fang, C. Li, X. Tu, N. Duan, K. K. Chen, R. P.-C. Tern, and T.-Y. Liow, "Review of silicon photonics foundry efforts," *IEEE Journal of Selected Topics in Quantum Electronics*, vol. 20, no. 4, pp. 405–416, 2014.

[8] S. Y. Siew, B. Li, F. Gao, H. Y. Zheng, W. Zhang, P. Guo, S. W. Xie, A. Song, B. Dong, L. W. Luo, C. Li, X. Luo, and G.-Q. Lo, "Review of sili-

con photonics technology and platform development," *Journal of Lightwave Technology*, vol. 39, no. 13, pp. 4374–4389, 2021.

[9] T. Sharma, J. Wang, B. K. Kaushik, Z. Cheng, R. Kumar, Z. Wei, and X. Li, "Review of recent progress on silicon nitride-based photonic integrated circuits," *IEEE Access*, vol. 8, pp. 195436–195446, 2020.

[10] P. Muñoz, G. Micó, L. A. Bru, D. Pastor, D. Pérez, J. D. Doménech, J. Fernández, R. Baños, B. Gargallo, R. Alemany, A. M. Sánchez, J. M. Cirera, R. Mas, and C. Domínguez, "Silicon nitride photonic integration platforms for visible, near-infrared and mid-infrared applications," *Sensors*, vol. 17, no. 9, p. 2088, 2017.

[11] G. Micó, *Integrated spectroscopic sensor fabricated in a novel $Si_3N_4$ platform.* phdthesis, Universitat Politècnica de València, Valencia, July 2020.

[12] J. Klamkin, H. Zhao, B. Song, Y. Liu, B. Isaac, S. Pinna, F. Sang, and L. Coldren, "Indium phosphide photonic integrated circuits: Technology and applications," in *2018 IEEE BiCMOS and Compound Semiconductor Integrated Circuits and Technology Symposium (BCICTS)*, pp. 8–13, 2018.

[13] M. J. R. Heck, J. F. Bauters, M. L. Davenport, J. K. Doylend, S. Jain, G. Kurczveil, S. Srinivasan, Y. Tang, and J. E. Bowers, "Hybrid silicon photonic integrated circuit technology," *IEEE Journal of Selected Topics in Quantum Electronics*, vol. 19, pp. 6100117–6100117, July 2013.

[14] J. Fernández, R. Baños, D. Doménech, C. Domínguez, and P. Muñoz, "Low-loss inverted taper edge coupler in silicon nitride," *IET Optoelectronics*, vol. 13, no. 2, pp. 62–66, 2019.

[15] Y. Xu, Y. Li, R. K. Lee, and A. Yariv, "Scattering-theory analysis of waveguide-resonator coupling," *Phys. Rev. E*, vol. 62, pp. 7389–7404, Nov 2000.

[16] S.-Y. Cho and R. Soref, "Apodized scissors for filtering and switching," *Opt. Express*, vol. 16, pp. 19078–19090, Nov 2008.

[17] M. Smit, "New focusing and dispersive planar component based on an optical phased array," *Electronics Letters*, vol. 24, pp. 385–386(1), March 1988.

[18] M. Smit and C. Van Dam, "Phasar-based wdm-devices: Principles, design and applications," *IEEE Journal of Selected Topics in Quantum Electronics*, vol. 2, no. 2, pp. 236–250, 1996.

[19] P. Munoz, D. Pastor, J. Capmany, and S. Sales, "Analytical and numerical analysis of phase and amplitude errors in the performance of arrayed waveguide gratings," *IEEE Journal of Selected Topics in Quantum Electronics*, vol. 8, pp. 1130–1141, Nov 2002.

[20] P. Munoz, D. Pastor, and J. Capmany, “Modeling and design of arrayed waveguide gratings,” *Journal of Lightwave Technology*, vol. 20, no. 4, pp. 661–674, 2002.

[21] S. Janz, A. Balakrishnan, S. Charbonneau, P. Cheben, M. Cloutier, A. Delage, K. Dossou, L. Erickson, M. Gao, P. Krug, B. Lamontagne, M. Packirisamy, M. Pearson, and D.-X. Xu, “Planar waveguide echelle gratings in silica-on-silicon,” *IEEE Photonics Technology Letters*, vol. 16, no. 2, pp. 503–505, 2004.

[22] J. Brouckaert, W. Bogaerts, P. Dumon, D. Van Thourhout, and R. Baets, “Planar concave grating demultiplexer fabricated on a nanophotonic silicon-on-insulator platform,” *Journal of Lightwave Technology*, vol. 25, no. 5, pp. 1269–1275, 2007.

[23] D. Melati, P. G. Verly, A. Delâge, S. Wang, J. Lapointe, P. Cheben, J. H. Schmid, S. Janz, and D.-X. Xu, “Compact and low crosstalk echelle grating demultiplexer on silicon-on-insulator technology,” *Electronics*, vol. 8, no. 6, 2019.

[24] D. Pérez, J. Fernández, R. Baños, J. D. Doménech, A. M. Sánchez, J. M. Cirera, R. Mas, J. Sánchez, S. Durán, E. Pardo, C. Domínguez, D. Pastor, J. Capmany, and P. Muñoz, “Thermal tuners on a silicon nitride platform,” 2016.

[25] R. Alemany, P. Muñoz, D. Pastor, and C. Domínguez, “Thermo-optic phase tuners analysis and design for process modules on a silicon nitride platform,” *Photonics*, vol. 8, no. 11, 2021.

[26] W. Bogaerts, D. Pérez, J. Capmany, D. A. B. Miller, J. Poon, D. Englund, F. Morichetti, and A. Melloni, “Programmable photonic circuits,” *Nature*, vol. 586, pp. 207–216, 2020.

[27] A. A. Michelson and E. W. Morley, “On the relative motion of the earth and the luminiferous ether,” *American Journal of Science*, vol. s3-34, no. 203, pp. 333–345, 1887.

[28] B. P. Abbott, “Observation of gravitational waves from a binary black hole merger,” *Phys. Rev. Lett.*, vol. 116, p. 061102, Feb 2016.

[29] X. Bao, W. Li, Z. Qin, and L. Chen, “OTDR and OFDR for distributed multi-parameter sensing,” in *Smart Sensor Phenomena, Technology, Networks, and Systems Integration 2014* (W. Ecke, K. J. Peters, N. G. Meyendorf, and T. E. Matikas, eds.), vol. 9062, pp. 1 – 11, International Society for Optics and Photonics, SPIE, 2014.

[30] K. Yuksel, M. Wuilpart, V. Moeyaert, and P. Megret, “Optical frequency domain reflectometry: A review,” in *2009 11th International Conference on Transparent Optical Networks*, pp. 1–5, 2009.

[31] P. Healey, R. Booth, B. Daymond-John, and B. Nayar, “Otdr in single-mode fibre at 1.5 µm using homodyne detection,” *Electronics Letters*, vol. 20, pp. 360–362(2), April 1984.

[32] S. Stopiński, K. Anders, S. Szostak, and R. Piramidowicz, “Optical time domain reflectometer based on application specific photonic integrated circuit,” in *2019 Conference on Lasers and Electro-Optics Europe European Quantum Electronics Conference (CLEO/Europe-EQEC)*, pp. 1–1, 2019.

[33] R. Zinsou, X. Liu, Y. Wang, J. Zhang, Y. Wang, and B. Jin, “Recent progress in the performance enhancement of phase-sensitive otdr vibration sensing systems,” *Sensors*, vol. 19, no. 7, 2019.

[34] A. F. Fercher, W. Drexler, C. K. Hitzenberger, and T. Lasser, “Optical coherence tomography - principles and applications,” *Reports on Progress in Physics*, vol. 66, pp. 239–303, jan 2003.

[35] D. Derickson, *Fiber optics test and measurement.* Prentice Hall, 1998.

[36] W. Eickhoff and R. Ulrich, “Optical frequency domain reflectometry in single-mode fiber,” *Applied Physics Letters*, vol. 39, no. 9, pp. 693–695, 1981.

[37] U. Glombitza and E. Brinkmeyer, “Coherent frequency-domain reflectometry for characterization of single-mode integrated-optical waveguides,” *Journal of Lightwave Technology*, vol. 11, pp. 1377–1384, Aug 1993.

[38] M. Froggatt, *Intracore and extracore examination of fiber gratings with coherent detection.* phdthesis, University of Rochester. Institute of Optics, Rochester, N.Y., 2001.

[39] B. J. Soller, D. K. Gifford, M. S. Wolfe, and M. E. Froggatt, “High resolution optical frequency domain reflectometry for characterization of components and assemblies,” *Opt. Express*, vol. 13, pp. 666–674, Jan 2005.

[40] “Luna technologies inc., optical vector analyzer ova 5100: `https://lunainc.com/product/ova-5100`,” 2019 - 2021.

[41] F. Morichetti, A. Canciamilla, C. Ferrari, M. Torregiani, A. Melloni, and M. Martinelli, “Roughness induced backscattering in optical silicon waveguides,” *Phys. Rev. Lett.*, vol. 104, p. 033902, Jan. 2010.

[42] J. F. Bauters, M. J. R. Heck, D. D. John, J. S. Barton, C. M. Bruinink, A. Leinse, R. G. Heideman, D. J. Blumenthal, and J. E. Bowers, “Planar waveguides with less than 0.1 db/m propagation loss fabricated with wafer bonding,” *Opt. Express*, vol. 19, pp. 24090–24101, Nov 2011.

[43] E. J. Stanton, N. Volet, and J. E. Bowers, “Low-loss demonstration and refined characterization of silicon arrayed waveguide gratings in the near-infrared,” *Opt. Express*, vol. 25, pp. 30651–30663, Nov 2017.

[44] M. A. Tran, D. Huang, T. Komljenovic, J. Peters, A. Malik, and J. E. Bowers, "Ultra-low-loss silicon waveguides for heterogeneously integrated silicon/iii-v photonics," *Applied Sciences*, vol. 8, no. 7, 2018.

[45] R. Halir, I. Molina-Fernández, J. Wangüemert-Pérez, A. O.-M. nux, J. de Oliva-Rubio, and P. Cheben, "Characterization of integrated photonic devices with minimum phase technique," *Opt. Express*, vol. 17, pp. 8349–8361, May 2009.

[46] D. Melati, A. Alippi, and A. Melloni, "Waveguide-based technique for wafer-level measurement of phase and group effective refractive indices," *J. Lightwave Technol.*, vol. 34, pp. 1293–1299, Feb 2016.

[47] D. Zhao, D. Pustakhod, K. Williams, and X. Leijtens, "High resolution optical frequency domain reflectometry for analyzing intra-chip reflections," *IEEE Photonics Technology Letters*, vol. 29, pp. 1379–1382, Aug 2017.

[48] M. Theurer, M. Moehrle, A. Sigmund, K.-O. Velthaus, R. M. Oldenbeuving, L. Wevers, F. M. Postma, R. Mateman, F. Schreuder, D. Geskus, K. Wörhoff, R. Dekker, R. G. Heideman, and M. Schell, "Flip-chip integration of inp to sin photonic integrated circuits," *Journal of Lightwave Technology*, vol. 38, no. 9, pp. 2630–2636, 2020.

[49] K. Twayana, Z. Ye, Óskar B. Helgason, K. Vijayan, M. Karlsson, and V. Torres-Company, "Frequency-comb-calibrated swept-wavelength interferometry," *Opt. Express*, vol. 29, pp. 24363–24372, Jul 2021.

[50] M. Tokushima and J. Ushida, "Demonstration of in-depth analysis of silicon photonics circuits using ofdr: waveguides with grating couplers," *Opt. Lett.*, vol. 47, pp. 162–165, Jan 2022.

[51] L. A. Bru, G. Micó, D. Pastor, D. Doménech, A. Sánchez, J. M. Cirera, J. Sánchez, C. Domínguez, and P. Muñoz, "Full field group velocity dispersion characterization of 300nm film height silicon nitride waveguides," in *19th European Conference on Integrated Optics (ECIO)*, (Eindhoven, The Netherlands), p. MP1.4, 3–5 April 2017.

[52] L. A. Bru, Z. Ye, D. Pastor, and P. Muñoz, "Multi-parameter estimation of high-Q silicon rich nitride resonators using optical frequency domain reflectometry," in *Integrated Optics: Devices, Materials, and Technologies XXII*, vol. 10535, pp. 148 – 155, International Society for Optics and Photonics, SPIE, 2018.

[53] L. A. Bru, D. Pastor, and P. Muñoz, "On the characterization of integrated power splitters and waveguide losses using optical frequency domain interferometry," in *21st European Conference on Integrated Optics (ECIO)*, (Ghent, Belgium), p. W.Po1.25, 24–26 April 2019.

[54] L. A. Bru, D. Pastor, and P. Muñoz, “Integrated optical frequency domain reflectometry device for characterization of complex integrated devices,” *Opt. Express*, vol. 26, pp. 30000–30008, Nov 2018.

[55] L. A. Bru, D. Pastor, and P. Muñoz, “Advanced and versatile interferometric technique for the characterization of photonic integrated devices,” *Opt. Express*, vol. 29, pp. 36503–36515, Oct 2021.

[56] W. Eickhoff and R. Ulrich, “Optical frequency-domain reflectometry in single-mode fibers,” in *Integrated Optics and Optical Fiber Communication*, p. WF3, Optical Society of America, 1981.

[57] A. Liu, P. Wolf, J. A. Lott, and D. Bimberg, “Vertical-cavity surface-emitting lasers for data communication and sensing,” *Photon. Res.*, vol. 7, pp. 121–136, Feb 2019.

[58] “Thorlabs ingaas high-speed photodiode fga01fc, `https://www.thorlabs.com/thorproduct.cfm?partnumber=FGA01FC`.”

[59] H. Haus, W. Huang, S. Kawakami, and N. Whitaker, “Coupled-mode theory of optical waveguides,” *Journal of Lightwave Technology*, vol. 5, no. 1, pp. 16–23, 1987.

[60] W.-P. Huang, “Coupled-mode theory for optical waveguides: an overview,” *J. Opt. Soc. Am. A*, vol. 11, pp. 963–983, Mar 1994.

[61] E. H. . R. E. Hewitt, “The gibbs-wilbraham phenomenon: An episode in fourier analysis,” *Archive for History of Exact Sciences*, vol. 21, pp. 129–160, 1979.

[62] C. Caló, B. Robillart, Y. Gottesman, A. Fall, F. Lamare, K. Merghem, A. Martinez, A. Ramdane, and B. Bcnkelfat, “Spectral and temporal phase measurement by optical frequency-domain reflectometry,” in *26th International Conference on Indium Phosphide and Related Materials (IPRM)*, pp. 1–2, May 2014.

[63] P. Drexler and P. Fiala, *Recent Progress in Optical Fiber Research*, ch. Optical Fiber Birefringence Effects – Sources, Utilization and Methods of Suppression, pp. 127 – 150. InTech, Jan. 2012.

[64] D. K. Gifford, B. J. Soller, M. S. Wolfe, and M. E. Froggatt, “Optical vector network analyzer for single-scan measurements of loss, group delay, and polarization mode dispersion,” *Appl. Opt.*, vol. 44, pp. 7282–7286, Dec 2005.

[65] T.-J. Ahn, J. Y. Lee, and D. Y. Kim, “Suppression of nonlinear frequency sweep in an optical frequency-domain reflectometer by use of hilbert transformation,” *Appl. Opt.*, vol. 44, pp. 7630–7634, Dec 2005.

[66] B. A. Gargallo, *Advanced Arrayed Waveguide Gratings: Models, design strategies and experimental demonstration.* phdthesis, Universitat Politècnica de València, Valencia, July 2016.

[67] L. A. Bru, B. Gargallo, G. Micó, R. Baños, J. D. Doménech, A. M. Sánchez, R. Mas, E. Pardo, D. Pastor, and P. Muñoz, "Optical frequency domain reflectometry applied to photonic integrated circuits," in *18th European Conference on Integrated Optics (ECIO)*, (Warsav), pp. o–08, 18–20 May 2016.

[68] G. Micó, L. A. Bru, D. Pastor, D. Doménech, J. Fernández, A. Sánchez, J. M. Cirera, C. Domínguez, and P. Muñoz, "Silicon nitride photonics: from visible to mid-infrared wavelengths," in *Silicon Photonics XIII* (G. T. Reed and A. P. Knights, eds.), vol. 10537, pp. 33 – 41, International Society for Optics and Photonics, SPIE, 2018.

[69] "Research & development agreement ybn2018115377. photonic integrated fmcw lidar. funded by: Huawei tecnologies canada co., ltd.," 2019 - 2021.

[70] "Fraunhofer institute for telecomunications, heinrich hertz institue (hhi) inp foundry, `https://www.hhi.fraunhofer.de/en/departments/pc/research-groups/photonic-inp-foundry.html`."

[71] B. Gargallo, P. M. noz, R. B. nos, A. L. Giesecke, J. Bolten, T. Wahlbrink, and H. Kleinjans, "Reflective arrayed waveguide gratings based on sagnac loop reflectors with custom spectral response," *Opt. Express*, vol. 22, pp. 14348–14362, Jun 2014.

[72] J. S. Levy, A. Gondarenko, M. A. Foster, A. C. Turner-Foster, A. L. Gaeta, and M. Lipson, "Cmos-compatible multiple-wavelength oscillator for on-chip optical interconnects," *Nature Photonics*, vol. 4, pp. 37–40, 2010.

[73] S. B. Papp, K. Beha, P. Del'Haye, F. Quinlan, H. Lee, K. J. Vahala, and S. A. Diddams, "Microresonator frequency comb optical clock," *Optica*, vol. 1, no. 1, pp. 10–14, 2014.

[74] J. Zhu, S. K. Ozdemir, Y.-F. Xiao, L. Li, L. He, D.-R. Chen, and L. Yang, "On-chip single nanoparticle detection and sizing by mode splitting in an ultrahigh-q microresonator," *Nature Photonics*, vol. 4, p. 46, 2009.

[75] "Nanofabrication laboratory, department of microtechnology and nanoscience (mc2) at chalmers university `https://www.chalmers.se/en/researchinfrastructure/NFL/Pages/default.aspx`."

[76] W. Bogaerts, P. De Heyn, T. Van Vaerenbergh, K. De Vos, S. Kumar Selvaraja, T. Claes, P. Dumon, P. Bienstman, D. Van Thourhout, and R. Baets, "Silicon microring resonators," *Laser & Photonics Reviews*, vol. 6, no. 1, pp. 47–73, 2012.

[77] D. G. Rabus, *Ring Resonators: Theory and Modeling*, ch. 2, pp. 3–40. Springer Berlin Heidelberg, 2007.

[78] C. K. Madsen and J. H. Zhao, *Optical Filter Design and Analysis: A Signal Processing Approach.* John Wiley & Sons, Inc., 1999.

[79] C. J. Krückel, A. Fülöp, T. Klintberg, J. Bengtsson, P. A. Andrekson, and V. Torres-Company, "Linear and nonlinear characterization of low-stress high-confinement silicon-rich nitride waveguides," *Opt. Express*, vol. 23, pp. 25827–25837, Oct 2015.

[80] F. Ladouceur and L. Poladian, "Surface roughness and backscattering," *Opt. Lett.*, vol. 21, pp. 1833–1835, Nov 1996.

[81] F. Morichetti, A. Canciamilla, and A. Melloni, "Statistics of backscattering in optical waveguides," *Opt. Lett.*, vol. 35, pp. 1777–1779, Jun 2010.

[82] T. Feuchter and C. Thirstrup, "High precision planar waveguide propagation loss measurement technique using a fabry-perot cavity," *IEEE Photonics Technology Letters*, vol. 6, no. 10, pp. 1244–1247, 1994.

[83] Z. Sheng, Z. Wang, C. Qiu, L. Li, A. Pang, A. Wu, X. Wang, S. Zou, and F. Gan, "A compact and low-loss mmi coupler fabricated with cmos technology," *IEEE Photonics Journal*, vol. 4, no. 6, pp. 2272–2277, 2012.

[84] M. A. Tran, T. Komljenovic, J. C. Hulme, M. L. Davenport, and J. E. Bowers, "A robust method for characterization of optical waveguides and couplers," *IEEE Photonics Technology Letters*, vol. 28, no. 14, pp. 1517–1520, 2016.

[85] J. Fernández, L. A. Bru, D. Pastor, D. Doménech, C. Domínguez, and P. Muñoz, "Universal tunable integrated mirror: the sagnac loop interferometer," in *XI Reunión Española de Optoelectrónica (OPTOEL)*, pp. 1–3, Sep. 2019.

[86] J. Fernandez, L. A. Bru, D. Pastor, D. Domenech, C. Domínguez, and P. Muñoz, "Sagnac reflector based broadband tunable integrated mirror," in *2020 22nd International Conference on Transparent Optical Networks (ICTON)*, pp. 1–5, 2020.

[87] S. Dwivedi, T. V. Vaerenbergh, A. Ruocco, T. Spuesens, P. Bienstman, P. Dumon, and W. Bogaerts, "Measurements of effective refractive index of soi waveguides using interferometers," in *Advanced Photonics 2015*, p. IM2A.6, Optical Society of America, 2015.

[88] X. Wang, Y. Zhao, Y. Ding, S. Xiao, and J. Dong, "Tunable optical delay line based on integrated grating-assisted contradirectional couplers," *Photon. Res.*, vol. 6, pp. 880–886, Sep 2018.

[89] D. Pérez-López, E. Sánchez, and J. Capmany, "Programmable true time delay lines using integrated waveguide meshes," *Journal of Lightwave Technology*, vol. 36, no. 19, pp. 4591–4601, 2018.

[90] S. G. Hailu and S.-L. Lee, "Tunable optical delay line based on a racetrack resonator with tunable coupling and stable wavelength," *Applied Sciences*, vol. 9, no. 24, 2019.

[91] D. Melati, A. Waqas, Z. Mushtaq, and A. Melloni, "Wideband integrated optical delay line based on a continuously tunable mach–zehnder interferometer," *IEEE Journal of Selected Topics in Quantum Electronics*, vol. 24, no. 1, pp. 1–8, 2018.

[92] Y. A. Vlasov, M. O'Boyle, H. F. Hamann, and S. J. McNab, "Active control of slow light on a chip with photonic crystal waveguides," *Nature*, vol. 438, no. 3, pp. 65–69, 2005.

[93] P. M. noz, D. Pastor, J. Capmany, D. Ortega, A. Pujol, and J. R. Bonar, "Awg model validation through measurement of fabricated devices," *J. Lightwave Technol.*, vol. 22, p. 2763, Dec 2004.

[94] B. Robillart, C. Calò, A. Fall, F. Lamare, Y. Gottesman, and B.-E. Benkelfat, "Spectral and temporal phase measurement by optical frequency-domain reflectometry," in *Fiber Lasers XI: Technology, Systems, and Applications* (S. Ramachandran, ed.), vol. 8961, pp. 581 – 591, International Society for Optics and Photonics, SPIE, 2014.

[95] L. A. Bru, D. Pastor, B. Gargallo, D. Doménech, C. Domínguez, and P. Muñoz, "Advanced integrated testing engine towards a complete characterization of photonic integrated devices," in *20th European Conference on Integrated Optics (ECIO)*, (Valencia), p. We.3.A.4, 30 May–1 June 2018.

[96] L. A. Bru, D. Pastor, B. Gargallo, D. Doménech, C. Domínguez, and P. Muñoz, "Advanced integrated testing engine towards a complete characterization of photonic integrated devices," in *2018 European Conference on Optical Communication (ECOC)*, p. SP3.MIC07, July 2018.

[97] L. A. Bru, D. Pastor, and P. Muñoz, "Integrated testing engine towards a complete characterization of complex photonic integrated devices," in *XII Reunión Nacional de Óptica (RNO)*, (Castellón), 3 – 6 July 2018.

[98] "Inphotec silicon-on-insulator photonic integration platform, `https://www.inphotec.it/technology_post_type/silicon-photonics-2/`."

[99] A. Hänsel and M. J. R. Heck, "Widely tunable laser on an inp photonic integrated circuit," *IEEE Photonics Technology Letters*, vol. 32, no. 2, pp. 105–108, 2020.

[100] A. Malik, C. Xiang, L. Chang, W. Jin, J. Guo, M. Tran, and J. Bowers, "Low noise, tunable silicon photonic lasers," *Applied Physics Reviews*, vol. 8, no. 3, p. 031306, 2021.

[101] M. Piels and J. E. Bowers, "1 - photodetectors for silicon photonic integrated circuits," in *Photodetectors* (B. Nabet, ed.), pp. 3–20, Woodhead Publishing, 2016.

[102] Q. Yu, J. Gao, N. Ye, B. Chen, K. Sun, L. Xie, K. Srinivasan, M. Zervas, G. Navickaite, M. Geiselmann, and A. Beling, "Heterogeneous photodiodes on silicon nitride waveguides," *Opt. Express*, vol. 28, pp. 14824–14830, May 2020.

[103] H.-G. Bach, A. Beling, G. Mekonnen, R. Kunkel, D. Schmidt, W. Ebert, A. Seeger, M. Stollberg, and W. Schlaak, "Inp-based waveguide-integrated photodetector with 100-ghz bandwidth," *IEEE Journal of Selected Topics in Quantum Electronics*, vol. 10, no. 4, pp. 668–672, 2004.

[104] D. Huang, P. Pintus, C. Zhang, P. Morton, Y. Shoji, T. Mizumoto, and J. E. Bowers, "Dynamically reconfigurable integrated optical circulators," *Optica*, vol. 4, pp. 23–30, Jan 2017.

[105] Y. Wang, S. Gao, K. Wang, H. Li, and E. Skafidas, "Ultra-broadband, compact, and high-reflectivity circular bragg grating mirror based on 220 nm silicon-on-insulator platform," *Opt. Express*, vol. 25, pp. 6653–6663, Mar 2017.